NASA TECHNICAL
MEMORANDUM

NASA TM X-58050
July 1970

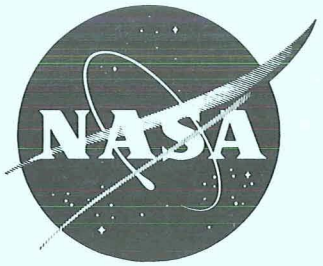

LINE BROADENING OF THE TRIPLET DIFFUSE SERIES OF HELIUM IN AN ARC-JET PLASMA

A Dissertation Presented to
the Faculty of the Graduate School of
The University of Texas at Austin
in Partial Fulfillment
of the Requirements for the Degree of
Doctor of Philosophy

NATIONAL AERONAUTICS AND SPACE ADMINISTRATION
MANNED SPACECRAFT CENTER
HOUSTON, TEXAS

NASA TM X-58050

LINE BROADENING OF THE TRIPLET DIFFUSE SERIES OF HELIUM IN AN ARC-JET PLASMA

Carl Douglas Scott
Manned Spacecraft Center
Houston, Texas

ACKNOWLEDGEMENTS

The author would like to express his gratitude to his supervising professors, Dr. Hans Schlüter and Dr. L. W. Frommhold. Dr. Schlüter's help in selecting the topic of investigation, his encouragement, and many discussions, and Dr. Frommhold's many discussions were invaluable. Thanks are tendered to Dr. Roger D. Bengtson, who made a number of helpful suggestions.

Special thanks are due Mr. David H. Greenshields and Mr. John E. Grimaud of the National Aeronautics and Space Administration, who made the work at the Manned Spacecraft Center possible.

The author gratefully acknowledges the assistance of Mr. V. P. Mellen and other Brown & Root-Northrup personnel who assisted with the experiments and of Miss Joann Birchett, Mr. Neil Wolfe, and other Lockheed Electronics Co. staff who programed the Abel inversion computer program.

March 1969

LINE BROADENING OF THE TRIPLET DIFFUSE SERIES OF HELIUM IN AN ARC-JET PLASMA

Carl Douglas Scott, B. A.
The University of Texas at Austin, 1969

Supervising Professor: Dr. L. W. Frommhold

Abel-inverted spectral-line profiles of the helium lines in the 2^3P-n^3D series were measured in an arc-jet plasma flow that had an electron density of 1.4×10^{15} cm^{-3} and a temperature of 7800° K at the center line. The electron density and temperature radial distributions were found from Abel-inversions of absolute continuum intensities and relative line intensities, respectively. The measured profiles were compared with theoretical profiles which were calculated from the quasistatic Stark broadening theory (similar to the theoretical calculations of Pfennig and Trefftz). In these calculations, Doppler broadening, although negligible, was included as a device to avoid singularities. An empirical correction to the theory was made which permits the validity of the quasistatic calculation for electrons to be extended into the impact regime toward the line cores and which improves the agreement with the measured profiles.

CONTENTS

SYMBOLS

A_{eff}	effective area of orifice
a	empirical constant
a_k	expansion coefficient of symmetrical part of intensity
$a_{I\mu}$	eigenvector
a_o	Bohr radius
b	empirical constant
b_k	expansion coefficient of antisymmetric part of intensity
b_n	temperature curve-fit coefficients
C_p	specific heat of water
c	velocity of light in vacuum
$D(\Delta\nu)$	Doppler function
d	mean distance of perturbers
E	electric-field strength
$\overline{E}$	field strength averaged over Stark components
E_H	ionization energy of hydrogen
$E_{M\mu}(\Delta\nu)$	field strength corresponding to a displacement $\Delta\nu$
$E_{n\ell}$	excitation energy of the n,ℓ level
E_o	normal-field strength
E_u	energy of upper energy state referenced to ground state
E_λ	energy of photon of wavelength λ
E_∞	ionization energy of helium

$\mathscr{E}_\mu$	eigenvalue = $\Delta\nu$
e	charge on the electron
f	absorption oscillator strength
g	statistical weight of lower energy level
$g_f(\lambda,T)$	free-free averaged Gaunt factor
$g_{n\ell}$	relative photoionization cross section for the n,ℓ level in units of the Kramers-Unsöld cross section
$g_n(\lambda)$	bound-free average Gaunt factor
$H_{L-1,L}$	first-order perturbation Stark-effect energy-matrix element
H_{LL}	unperturbed helium energy-matrix element
$H(\beta,y)$	electric-field probability distribution
h	Planck's constant, 6.62377×10^{-27} erg-sec
$\overline{h}$	mass averaged enthalpy determined from heat balance
h_s	stagnation enthalpy
I	arc current, amps
I	intensity, relative units
I_c	intensity of a continuum source
I_{cal}	intensity of calibration source at wavelength, λ
I_{line}	total integrated line intensity
$I_{M\mu}(\Delta\nu)$	intensity of the M,μ Stark component at $\Delta\nu$
I_T	Planck intensity function
$I(\Delta\nu)$	intensity, relative
I_λ	intensity at wavelength λ

J	total angular momentum
$J^{+}(y)$	symmetric part of measured intensity at position y
$J^{-}(y)$	antisymmetric part of measured intensity at position y
$J(\lambda)$	line intensity profile = $I_{line}L(\lambda)$
K	upper limit on sum in expansion
k	Boltzmann constant, 1.38026×10^{-16} erg/°K = 8.6159×10^{-5} eV/°K
k'	absorption coefficient
L	orbital quantum number
$L_{M\mu}(E)$	relative line intensity of Stark component
$L(\lambda)$	line profile normalized to total area equal to unity
M	magnetic quantum number
M_{He}	mass of helium atom
m	magnetic quantum number
$\dot{m}$	gas mass-flow rate through orifice
m_e	mass of the electron, 9.10721×10^{-28} grams
$\dot{m}_g$	gas mass-flow rate through the arc heater
$\dot{m}_w$	water mass-flow rate through the arc heater
N	effective perturber density
N_1	ion ground-state population
N_e	electron density, cm^{-3}
$N_e(r)$	electron density distribution

N_i	ion density, cm^{-3}
N_o	Total density in particles per unit volume
$N(r)$	radial intensity distribution in jet
$N(r,\lambda)$	power radiated per unit volume per steradian per unit wavelength at position r and wavelength λ
n	principle quantum number
P	pressure upstream of sonic orifice
P_o	standard atmospheric pressure
P_t	stagnation pressure in arc heater, atm
$P(\Delta\nu)$	general convolution of two broadening functions
$P(\lambda)$	instrument profile function
P^o_λ	peak value of normalized profile
R	gas constant
R	jet radius
r	radial position in jet
r_o	radius of the electron
$S(\lambda)$	source line profile
S_λ	sensitivity of the spectrometer
T	electron temperature, ^oK
$T(r)$	temperature as a function of jet position
$T(\Delta\nu)$	general broadening function (equals Doppler function in eq. (18))
t	effective thickness of plasma along a diameter
V	arc voltage
V_c	signal resulting from a continuum source

V_{cal}	photomultiplier signal resulting from a calibration source
V_{line}	total signal integrated over a line profile
V_{λ}	photomultiplier signal resulting from any source at wavelength λ
v	mean electron velocity
$v(\lambda)$	photomultiplier signal resulting from any source at wavelength λ
W(E)	electric field-strength distribution function
W	effective exit-slit width
$w_{1/2}$	half width, cm^{-1}
y	Debye shielding parameter = d/λ_D
y	position of jet measured vertically perpendicular to line of sight
y'	corrected scan position = $y_i - y_o$
y_i	position of i^{th} intensity measurement in Abel scan
y_o	position of center of jet
z	$\left(a \frac{\Delta\nu}{\Delta\nu_L}\right)^b$
z_1, z_2	coordinates of helium electrons
α	fine structure constant
β	E/E_o relative field strength
γ	ratio of specific heats
ΔE	advance of the series limit
ΔE	energy-level difference
ΔE_{∞}	reduction of the ionization energy
ΔT	temperature rise of arc heater cooling water

$\Delta\nu$	wave number referenced to center of line
$\Delta\nu_f$	finite integration limit in line-profile normalization
$\Delta\nu_J$	splitting of 2^3P level with J
$\Delta\nu_L$	minimum wave number for which the quasistatic theory is valid
$\Delta\nu_{M\mu}(E)$	displacement of Stark component M,μ because of field E
ε	a small number
$\varepsilon_M(\lambda,r)$	measured continuum emission coefficient
ε_o	permitivity of free space
$\varepsilon(\lambda)$	continuum emission coefficient
$\varepsilon(\lambda,N_e,T)$	continuum emission coefficient
$\varepsilon(\lambda,T)$	continuum emission coefficient
η_k	expansion function for intensity of jet
λ	wavelength
λ_D	Debye length
λ_k	a constant obtained when Abel-inverting $(R^2 - y^2)^k$
λ_o	wavelength at peak of line profile
μ	Stark-effect quantum number
ξ_k	expansion function for radial intensity distribution
π	3.14159
σ	measure of the width of a Gaussian function
σ	standard error
σ_λ	sensitivity of spectrometer

τ	optical depth
$\Psi(n,M,\mu)$	perturbed helium eigenfunction
$\Psi_o(n,L,M)$	unperturbed helium eigenfunction

Superscripts

+	symmetric part
-	antisymmetric part

1.0 INTRODUCTION

The study of the spectra of radiation emitted from plasmas has long been an invaluable tool in atomic research, not only for determining properties of the constituent atoms in the plasma, but also for determining properties of the plasma as a whole and for determining the effects of the plasma on the atoms. In this work, established spectroscopic techniques were used to determine the electron density and temperature in a helium arc-jet plasma. Then, these measured parameters were used to calculate the Stark broadening of spectral lines in the triplet-diffuse series of helium. These calculations were made by use of the quasistatic approximation for ions and electrons, and were compared with measured profiles in a plasma where the center-line electron density was $1.4 \times 10^{15} \pm 13$ percent cm^{-3} and the center-line temperature was 7800 ± 17 percent $^{\circ}K$. Not only is knowledge of the broadening useful from a laboratory viewpoint, but it is useful in determining conditions in stellar plasmas, and is important in solving radiative-transfer problems.

The theory of Stark broadening has been worked out for two limiting approximations: the quasistatic approximation, which applies to low-density and low-temperature plasmas; and the impact approximation, which applies to high-density and high-temperature plasmas.

The application of these approximations to helium line broadening has been restricted until now to comparisons with experimental measurements only in the extremes where one theory would be expected to predominate over the other. There has been increased astrophysical interest in the helium-triplet diffuse series because it is strong in many stellar spectra. This interest is also in conditions between the extremes, that is, in a range of electron

densities of 10^{14} to 10^{15} cm^{-3}. This is the range of conditions obtainable in arc-jet flows.

Measurements of the profiles of helium lines have been predominantly made in either the relatively low-density plasmas of radio-frequency (rf) discharges or the relatively high-density plasmas such as arcs and shock tubes.

Wulff (ref. 1) measured the profiles of various lines in the sharp, principal, and diffuse series of neutral helium in a pulsed arc discharge where the electron density was 3×10^{16} and the temperature was 30 000° K. Comparison of the 4471 Å and 4026 Å helium lines with a statistical theory of the Balmer H_β and H_γ lines, respectively, did not yield good agreement, as might be expected, because helium has a much more complex term structure than hydrogen does. Griem, et al. (ref. 2) calculated the helium line broadening in the impact approximation. They compared these calculations with those measured by Wulff (ref. 1) 4713 Å and 3965 Å lines, and found good agreement.

Vidal (ref. 3) made accurate measurements of the line broadening of the singlet and triplet diffuse series of helium in an rf discharge. In Vidal's experiments, the electron density was 2.65×10^{13} cm^{-3}, and the temperature was 1850° K. Pfennig and Trefftz (ref. 4) calculated the line wing profiles by using the quasistatic theory and then they compared these profiles with the measurements (ref. 3). Agreement in the far wings was reasonably good.

Greig, et al. (ref. 5) measured the profiles of the 3889 Å (2^3S-3^3P) and the 5016 Å (2^1S-3^1P) helium lines from a high-density plasma in a shock-tube source. The electron density determined from the width of the H_β line was in the range of 10^{16} to 10^{17} cm^{-3}. They found that the widths of the

helium lines just discussed compared well with the generalized impact theories of Griem, et al. (ref. 2) and Oertel (ref. 6).

In these experiments, measurements of line profiles in the helium-triplet diffuse series were made in the free-stream flow of an arc-jet plasma. The electron density was determined from absolute continuum-intensity measurements, and the electron temperature was determined from relative total line intensities. In the present work, an attempt is made to use the quasistatic theory to describe helium $2^3P\text{-}n^3D$ line profiles and to include an empirical correction to extend the range of validity of the theory toward the center of the line. This correction is patterned after those who applied it to hydrogen broadening, Schlüter (ref. 7) and Edmonds, et al. (ref. 8). This correction makes the perturber density N a function of the wave number $\Delta\nu$, tending from $N = N_e$ in the core to $N = 2N_e$ in the far wings.

Because of the inhomogeneous nature of the free-stream jet, the measured profiles were transformed to profiles which are functions of the jet radius by Abel-inversion. Comparisons of the experimental results and the theory are made at the center-line radius $r = 0$. The temperature and the electron density were determined as functions of the plasma radius by Abel-inversion of line and continuum intensities, respectively. The theoretical bases for these calculations are described in Section 2.1, Line Intensities and Temperature, and Section 2.2, Continuum Intensity and Electron Density.

The theoretical line-profile calculation in which the Doppler profile is folded with the quasistatic profile is described in Section 2.3, Quasistatic Stark Broadening Theory. This folding primarily is a mathematical convenience because the Doppler broadening is negligible compared with the Stark broadening at these conditions. The quasistatic profile is calculated from

the relative line strengths and frequency shifts of the Stark components of Pfennig and Trefftz (ref. 9). Baranger and Mozer's high-frequency component field-strength-distribution function, applicable for the electrons, was used. The ions are also accounted for by the same field-strength-distribution function. The empirical correction is also described.

The facility and instrumentation are described in Section 3.1, The Apparatus; the spectroscopic measurement techniques are described in Section 3.2, The Spectroscopic Measurements. These measurements include the Abel-inverted line and continuum intensities, Abel-inverted line profiles, and the instrument profiles.

The results of the measurements and the theoretical calculations are discussed in Section 4.0, Discussion of Results and Comparison of Experiment With Theory. It is shown that the agreement in the wings is reasonably good, except in regions where the forbidden components contribute to the profiles. The empirical correction is shown to improve agreement toward the line cores in cases where errors in the measured profiles are not too great.

The summary is given in Section 5.0, Summary. The relations involved for relative and absolute-line and continuum-intensity calibration are shown in appendix A. The cases for broad and narrow lines are discussed. The Abel-inversion calculations are discussed in appendix B.

2.0 THEORY

2.1 LINE INTENSITIES AND TEMPERATURE

Temperature is a quantity which defines the distribution of energy in a statistical system in equilibrium; hence, one can determine the temperature if the population of energy levels in an electronic system is known. Because the intensity of line radiation emitted from an optically thin gas is proportional to the population density of an energy state, one can obtain the temperature from intensity measurements.

The electron temperature in the arc-jet plasma was determined by the use of the standard method of the Boltzmann plot, wherein relative total-line intensities are used and log $(I\lambda^3/gf)$ is compared with E_u; I is the relative total intensity, λ is the wavelength of the line, g is the statistical weight of the lower energy level of the transition, and f is the absorption-oscillator strength. The slope of the resulting line equals $-(1/kT)$, where k is the Boltzmann constant and T is the electron temperature. This method is based on the assumption that the involved lines are optically thin. Also, the method is based on the expression for the intensity of a spectral line

$$I = \frac{2\pi hc^2 r_o}{\lambda^3} gfN_o e^{-E_u/kT} \qquad (1)$$

where h is Planck's constant, c is the velocity of light, r_o is the electron radius, and N_o is the total atom density. This equation is based

upon a local thermodynamic equilibrium, because a Boltzmann distribution of the energy levels is assumed.

The assumption of optical thinness is implicit here because the radiance $N(r)$ is determined from an Abel-inversion which holds for an optically thin plasma. The Abel-inversion numerical technique is discussed in appendix B.

2.2 CONTINUUM INTENSITY AND ELECTRON DENSITY

To determine the electron density, the equation for the continuum intensity was solved for the electron density. The equation used was that given by Anderson and Griem (ref. 11) for the emission coefficient for the continuum

$$\varepsilon(\lambda,T) = \frac{64\pi^2(\alpha a_o)^3}{3^{3/2}\lambda^2} cE_H\left[\frac{N_1}{N_i}\sum{}' \frac{g_{n\ell}(\lambda)}{n^3}\exp\left(\frac{E_\infty - E_{n\ell}}{kT}\right) + \sum{}'' \frac{g_n(\lambda)}{n^3}\exp\left(\frac{E_H}{n^2kT}\right) + \frac{g_f(\lambda,T)kT}{2E_H}\exp\left(\frac{\Delta E}{kT}\right)\right] \times N_e N_i \exp\left(-\frac{E_\lambda + \Delta E_\infty}{kT}\right)\left(\frac{E_H}{kT}\right)^{3/2} \tag{2}$$

where α is the fine structure constant, a_o is the Bohr radius, c is the speed of light, E_H is the ionization energy of hydrogen, k is the Boltzmann constant, T is the temperature, λ is the wavelength, n is the principle quantum number, $N_e = N_i$ is the electron density, and N_1/N_i is the ratio of ion ground-state population to total ion population (set equal to 1).

The relative photoionization absorption cross section for the n,ℓ levels is $g_{n\ell}$, in units of the Kramers-Unsöld cross sections, but is multiplied by the ratio of the statistical weight of the n,ℓ level to that of the hydrogen levels $2n^2$ and is divided by the statistical weight of the ion ground state. The variable $g_n(\lambda)$ is the bound-free Gaunt factor, and $g_f(\lambda,T)$

is the free-free Gaunt factor averaged over a Maxwellian velocity distribution of electrons. The values of these Gaunt factors were interpolated from the tables of Karzas and Latter (ref. 12). The E_∞ is the ionization energy; $E_{n\ell}$ is the excitation energy of the level.

The variable ΔE is the advance of the series limit given by Griem (ref. 13) in the formula

$$\Delta E = 4\left(a_o^3 N_e\right)^{4/15} E_H \tag{3}$$

The variable ΔE_∞ is the reduction in ionization energy given by Griem (ref. 13) in the formula

$$\Delta E_\infty = \frac{e^2}{4\pi\epsilon_o}\left(\frac{2e^2 N_e}{\epsilon_o kT}\right)^{1/2} \tag{4}$$

where E_λ is the photon energy and ϵ_o is the permittivity of free space.

In the sums, only those terms contribute for which the photon energy is greater than the energy required to excite a bound electron into a free state, taking into account the advance of the series limit. The upper limit on n for the bound-free sum is one less than the n corresponding to the last discernible line in the series. The electron density is then computed from the absclute continuum-intensity measurement

$$N_e(r) = \left[\frac{N(r,\lambda)}{\epsilon(\lambda)}\right]^{1/2} \tag{5}$$

where $N(r,\lambda)$ is the power radiated per unit volume per steradian per unit wavelength at a point in the plasma at a distance r from the center line.

2.3 QUASISTATIC STARK BROADENING THEORY

The theory of Stark broadening of spectral lines may be approached from two opposing idealizations: the impact theory and the quasistatic theory.

The impact theory is applicable when the phase of an emitted wave is on the average, only slightly changed during the time of the order of a few collision times. This condition applies in two general cases. In the first case, the collisions are strong enough to disrupt the phase of the wave, are well separated in time from one another, and occur instantaneously. Here, the collision time is effectively zero, while the average correlation time is the mean time between collisions. In the second case, the impact approximation holds if the collisions are so weak (although they may last for a significant time with their effects even overlapping) that their combined effect on the wave is small in the characteristic collision time.

The quasistatic approximation is based on the assumption that the excited atoms are in a relatively constant perturbing field produced by randomly situated (slowly moving) perturbers. The resulting electric microfield perturbs the energy levels; this disturbs the emitted line frequency by an amount $\Delta\nu$, which depends on the strength of the interaction. Thus, the total line shape depends on knowledge of the probability distribution for stationary perturbers to provide a given interaction with the atom. The slowly moving ions are particularly suited to this treatment; whereas, the faster moving electrons may be treated more adequately by the impact approximation, especially in high-temperature plasmas. However, as indicated in Section 1.0, INTRODUCTION, it has been shown that, for the line wings, the quasistatic approximation has been used successfully to describe the broadening because of electrons and ions in low-density, low-temperature rf hydrogen and helium plasmas. This was true for

the hydrogen case where the empirical correction of Schlüter (ref. 7) was used. In the present work, the same type of correction was applied to the quasistatic broadening theory of helium.

Pfennig and Trefftz (ref. 4) solved for the helium first-order energy-perturbation matrix elements resulting from a static external electric field and their associated line strength as a function of the electric field. This was done in parabolic coordinates by using essentially the same approximation as Foster (ref. 14). They formed the field-dependent off-diagonal matrix elements

$$H_{L-1,L} = H_{L,L-1} = eE\left\langle n,L,M\middle|z_1 + z_2\middle|n,L-1,M\right\rangle \tag{6}$$

where e is the charge of the electron; z_1 and z_2 are coordinates of the electrons; and n,L,M are quantum numbers.

These matrix elements form block diagonal submatrices that are associated with each M. The elements on the principle diagonals are the unperturbed energy eigenvalues. For $L \geq 1$, the helium eigenstate $\Psi_o(n,L,M)$ may be adequately described by an unexcited $1s$ electron which does not contribute to $H_{L-1,L}$ and by an excited electron $n\ell m(\ell = L, m = M)$, the eigenfunction of which is approximated by the hydrogen type. Thus, according to Bethe and Salpeter (ref. 15)

$$H_{L-1,L} = eE\left\langle n,\ell,m\middle|z\middle|n,\ell-1,m\right\rangle = \frac{2}{3}eEa_o n\left[\frac{(n^2-\ell^2)(\ell^2-m^2)}{(2\ell+1)(2\ell-1)}\right]^{1/2} \tag{7}$$

where a_o is the Bohr radius.

Pfennig and Trefftz (ref. 9) used the values for the diagonal elements H_{LL} of Martin (ref. 16) and extrapolated them to extend the table. They

expressed the Stark-effect eigenfunctions as linear combinations of the unperturbed helium functions $\Psi_o(n,L,M)$.

$$\Psi(n,M,\mu) = \sum_{\bar{L}} a_{L\mu}(E)\Psi_o(n,L,M) \tag{8}$$

Then, they solved the eigenvalue problem

$$\sum H_{LL'}a_{L'\mu} = a_{L\mu}\mathcal{E}_{\mu} \tag{9}$$

with the normalization condition

$$\sum_{L=M}^{n-1} a_{L\mu}^2 = 1 \tag{10}$$

($\mu = M, M + 1, \ldots n - 1$). The index μ is related to the parabolic quantum number n_1, that is, $\mu = n_1 + M$. Pfennig and Trefftz (ref. 9) tabulated the Stark effect, splitting $\Delta\nu$ (perturbation energy) and relative line intensities $L_{M\mu}$. The splitting is relative to the unperturbed nD level, and perturbations in the 2P levels are neglected.

The equation for the perturbed relative line intensity of one component is given by the equation

$$I_{M\mu}(\Delta\nu) = \int_{-\infty}^{\infty} \delta\left[\Delta\nu_{M\mu}(E) - \Delta\nu\right] L_{M\mu}(E)W(E)\,dE \tag{11}$$

where $L_{M\mu}(E)$ is the relative line intensity as a function of perturbing field strength and $W(E)\,dE$ is the probability of finding the atom in a perturbing field $E \leq E' \leq E + dE$. The integration with the Dirac delta function picks out a particular field strength associated with a given wave number.

Integration in equation (11) by the use of the theory of generalized functions yields

$$I_{M\mu}(\Delta\nu) = L_{M\mu}\left(E_{M\mu}\right)W\left(E_{M\mu}\right)\left|\frac{dE}{d\Delta\nu}\right|_{M\mu} \tag{12}$$

where $E_{M\mu}$ is the electric field that is required to produce a displacement $\Delta\nu$ in the M,μ component. A summation of the overall components yields

$$I(\Delta\nu) = \sum_{M,\mu} L_{M\mu}\left(E_{M\mu}\right)W\left(E_{M\mu}\right)\left|\frac{dE}{d\Delta\nu}\right|_{M\mu} \tag{13}$$

This is the expression used by Pfennig and Trefftz (ref. 4) in their calculation. However, this equation is not valid for certain values of $\Delta\nu$. In several of the components, $\left|\frac{dE}{d\Delta\nu}\right|_{M\mu}$ is singular for certain $\Delta\nu$. This is because of a reversal or stoppage in the displacement $\Delta\nu$ with increasing field strength. To avoid this mathematical difficulty, equation (11) was folded with the Doppler broadening function.

$$D(\Delta\nu) = \frac{M_{He}c^2}{2\pi kT}\, e^{-\frac{M_{He}c^2\Delta\nu^2}{2kT}} = \frac{2}{\sqrt{\pi}}\,\frac{1}{\sigma}\, e^{-(\Delta\nu/\sigma)^2} \tag{14}$$

One interesting feature of this function is that, in the limit $\sigma \to 0$, the Doppler function behaves like the delta function. However, in the physical situation, the Doppler function has a finite width; thus, the singularity encountered by using a delta function is eliminated.

The general expression for the folding of two broadening functions is

$$P(\Delta\nu) = \int_{-\infty}^{\infty} I(\Delta\nu')T(\Delta\nu - \Delta\nu')\, d(\Delta\nu') \tag{15}$$

Equations (11) and (14) are substituted into equation (15) to yield

$$P(\Delta\nu) = \int_{-\infty}^{\infty}\int_{-\infty}^{\infty} \delta\left[\Delta\nu_{M\mu}(E) - \Delta\nu'\right] L_{M\mu}(E)W(E)D(\Delta\nu - \Delta\nu')\, d\Delta\nu'\, dE \qquad (16)$$

The integration of equation (16) with respect to $\Delta\nu'$ yields

$$I(\Delta\nu) = \int_{-\infty}^{\infty} W(E)L_{M\mu}(E)D\left[\Delta\nu - \Delta\nu_{M\mu}(E)\right] dE \qquad (17)$$

where $P \rightarrow I$ in the notation. Thus, the Doppler function has replaced the delta function in the integral. This integral may now be computed by numerical means. The desired equation for the triplet lines is obtained by restoring all components of the line and by considering the splitting in the 2^3P level.

$$I(\Delta\nu) = \sum_{J=0}^{2} \frac{2J + 1}{9} \sum_{M,\mu} \int_{0}^{\infty} W(E)L_{M\mu}(E)D\left[\Delta\nu - \Delta\nu_{M\mu J}(E)\right] dE \qquad (18)$$

where $\Delta\nu_{M\mu J}(E) = \Delta\nu_{M\mu}(E) + \Delta\nu_J$, $\Delta\nu_J = 1.045$ for $J = 0$, $\Delta\nu_J = 0.049$ for $J = 1$, and $\Delta\nu_J = 0.029$ for $J = 2$. Because the integrand is defined as zero for $E < 0$, the lower limit of the integration may be zero.

If $W(E)$ and $D(\Delta\nu)$ are normalized and if $\sum L_{M\mu}(E) = 1$, then

$$\int_{-\infty}^{\infty} I(\Delta\nu) = 1 \qquad (19)$$

In the tables of Pfennig and Trefftz (ref. 9), $\sum L_{M\mu}(E) = 1$ when the sharp component of the line ($\mu = 0$ term) is omitted.

The field-strength distribution function $W(E)$ was obtained from the $H(\beta,y)$ tables of Baranger and Mozer (ref. 10) for the high-frequency component.

In these tables, a two-body correlation approximation was used to account for shielding when β is the dimensionless field strength E/E_o. Recently, Hooper (ref. 17) has calculated the field-strength distribution function. His calculations account for all the higher order correlations; however, for small Debye shielding parameters y, the tables of Baranger and Mozer (ref. 10) differ very slightly from those of Hooper (ref. 17). They tabulated $H(\beta,y)$ for β from 0.2 to 10 and for y from 0 to 0.8 where $y = d/\lambda_D$. The following equation defines d.

$$\frac{4}{15}(2\pi)^{3/2}d^3N = 1 \tag{20}$$

where N is the perturber density and $\lambda_D = \left(kT/4\pi N_e e^2\right)^{1/2}$ is the Debye length. The normal field strength E_o is defined by

$$E_o = \frac{e}{d^2} \tag{21}$$

Equations (20) and (21) are combined to yield

$$E_o = 3.748 \times 10^{-10} N_e^{2/3} \text{KV/cm} \tag{22}$$

The function W(E) was obtained from the tables of $H(\beta,y)$ by the relation

$$W(E) = \frac{1}{E_o} H(\beta,y) \tag{23}$$

For $\beta > 10$, the asymptotic formula of Baranger and Mozer (ref. 10) was used.

$$H(\beta) \approx H_o - y\beta^{-7/2}\left(0.5453y + 11.78\beta^{-1} + 114.6\beta^{-5/2} + \cdots\right) \tag{24}$$

where $H_o \approx 1.496\beta^{-5/2} + 7.639\beta^{-4} + 21.60\beta^{-11/2} + \cdots$.

An empirical correction to the line profile may be made by following the reasoning of Griem (ref. 18), Schlüter (ref. 7), and Edmonds, et al. (ref. 8). Here, an attempt was made to extend the basic quasistatic Stark broadening theory toward the center of the lines by making the effective perturber density a function of the wavelength. Effectively, this makes the line core a function only of ions, whereas the wings become dependent on both electrons and ions in a smooth transition. The empirical correction used is of the form

$$N = N_e\left[1.5 + 0.5\left(\frac{z - 1}{z + 1}\right)\right] \tag{25}$$

and

$$z = \left(a\,\frac{\Delta\nu}{\Delta\nu_L}\right)^b \tag{26}$$

where a and b are constants to be chosen, $\Delta\nu < \Delta\nu_L$ is the displacement from the line center for which impact treatment of the electrons is appropriate, and $\Delta\nu > \Delta\nu_L$ is the range of validity of the quasistatic approximation.

The value of $\Delta\nu_L$ was calculated by the use of the asymptotic behavior of $W(E)$ and by averaging over Stark components. For the quasistatic approximation to be valid, the time between collisions $\tau = r/v$ must be long compared with the perturbation period $1/2\pi|\Delta\nu|c$. Here, v is the velocity and r is

the distance of the perturbing particle which produces the electric field. Thus,

$$\tau >> 1/2\pi|\Delta\nu|c \tag{27}$$

Because $E = e/r^2$ and $\frac{1}{2} m_e v^2 = \frac{3}{2} kT$, the following condition exists.

$$\Delta\nu >> \Delta\nu_L \equiv \frac{1}{4\pi^2 c^2 e} \frac{3kT}{m_e} \frac{E}{\Delta\nu} \tag{28}$$

This condition is too strict, as a precise calculation of the theory shows. It is sufficient to have the following condition (ref. 19).

$$\Delta\nu_L = 0.2 \frac{1}{4\pi^2 c^2 e} \frac{3kT}{m_e} \frac{E}{\Delta\nu} \tag{29}$$

Values were calculated for $E/\Delta\nu$ and were averaged over all of the Stark components in the following manner.

$$\overline{E} = \sum E_{M\mu} \left[\frac{L_{M\mu}(E) W\left(E_{M\mu}\right) \left|\frac{dE}{d\Delta\nu}\right|_{M\mu}}{\sum L_{M\mu}(E) W\left(E_{M\mu}\right) \left|\frac{dE}{d\Delta\nu}\right|_{M\mu}} \right] \tag{30}$$

where the factor in the parentheses is a weight factor which weighs the components by the fractional intensity of the component. With the approximation that $\left|\frac{dE}{d\Delta\nu}\right|_{M\mu} \approx \frac{E_{M\mu}}{|\Delta\nu|}$ (justified in the linear Stark effect and therefore only slightly dependent on $\Delta\nu$), the asymptotic expression $W(E) \sim E^{-5/2}$ may be

used to obtain the approximate expression for the average field strength, as shown in equation (31).

$$\bar{E} \approx \frac{\sum L_{M\mu}(E) E_{M\mu}^{-1/2}}{\sum L_{M\mu}(E) E_{M\mu}^{-3/2}} \tag{31}$$

Because $\bar{E}$ is only slightly dependent on the value of $\Delta\nu$, $\bar{E}/\Delta\nu$ may be introduced into the expression for $\Delta\nu_L$. In the numerical calculation, a component was omitted if it did not contribute to the line profile in the range of interest; for example, the S ($\mu = 0$) component was omitted.

The technique for extending the range, for which the quasistatic theory applies, is limited because the profiles are no longer automatically normalized if $W(E)$ has been normalized by the use of a constant normal field strength E_o. To avoid renormalization of the line profile, $W(E)$ was normalized in the following manner. Taking the normalization condition

$$\int_0^\infty H(\beta) d\beta = 1 \tag{32}$$

and transforming the variable of integration the following is obtained

$$\int_0^\infty H\left(\frac{E}{E_o}\right) \left|\frac{\partial\beta}{\partial E}\right| \, dE = 1 \tag{33}$$

where $\left|\frac{\partial\beta}{\partial E}\right|$ is the absolute value of the Jacobian of the transformation.

$$\left|\frac{\partial\beta}{\partial E}\right| = \left|\frac{1}{E_o} - \frac{E}{E_o^2} \frac{\partial E_o}{\partial N} \frac{\partial N}{\partial z} \frac{\partial z}{\partial \Delta\nu} \frac{\partial \Delta\nu}{\partial E}\right| \tag{34}$$

Therefore,

$$\int_0^\infty \frac{1}{E_o} H\left(\frac{E}{E_o}\right)\left|1 - \frac{E}{E_o}\frac{\partial E_o}{\partial N}\frac{\partial N}{\partial z}\frac{\partial z}{\partial \Delta\nu}\frac{\partial \Delta\nu}{\partial E}\right| = 1 \tag{35}$$

A modified field-strength distribution may be defined as

$$W(E) = \frac{1}{E_o} H\left(\frac{E}{E_o}\right)\left|1 - \frac{E}{E_o}\frac{\partial E}{\partial N}\frac{\partial N}{\partial z}\frac{\partial z}{\partial \Delta\nu}\frac{\partial \Delta\nu}{\partial E}\right| \tag{36}$$

This differs from the usual definition of $W(E)$ by the Jacobian factor. Here the normalization is preserved.

In calculating the derivatives in the Jacobian factor, equations (22), (25), and (26) were used. The dependence of $\Delta\nu$ on E was found in the tables of Pfennig and Trefftz (ref. 9) for each Stark component. The derivative was calculated numerically by fitting a parabola to three adjacent points about E and then by calculating the derivative of the parabola at E.

In calculating the theoretical line profiles, equation (18) was programed for computation on a digital computer. The tables of line intensities $L_{M\mu}$, displacements $\Delta\nu$ (eigenvalues), and field-strength values E were taken from Pfennig and Trefftz (ref. 9). The tables were interpolated for intermediate values of E in the integration. The field-strength distribution-function $H(\beta,y)$ tables of Baranger and Mozer (ref. 10) were interpolated with the calculated value of y for each β. The resulting distribution was then used in the calculation of $W(E)$ according to equation (36), interpolating for intermediate values of E.

3.0 EXPERIMENT

3.1 THE APPARATUS

3.1.1 The Arc-Jet Facility

Measurements of the spectral line, continuum intensities, and the line profiles were made in the 1.5-megawatt arc-tunnel facility at the Manned Spacecraft Center. An arc heater, shown in figure 1, is used to heat various gases to high temperatures. In these experiments helium was used.

The arc heater was designed and built by Electro-Optical Systems, Inc., under a NASA contract. The arc heater consists of a tungsten-tipped cathode at the upstream end, a restrictor tube with an inside diameter of 2 cm, a divergent conical nozzle, and a ring of anode pins in the nozzle. All components are water cooled. The restrictor section consists of a number of annular-ring, water-cooled segments made of copper. They are insulated from one another with boron nitride inserts. Also, the segments are separated by O-ring seals. The conical nozzle is segmented in the same manner as the restrictor section. One of the segments in the nozzle consists of a boron nitride annular ring and it has 30 radially drilled holes which accommodate the copper anode pins. Thus, each of the 30 radial pins forms part of the anode. Each pin is connected in series with a 1.4-ohm ballast resistor, which insures that the current is divided evenly among the 30 pins.

Gas is injected approximately tangentially near the cathode through an entry block made of boron nitride. There is a secondary-gas inlet approximately 12 inches downstream from the cathode. This inlet can be used to introduce a secondary gas such as oxygen. However, in this experiment, this inlet was used to inject helium. A small amount of an inert gas is also

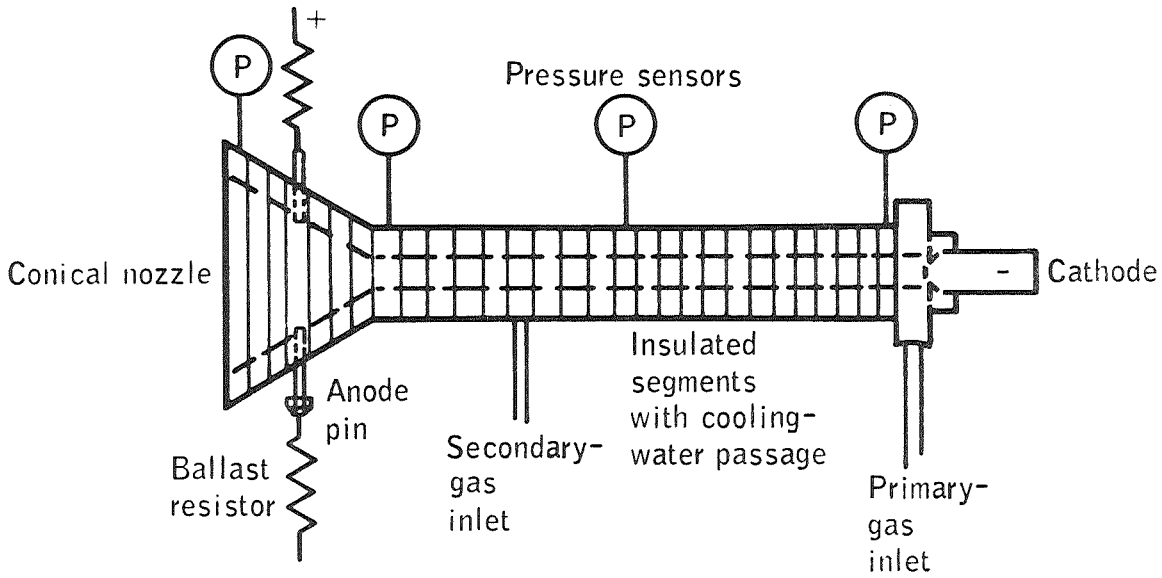

Figure 1.- Schematic diagram of arc heater.

introduced around the anode pins. This gas cools the pins and the boron nitride ring which insulates them from the copper segment.

The power applied to this arc heater is limited to 1500 A and 1 MW. The current limitation is because of the cathode. The tungsten tip begins to spallate at higher currents. The 1-MW limitation is because of the heat load to the restrictor section, which was designed to absorb up to 320 KW of combined radiative and convective heating. Early in the experiments, it was found that 1400 A was the maximum current that could be used reliably because of the failure of anode ballast-resistor elements at the points of contact with the water-cooling-tube fittings. Later, a modification in the design of these fittings eliminated this problem. Because data had been taken at the 1400-A condition, it was decided not to increase the current, although running at as high a power as possible was desirable because the plasma luminosity increased with an increase in power.

The arc heater was designed to run on gas-flow rates of from 2 to 20 g/sec. A lower flow limit is necessitated by the increase in heating to the restrictor section at very low gas-flow rates. It was found that the maximum gas enthalpy (calculated by the heat-balance method) could be obtained at gas-flow rates of from 2 to 3 g/sec. A total gas-flow rate (not including anode-pin bleed) of 2.0 g/sec was chosen. While running on pure helium, a flow of 1.5 g/sec was introduced at the cathode, and 0.5 g/sec was introduced in the restrictor section (secondary inlet). An anode-pin bleed of approximately 0.5 g/sec of helium was used to externally cool the boron nitride ring.

Four pressure taps are located on the arc heater to measure pressure. One tap is located near the cathode, a second tap is approximately in the

center segment of the restrictor, a third tap is in the "throat" or downstream-end segment of the restrictor, and the fourth tap is at the nozzle exit.

The initial arc discharge is begun at a low pressure (approximately 0.5 torr) and a starting gas-flow rate of approximately 0.5 g/sec. Argon and helium have breakdown potentials that are low enough that an open-circuit voltage of 1000 volts will initiate the discharge. Once the discharge is established, the main gas flow is turned on and the starting flow is then turned off.

The heated gas is expanded to supersonic velocities through the conical nozzle into a vacuum test chamber. The nozzle has a full-divergence angle of approximately 56°. The exit diameter is 6 inches.

The vacuum test chamber and the arc heater are shown in figure 2. The chamber is approximately 6 feet in diameter and contains apparatus for inserting ablation models and probes into the jet. Mirrors are mounted inside to direct light from the jet or ablation models out through windows into light-measuring instruments. The chamber is connected to the diffuser section and heat exchangers, and then is connected to a four-stage steam-ejector system which maintains a vacuum in the system. A large valve, located in the vacuum line between the steam ejectors and heat exchanger, is used to control the pressure inside the test chamber. The valve is electrically operated from the control room so that the chamber can be isolated from the steam ejectors by closing the valve, and so that the pressure inside the chamber can be regulated by adjusting the extent to which the valve is opened. In these experiments, a pressure of 4.76 torr was maintained in the test chamber and was measured by a radioisotope-type ionization gage (Alphatron).

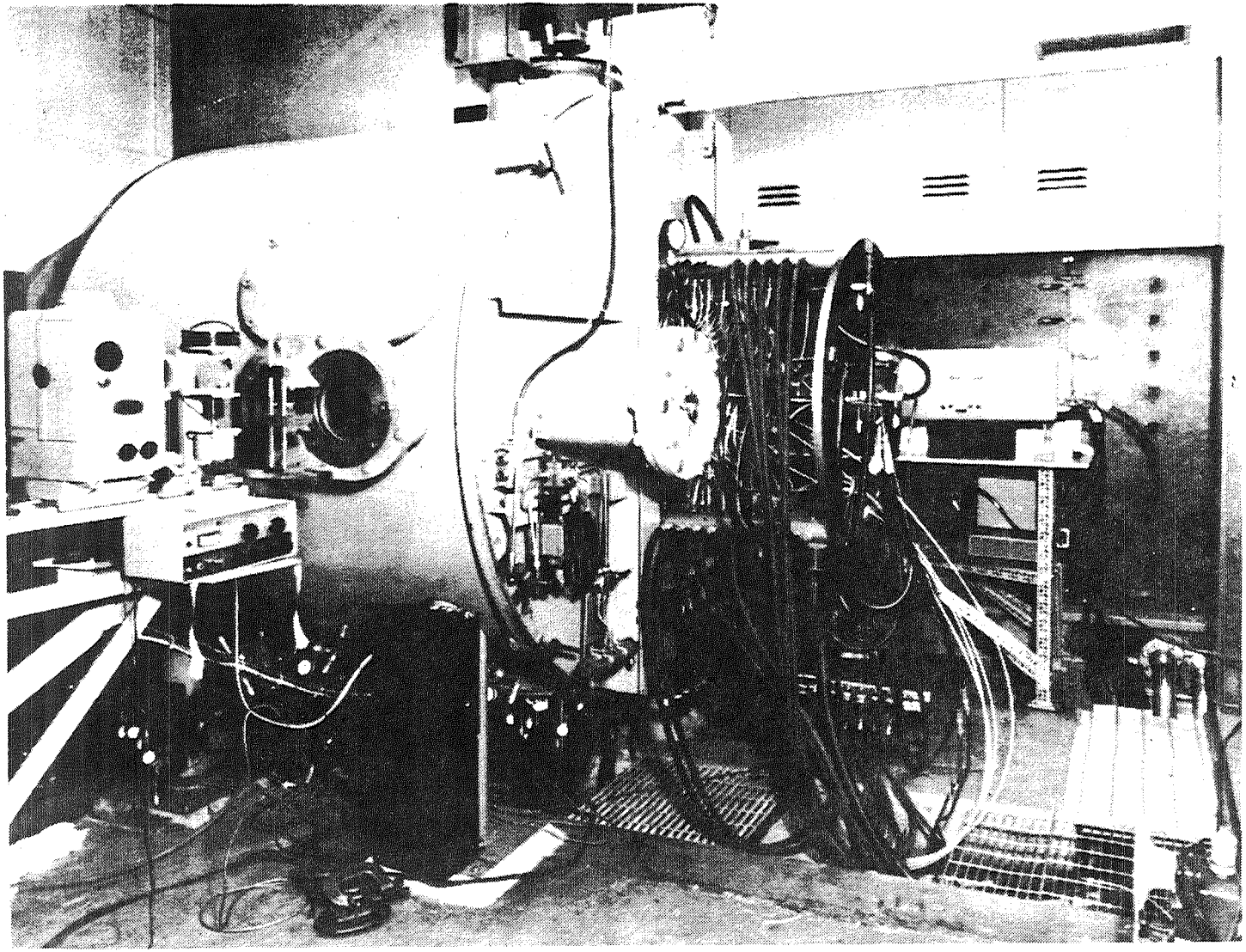

Figure 2.- Vacuum chamber with arc heater mounted on the door; viewing window is on the left side of the chamber.

Power to the arc heater was supplied by a 1.5-MW ac and dc power supply operated in the dc mode. This power supply will operate in three basic dc configurations (table I). Four pairs of modules in parallel can be linked to provide the current and voltage combinations shown in table I.

The current is controlled by saturable-core reactors on the ac side of the power supply. Rectification is accomplished by the use of three-phase silicon diode bridge networks.

The arc heater, test chamber, and heat exchanger are cooled by 500-psi deionized water flowing in a closed system. This water is then cooled through a water-to-water heat exchanger which is supplied by a secondary open-loop water system. A small amount of water is continually recirculated through deionizers. Deionization of the water is necessary to prevent buildup of mineral deposits in the arc heater and other water passages and to minimize the water conductivity.

3.1.2 The Facility Instrumentation and Measurement Techniques

The facility instrumentation consists of various types of transducers for measuring pressures, temperatures, flow rates, voltages, and so forth. The electrical output signals from these instruments are recorded on a 50-channel analog-to-digital magnetic tape recorder. The magnetic tapes of data are then processed on a digital computer in the MSC computation center. A sample of the computer output is shown in table II. The time-averaged values and minimum and maximum values of each measured quantity are given. The variations indicated by the minima and maxima are caused by noise and drift (for nominally constant quantities).

TABLE I.- 1.5 MW ac AND dc POWER SUPPLY CHARACTERISTICS IN THE dc MODE

	Parallel configuration	Series-parallel configuration	Series configuration	Single pair of modules
Open-circuit voltage, V . . .	1000 V	2000 V	4000 V	1000 V
Maximum current, A	3000 A	1500 A	750 A	750 A

TABLE II.- SAMPLE DATA FROM DATA REDUCTION COMPUTER PROGRAM

National Aeronautics and Space Administration
Manned Spacecraft Center - Houston
Experimental Heat Transfer Section

Statistical Report Number of Samples 1915
Test Run 423 Run 4230007 Tape 52676

Time	Seconds	Date
Starting	2.6062	12-19-68
Ending	64.3764	12-19-68

Measurement Description	Average	Units	Range	
Event	3.78110		-89.3786	94.9964
Main H_2O Temp In	67.2433	Deg.F	53.7282	82.9703
Arc Heater H_2O Temp Out	84.2175	Deg.F	78.3345	92.9680
Delta T	16.5217	Deg.F	16.3581	16.7089
Arc Heater H_2O Flow	18.3722	lb/sec	18.2266	18.4924
Mid-Con Helium Flow	.120825-02	lb/sec	.120611-02	.121045-02
Cathode Helium Flow	.303156-02	lb/sec	.302850-02	.303516-02
Voltage	475.953	Volts	474.277	478.083
Current	1409.71	Amps	1403.55	1419.88
Nozzle Pressure	4.59730	Torr	3.93940	5.35605
Throat Pressure	286.135	Torr	284.976	287.074
Mid-Construction Pressure	502.873	Torr	500.931	504.665
Cathode Pressure	581.800	Torr	578.129	585.840
Chamber Alphatron	4.82645	Torr	4.78047	4.89595
Nozzle Alphatron	3.95931	Torr	3.91816	4.00741
Intensity	-7.41421	MV	-44.3476	.607147-01
Abel Scan Position	5.34408	MV	-34.2110	36.7661
Abel Scan Command	57.7177	MV	-.833321-02	94.2833

The measurements of the spectral lines were made at one set of run conditions; therefore, the values shown are considered standard and typical.

The instruments used to measure facility parameters are described as follows. Copper-constantan thermocouples are used to measure water temperatures. The temperature increase in the water which flows through the arc heater is measured by a thermopile, the output of which is a millivolt signal that is approximately proportional to the temperature difference between the water inlet and the water outlet.

Water-flow rates are measured by turbine-type flowmeters, the output of which is a frequency that is proportional to the flow rate. This sinusoided signal is converted to a dc signal by a frequency-to-analog converter. Gas-flow rates of the primary gases are measured by the sonic-orifice technique. The pressure upstream of a calibrated orifice is measured with a strain-gage-type pressure transducer. The flow rate is then calculated by the use of the sonic-orifice equation

$$\dot{m} = A_{eff} P \left[\frac{32.2\gamma}{RT} \left(\frac{2}{\gamma + 1} \right)^{\frac{\gamma+1}{\gamma-1}} \right]^{1/2} \tag{37}$$

where $\dot{m}$ is the mass-flow rate, A_{eff} is the effective orifice area, P is the upstream pressure, R is the perfect gas constant, T is the temperature, and γ is the ratio of specific heats of the gas. For this formula to be valid, the upstream pressure must exceed the downstream pressure at least by about a factor of two.

The current through the arc heater was determined by measuring the potential drop across a calibrated resistor which was in series with the arc heater. This voltage was transduced by an isolating device, the dc output of

which is proportional to the dc input. The potential drop across the arc heater was measured by a similar transducer. Isolation of the recorder from the arc heater power supply was necessary for safety reasons and to protect the recorder from possible large-current ground loops.

The nozzle-exit pressure and the test-chamber pressure were measured by an Alphatron ionization gage. The other pressures in the system were measured by strain-gage-type pressure transducers.

A measure of the net energy introduced into the gas by the arc heater is the heat-balance enthalpy. It is defined by the equation

$$\bar{h} = \frac{IV - C_p \dot{m}_w \Delta T}{\dot{m}_g} \tag{38}$$

where I is the current across the arc heater, V is the voltage across the arc heater, C_p is the specific heat of water, ΔT is the temperature increase of the cooling water through the arc heater, $\dot{m}_g$ is gas-flow rate, and $\dot{m}_w$ is the cooling-water flow rate through the arc heater. Strictly speaking, this is not the actual thermodynamic enthalpy, because it is a quantity averaged over the length of the arc heater and the pressure is not constant over the length of the arc heater. In these experiments $h = 1.81 \pm 0.05 \times 10^{12}$ erg/g. The standard error is given here along with the calculated values.

Another measure of the stagnation enthalpy is given by the sonic-throat equation (ref. 20).

$$h_s^{1/2} = \frac{P_o A^* P_t}{\dot{m}_g} \left(\frac{32.2}{778}\right)^{1/2} \left[\frac{\gamma^2}{\gamma - 1} \left(\frac{2}{\gamma + 1}\right)^{\frac{\gamma+1}{\gamma-1}}\right]^{1/2} \tag{39}$$

This equation is based on the assumption that the gas behaves as a perfect gas. P_o is standard atmospheric pressure, 2115 lb/ft^2; A* is the area of the sonic-nozzle throat, ft^2; and P_t is the stagnation pressure, atmospheres. The two numbers in parentheses are conversion factors. In these experiments $h_s = 1.95 \pm 0.09 \times 10^{12}$ erg/g. This technique for determining the stagnation enthalpy is only an approximation because of the following factors. The gas is not strictly perfect, because there is some ionization, No true stagnation pressure exists, because there is a pressure gradient along the length of the restrictor. The pressure measured at the cathode was used in the sonic-throat equation; it is considered that this pressure is most representative of a stagnation pressure, because the gas velocity is lowest at that location.

3.1.3 The Spectroscopic Instrumentation

The spectroscopic data were obtained by the use of a Jarrel-Ash 3.4-m Ebert stigmatic spectrograph. This instrument has both photographic and photoelectric capability. A grating having 590 lines/mm and an effective aperture of 114 mm was used, yielding a total of 67 260 rulings. The spectrograph has a reciprocal dispersion of 5.05 Å/mm in the first order with this grating. Photographic plates were used to identify the spectra and for qualitative evaluation of the spectra.

A sine bar-grating drive rotates the grating so that the spectral line scans across the exit slit linearly in time or with shaft rotation when a constant-speed motor drives the sine-bar lead screw. Various combinations of entrance-slit and exit-slit widths were used during these experiments. The choice depended on the type of measurement and on the width of the spectral lines being measured. It was desirable to use as wide a slit as possible,

narrow enough to sufficiently resolve the line in question. It was fortuitous that the weaker lines were broader, so that wider slits could be used to increase signal strength.

Photoelectric measurements were made using an EMI-6255B photomultiplier tube that has an S-13 response. The anode was connected through a 1MΩ resistor to ground.

The resultant signal was connected to the input of the phase-sensitive lock-in amplifier. The light going to the spectrograph was interrupted at a rate of 10 800 Hz by a light chopper that was mounted next to the entrance slit. The light chopper had an output signal that was used as a reference by the amplifier. Positioning the chopper in front of the entrance slit was very critical, because openings in the blades were small. There were 180 openings near the periphery of the 9-inch-diameter chopper blade. Vibration induced into the spectrograph when the chopper was mounted directly to the optical bench was serious enough to cause fluctuations in the output signal when using narrow slits. To eliminate this problem, the chopper was mounted on a support which was isolated from the spectrograph. A schematic of the arc tunnel, spectrometer, and optical path is shown in figure 3.

The optical path passed from the arc jet F_c through two mirrors, M_1 and M_2. These two mirrors were needed so that a region 5-inches from the nozzle exit plane could be viewed perpendicularly to the axis of the jet. The window in the tunnel had a diameter of 7 inches, and its center was 9 inches from the nozzle exit plane. The window was made of fused silica.

After the light passed from the tunnel, the image was rotated 90° in a plane perpendicular to the optical axis by a pair of mirrors. At the same time, the optical axis was directed to the scanning mirror M_R. Rotation of

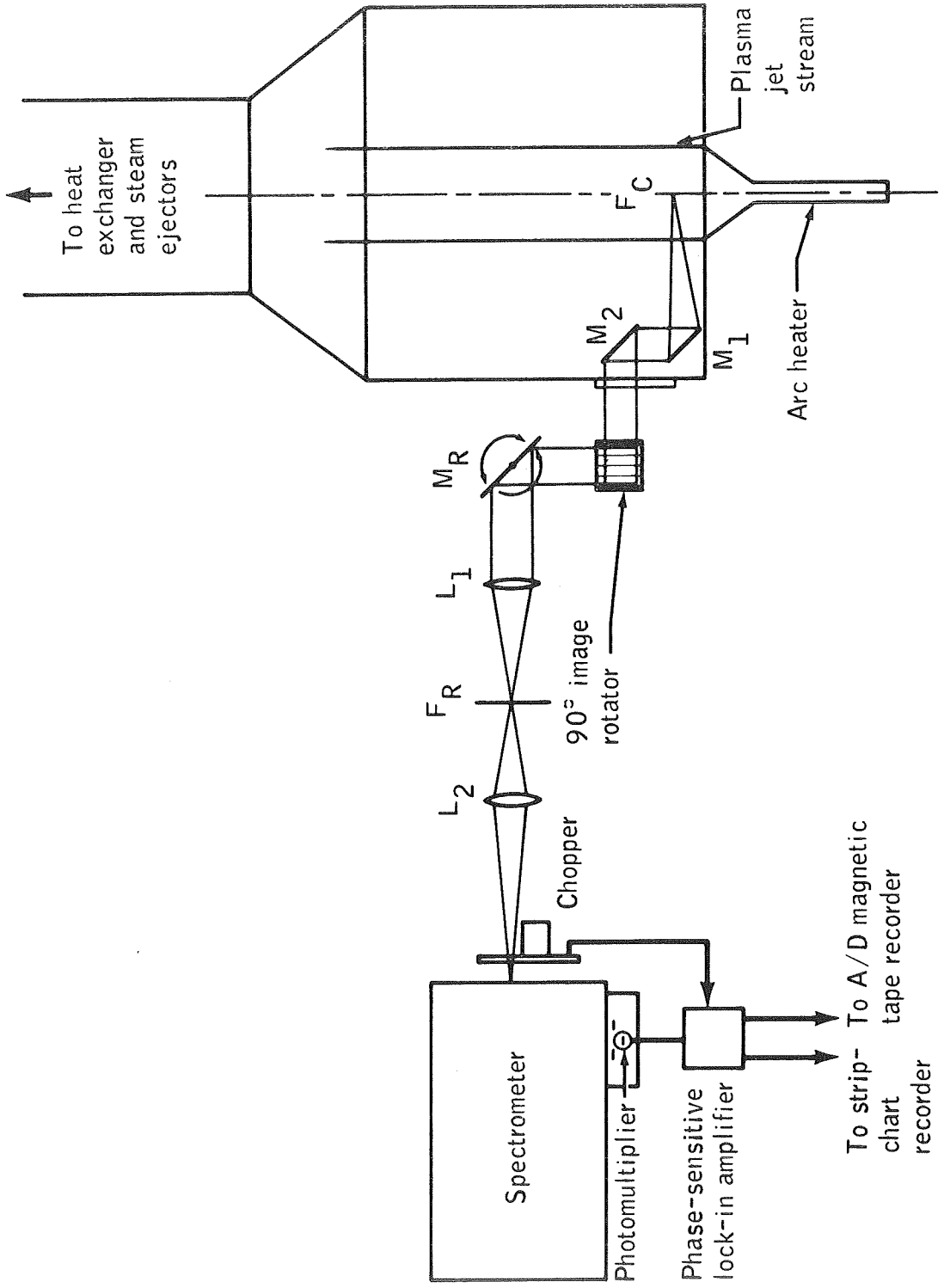

Figure 3.- Arc tunnel, showing the optical arrangement.

the image was necessary so that the image of the horizontal jet could be made to lie along the length of a vertical entrance slit.

The scanning mirror was driven by a stepping motor, and its angular rotation was sensed by a single-turn resistive-film potentiometer which had a linearity of ±0.01 percent. The angle of rotation of the mirror required to scan from one side of the jet to the other side (a distance of 14 cm) was 2.6°. Therefore, the accuracy in mirror position was reduced to ±1.4 percent of full deflection, neglecting any other sources of error.

From the scan mirror, the light was directed through a 70-mm-diameter collecting lens, L_1, then to a 30-mm-diameter focusing lens, L_2, then to the chopper and entrance slit of the spectrometer. All lenses were made of fused silica to provide transmission in the near ultraviolet. All mirrors were first-surface mirrors deposited with pure aluminum and were without overcoat. It was found that the mirrors inside the test chamber had to be replaced occasionally, because a film deposited on their surfaces. This film was probably a product of ablation which had condensed onto surfaces of the test chamber during previous runs during which ablation materials were tested. However, it should be pointed out that no evidence of ablation products appeared in the long-exposure spectrograms. The only identifiable impurities that were detected in the spectra were a weak OH band in the spectral range of 3063 to 3400 Å and a very weak N_2^+ bandhead near 3900 Å. This probably came from water vapor which had diffused into the test chamber from the steam ejectors and small air leaks.

Reference sources and calibration sources were placed at the focal plane F_R. Likewise, an iron arc was located there when the optics were being alined. A ribbon-filament lamp was also placed at the focal plane F_c, in the

chamber for use as a calibration source to determine the spectral transmission of the optical path. To determine the largest slit height usable while calibrating with the source at F_c, the photomultiplier output was measured compared with the slit height. The results were plotted, and the curve was linear up to a height of approximately 7 mm. Therefore, a 7-mm slit height was used when calibrating the optical path.

To verify that the transmission function of the optics would remain the same for any portion of the jet in a plane perpendicular to the axis of the jet, the lamp was centered approximately 10 cm above, 10 cm below and on the jet axis. The variation in the signal from one position to another was less than ± 1 percent. The radius of the luminous jet was 2.75 inches (6.99 cm) at the position 5 inches from the nozzle exit plane. This was determined by inserting a water-cooled probe into the jet at the lower visible boundary, then at the upper boundary, and taking the difference in probe position. The probe was positioned electromechanically by a servo system.

To obtain Abel-inverted line profiles, the scan mirror and the grating were positioned sequentially by a programable stepping-motor indexer. This device drove both the grating-scan stepping motor and the position-scan stepping motor. The motor shaft rotated 1.8° per step. The motors were connected to the grating drive and the scan mirror through reduction gears to obtain the very small rotations necessary for scanning. A magnetic clutch was used in the grating-drive linkage so that the grating could be rotated manually from one line to another without having to disconnect the motor. A drawing of the (Abel) position-scan-drive assembly is shown in figure 4.

The position- (or Abel) scan motor was stepped a preset number, N steps, M times. After each N steps, the motor stopped for a preset time, t.

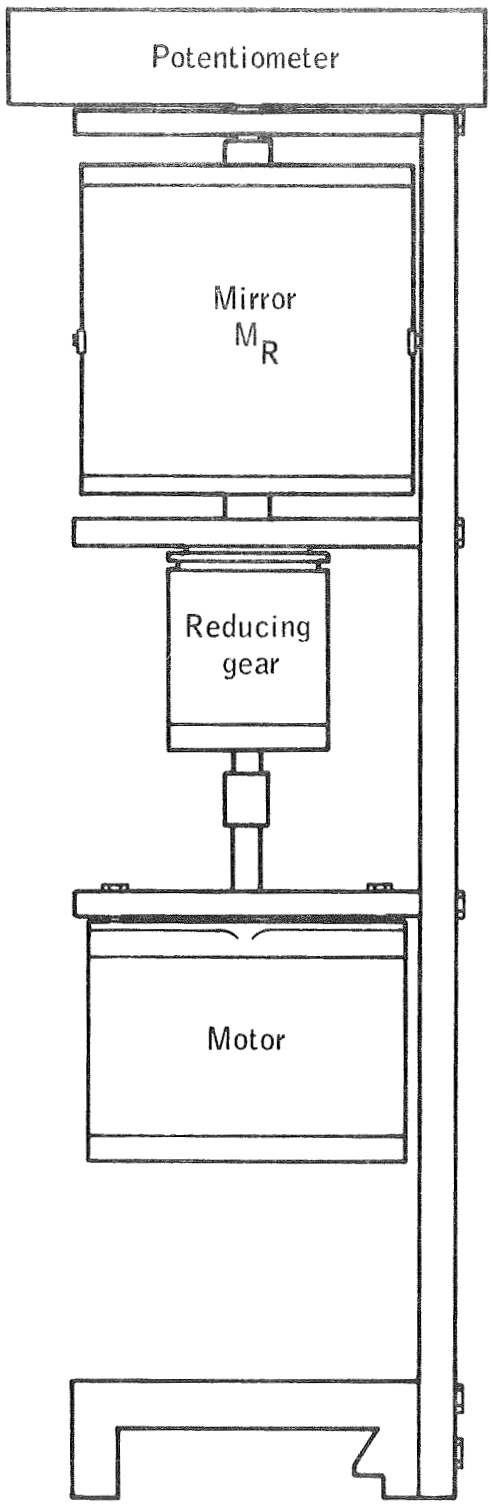

Figure 4.- Position (Abel) scan-drive assembly which rotates the mirror M_R to scan the jet.

The duration of time was determined by the time constant of the amplifier. A longer time constant was used when scanning weak lines. M of the stops completes one scan of the jet. Then, the grating was incremented K steps, corresponding to the desired wavelength increment. The wavelength increment was determined by the breadth of the line and the resolution desired. This whole sequence was repeated L number of times. L was determined by the number of increments required to scan across the line, or part of a line in the case that a single line was scanned piecewise. A piecewise-scan technique was used to obtain a different sensitivity range of the amplifier for different portions of the line. While the motors are stopped at each position during a scan of the jet, the indexer outputs a dc signal to one channel of the recorder. This signaled the computer when to accept the intensity and position data which were recorded in other channels. The position was sensed by the potentiometer previously mentioned. Each fraction of the potentiometer resistance formed one side of a Wheatstone bridge, such that the output of the network was proportional to the position (fig. 5).

The scan-mirror assembly was calibrated by focusing an arc, located at the focal plane, F_R, onto focal plane F_c. The distance the image traveled in a given number of steps was measured several times. The average resulted in a distance of 0.0398 ± 0.0004 cm/step. The grating drive was calibrated by rotating the shaft a certain number of turns (or steps), and recording the corresponding wavelength difference. This resulted in a calibration of 0.0025 ± 1 percent $\mathring{A}$/step.

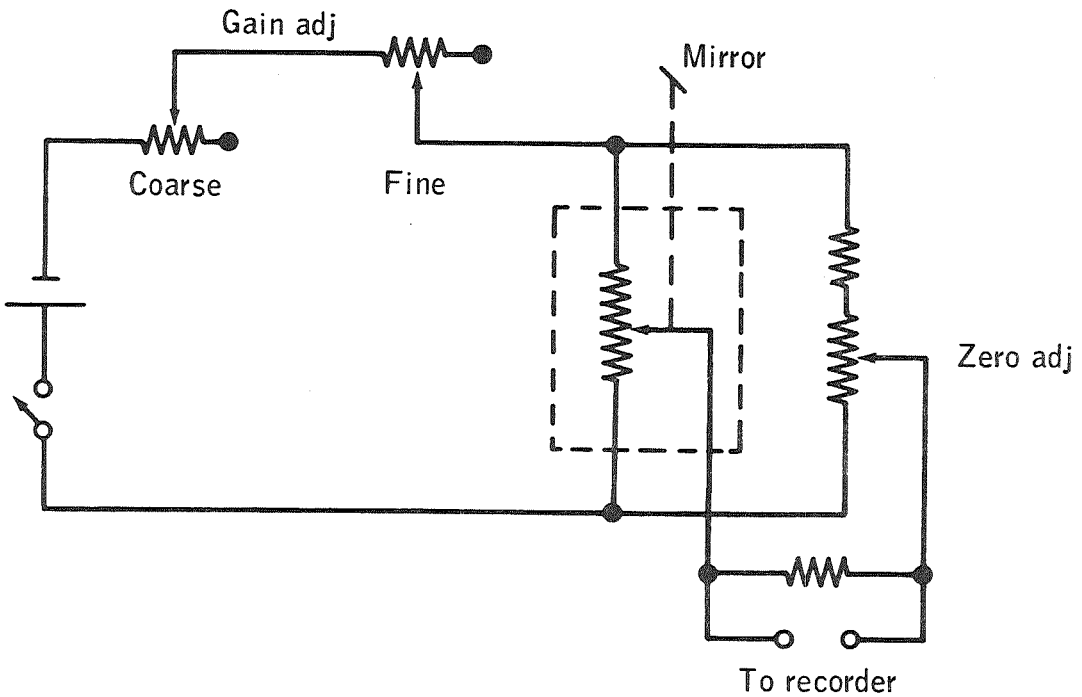

Figure 5.- Abel position-scan read-out circuit. The rotational position of the mirror is sensed by a potentiometer which forms part of a Wheatstone bridge.

3.2 THE SPECTROSCOPIC MEASUREMENTS

The region of the jet in which the spectral measurements were made is shown in figure 6; the rectangular overlay denotes the region scanned by the entrance slit for the Abel-inversion measurements. The width of the rectangle is the height of the slit image projected onto the jet. This region is downstream of an expansion shock wave, which is also shown on the overlay. The outer edge of the jet cannot be seen in this photograph because the exposure was reduced to reveal the shock wave more clearly.

3.2.1 Line Intensities

The total-intensity jet profiles of several lines were measured by the use of the Abel-scan mechanism. These measurements were made for a wide exit slit (205μ) and a somewhat narrower (50μ) entrance slit. This facilitated measuring the total intensity at the peak wavelength (calibrations are given in appendix A).

A scan across the line was made to determine the extent of the line in wavelength and to determine the constancy of the background continuum in the neighborhood of the line. Then, the line was centered on the exit slit and an Abel-scan across the jet was made. Another scan was made of the background continuum a few angstroms from the line. After performing the numerical Abel-inversions of these data, the Abel-inverted-background continuum signal was subtracted from the Abel-inverted total line-intensity signal. The net signal was converted to the total line intensity in proper units by the use of equation (A16).

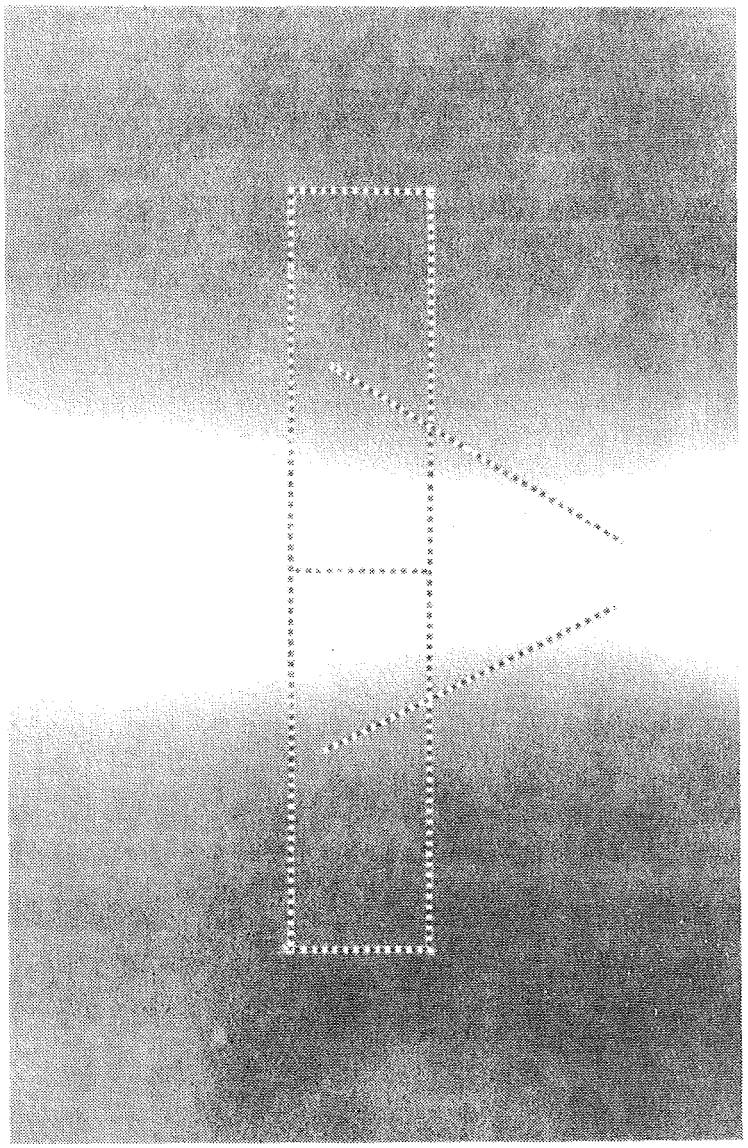

Figure 6.- Photograph of portion of jet which is scanned by the spectrometer. The area scanned is denoted by the superimposed rectangle. The conical expansion shock wave is denoted, and it makes an angle of approximately 30° with the jet axis. The outer edge of the jet is not visible here because the exposure was reduced to enhance the appearance of the shock wave in the original photograph.

3.2.2 Line Profiles

The shapes of a number of line profiles were measured with the center line of the arc jet focused on the entrance slit. This measurement yielded an average profile over a diameter of the jet. Two techniques were used to scan the line. The first method involved a scan of the entire line at a constant stepping rate and on a single amplifier-sensitivity setting. The second method involved a scan of the line piecewise, changing the amplifier sensitivity to take full advantage of the amplifier accuracy on each range. The stepping rate and amplifier time constant were adjusted to obtain the best signal-to-noise ratio of the output consistent with a reasonable rate of acquiring the data. The scan was continued until a minimum or a constant signal was obtained. This minimum constant signal was taken to be the background-continuum signal level. The continuum signal was subtracted from the scan signal to obtain the true spectral profile of the lines. In the case of weak lines, this was difficult to do accurately because the signal becomes less than the noise. Therefore, in the case of weak lines, the accuracy in the far wings suffers. In addition, overlapping of lines caused difficulties in some cases.

3.2.3 Abel-Inverted Line Profiles

To obtain profiles that represented the line shape in a homogeneous plasma (that is, a profile which is not an average over inhomogeneous layers), it was necessary to Abel-invert the profiles. The apparatus and the sequence of the scans are described in Section 3.1.3, The Spectroscopic Instrumentation.

A sample of the data is shown in figure 7; the intensity, position, and command signal are shown. The units are in millivolts compared with time (sec). These raw data were reduced by computer according to the following scheme. The data just mentioned were read off the magnetic tape in digital

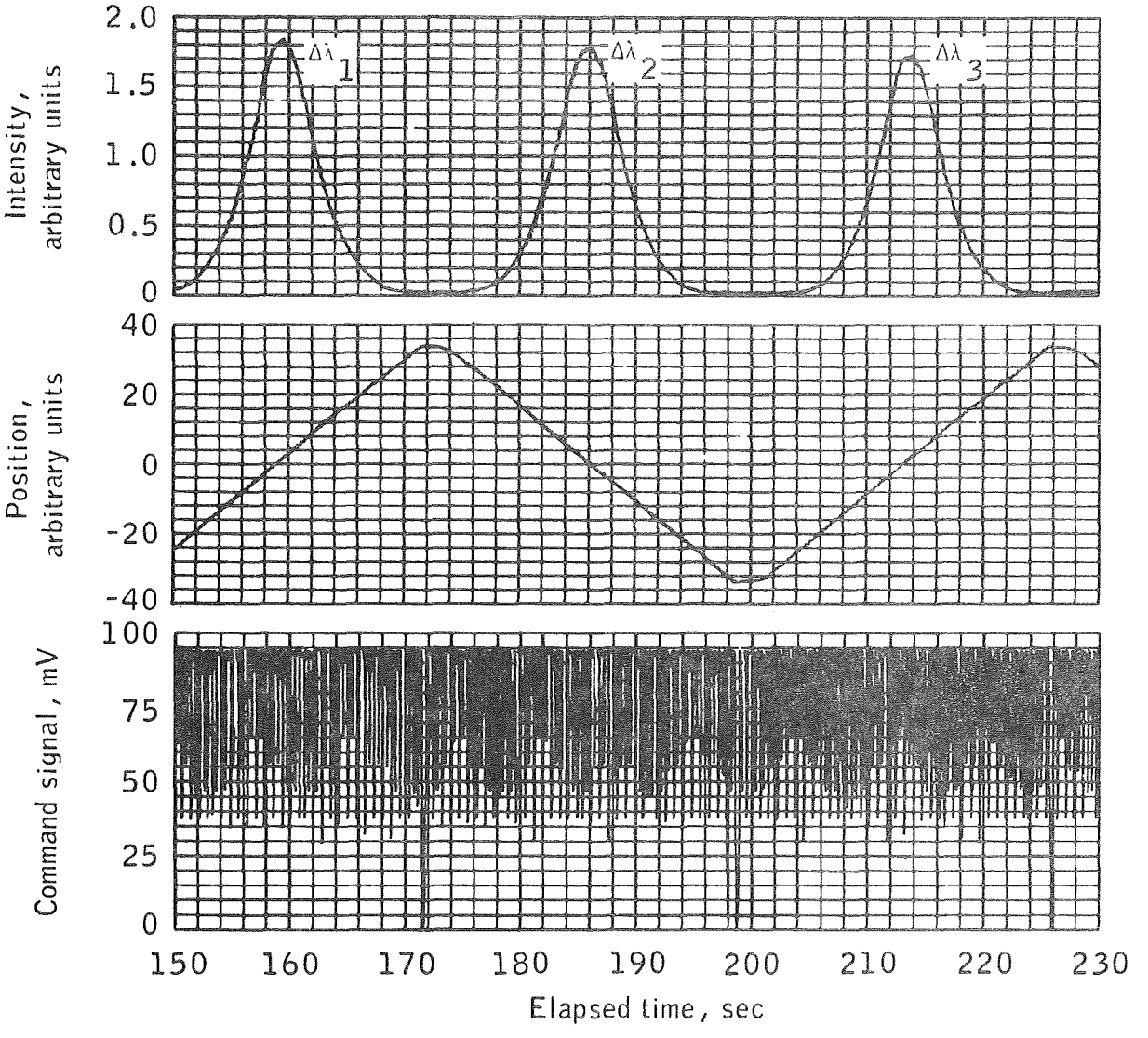

Figure 7.- Sample Abel profile data showing scans of the jet at 3 wavelengths in a line profile out of a total of approximately 100 required to make a complete Abel-inverted line-profile measurement. Fifty-eight steps are in each Abel scan. The command signal >90 mV denotes a point in the scan.

form. Only the data that were flagged by the command channel were sampled. In addition, the position was required to be within the jet radius R. A counter kept track of the number of samples in a scan of the jet so that this process was repeated for each scan. By the use of calibration factors, the raw position data were converted to centimeters and the intensities and corresponding positions were stored on tape for each scan.

To reduce the uncertainty in determining the center of the jet, the center position was found by calculating the centroid

$$y_o = \frac{\sum y_i I(y_i)}{\sum y_i} \tag{40}$$

where $I(y_i)$ is the measured intensity at the corresponding position y_i. The corrected positions were then $y_i' = y_i - y_o$. The light scattered and reflected by the walls of the chamber was accounted for by scanning beyond the jet radius, R, approximately 1 cm above and below the jet, and averaging those measured intensities which were outside the jet diameter. This average was subtracted from the intensity data.

The data were then Abel-inverted according to the method described in appendix B.

3.2.4 Continuum Measurements

The series limit continuum was scanned from 3500 to 3200 Å. This was done by the use of an exit slit width of 75μ. The absolute calibration is described in appendix A. One difficulty in making this measurement was the

rather weak signal in the range of 3300 to 3100 Å and an impurity band OH ($A^2\Sigma^+ - X^2\pi$), which has a bandhead at 3063 Å and is degraded toward the red (fig. 8).

The Abel-inverted absolute-intensity profiles of the jet were measured in the series-limit continuum and in the continuum near each of the Abel-scanned lines, as was mentioned in Section 3.2.1, Line Intensities. These latter measurements were made with an entrance slit of 50μ and an exit slit width of 205μ. Inasmuch as the intensity of the continuum was weak, it was necessary to scan slowly. This required averaging times of 1 to 3 seconds per position to smooth the data.

3.2.5 Instrument Profiles

To account for the instrument broadening in the measured profiles, it was necessary to measure the instrument profile for each configuration that was used in the experiments. It was found that the instrument profile need not be taken into consideration in a number of cases, because many of the lines were much broader than was the instrument profile. The instrument profile can be measured by profiling a spectral line whose width is significantly less than that of the instrument profile. The profile which is measured is the folding of the line profile with the instrument profile

$$I(\lambda) = \int_0^\infty P(\lambda')S(\lambda' - \lambda)\, d\lambda' \qquad (41)$$

where $P(\lambda)$ is the instrument profile and $S(\lambda)$ is the profile of the source line. Because $S(\lambda)$ is much narrower than $P(\lambda)$, it acts like the Dirac delta function in the integration, so that when carrying out the integration

Figure 8.- Photographic spectra of arc jet. Parts (a) and (d) are spectra of a mixture of 97 percent He and 3 percent H_2. Parts (b), (c), (e), and (f) are pure helium spectra, made with differing exposures and slit widths to show both faint and strong lines, respectively. Parts (d), (e), and (f), are the longer wavelength extensions of parts (a), (b), and (c), respectively. The sharp, faint lines adjacent to the primary spectra are made with a He low-pressure discharge for reference. The "Forbidden" designation refers to the n^3P Stark component of the corresponding $2^3P - n^3D$ lines.

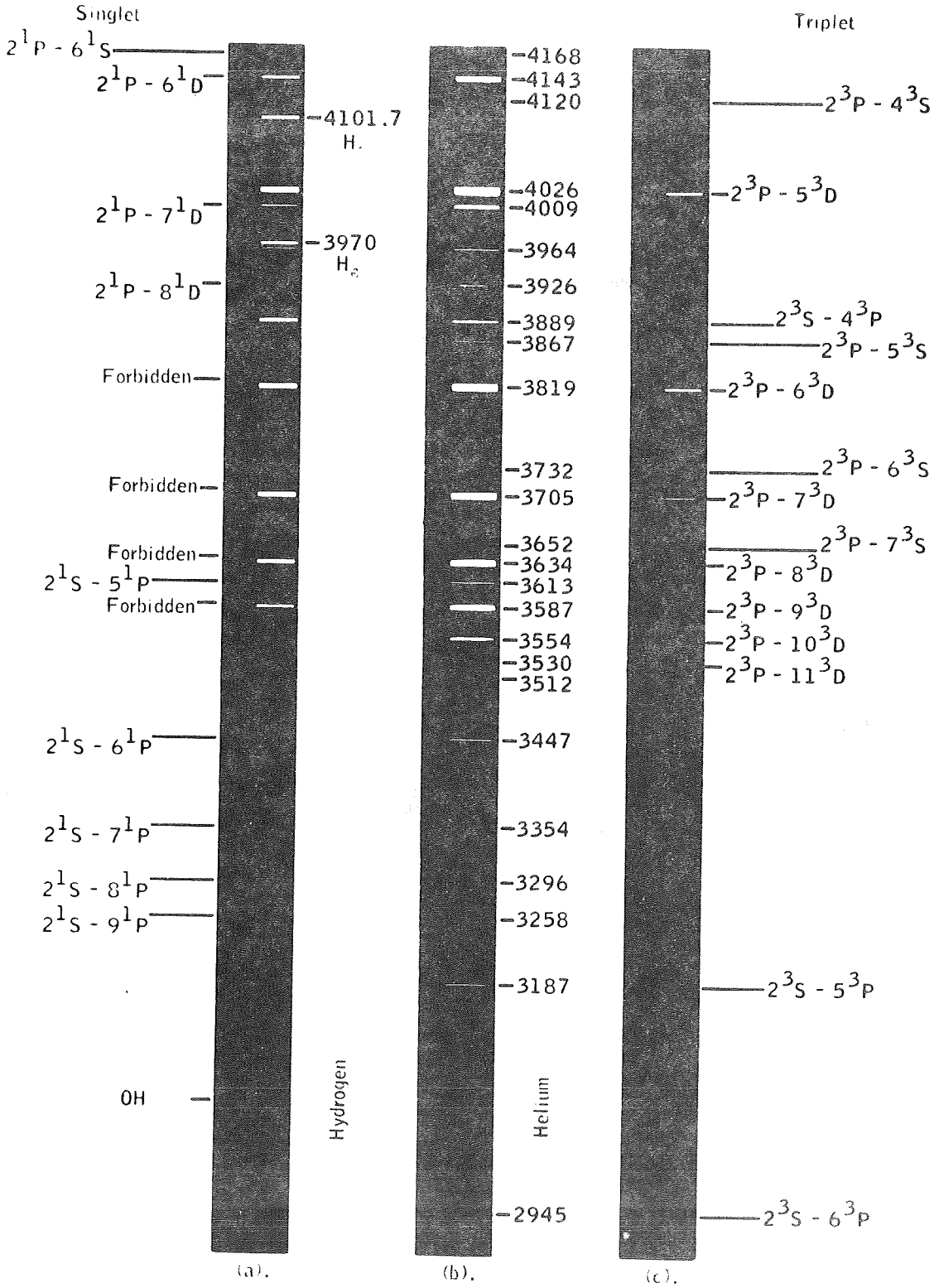

NASA S-69-27357

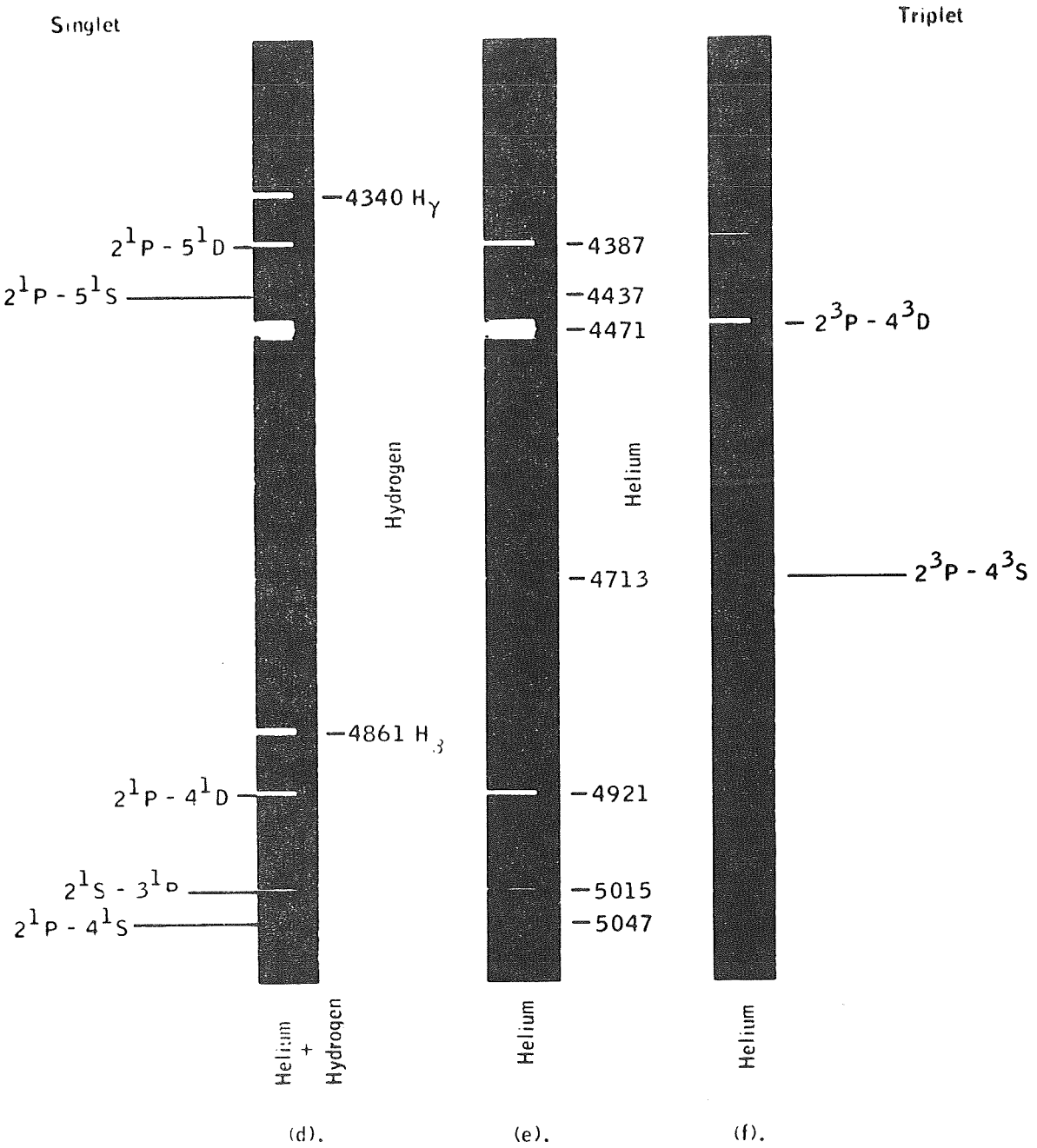

Figure 8.- Concluded.

$I(\lambda) = P(\lambda)$ is obtained. This justifies the assumption that this measured profile can be used as the instrument profile.

The line used in these experiments for measuring the instrument profile was the 4358-Å line of a low pressure Hg^{198} radiofrequency discharge. The line from this source is one of the narrowest available, having a width of only approximately 0.004 Å. The lamp was excited by a 60-watt transmitter operating continuously at a frequency of approximately 28 MHz.

To verify that the spectrometer was correctly alined and that the source was indeed narrow, the widths of the measured profiles were compared with those calculated theoretically. The theoretical curves of Rolf Brahde (ref. 21) were used. These curves are the result of folding the entrance and exit slits with the diffraction profile of a rectangular opening. The grating was the limiting optic in this case.

The measured instrument full half widths are compared with the theoretical in table III. The measured values are consistent with the theoretical, except in the case of the 25μ slit. Good alignment was essential for obtaining the narrowest and most symmetrical profiles, and the focus was also critical.

TABLE III.- COMPARISON OF THE EXPERIMENTAL AND THEORETICAL INSTRUMENT PROFILE FULL WIDTHS AT HALF HEIGHT

Entrance slit, μ	Exit slit, μ	Measured, Å	Calculated, Å	
			(a)	(b)
10	10	--	0.051	0.075
25	10	0.15	0.126	0.14
25	25	0.25	0.126	0.15
75	75	0.44	0.379	0.43
		λ = 4358 Å		

[a]Calculated by the use of simple rectangular-slit approximation not taking diffraction into account.

[b]Calculated taking diffraction into account (ref. 21).

4.0 DISCUSSION OF RESULTS AND COMPARISON OF EXPERIMENT WITH THEORY

4.1 LINE INTENSITIES AND TEMPERATURE PROFILES

4.1.1 Determination of Temperature Profile from Line Intensities

To determine the electron temperature distribution in the jet as a function of radius, eight narrow helium lines were scanned in wavelength using a wide exit slit. These measurements were made at a single jet position through the jet center line. From these measurements, an effective spectral slit width w was determined by use of the relation (appendix A)

$$w = \frac{\int v(\lambda)d\lambda}{v(\lambda_o)} \tag{42}$$

Use of a wide exit slit and this calibration facilitated the use of a single peak-wavelength measurement at each position. The character of the background continuum was also determined, and it was found that the continuum essentially was constant in the neighborhood of each line.

The jet was scanned perpendicular to the axis to obtain the radial-intensity profile of each line by Abel-inversion. Similarly, the radial profile of the background continuum of each line was obtained. The resulting intensities were calibrated by use of the methods described in Section 3.2.1, Line Intensities and appendix A. The temperatures at 10 radial positions were determined by making a least-squares fit of the data for each radius to the logarithm of equation (1). The slopes of these straight lines equal 1/KT. The radial temperature distribution is shown in figure 9. The error bars denote the standard deviations, which at the center line, amount to an error

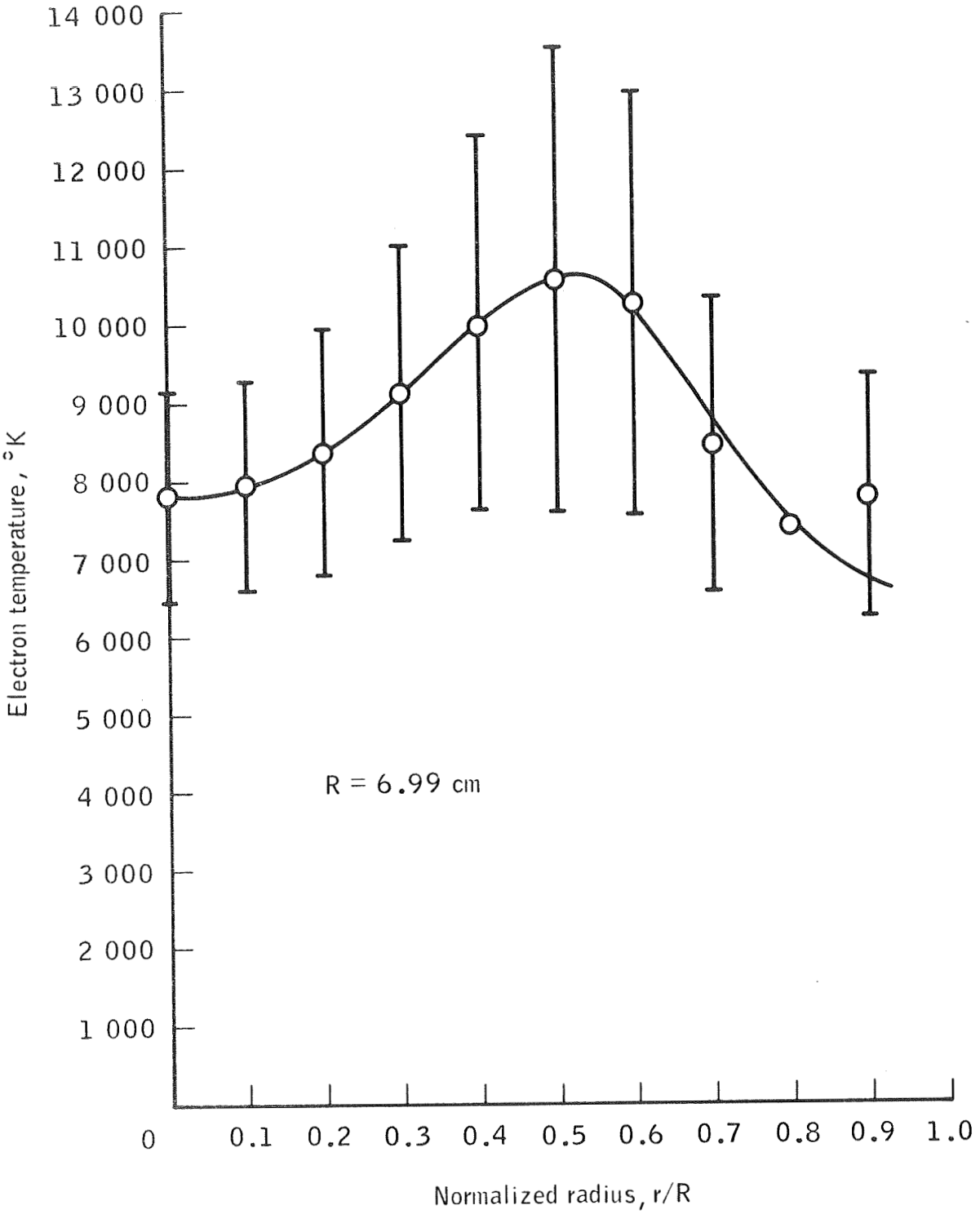

Figure 9.- Electron temperature, determined from Boltzmann plots corresponding to each radius r/R. Error bars denote the standard deviation.

of 17.3 percent. The determination of the standard deviation was made using standard error-analysis techniques such as those found in Barford (ref. 22). These errors are based on the scatter in the final results of the calibrated intensities, and, therefore, they include all sources of random errors. It is assumed that any systematic errors are small in comparison. Within the limits of experimental error, there was no curvature to the plot of log $(I\lambda^3/gf)$ compared with E_u, where I is the relative total line intensity, g is the statistical weight of the lower energy level, f is the absorption-oscillator strength, and E_u is the upper energy level of the transition. The fact that there was no curvature is consistent with the assumption of local thermodynamic equilibrium of the electrons in the energy levels involved. The lines involved in the temperature determination and the associated absorption-oscillator strengths f, statistical weights of the lower energy-level g, and the energy in cm^{-1} of the upper energy level E_u are shown in Table IV. The oscillator strengths given here are from Green, et al. (ref. 23), and they are the most recent and most extensive tables available. The oscillator strengths of Trefftz, et al. (ref. 24) are consistent with these, but their tables are less extensive.

4.1.2 Optical Thinness Verification

To verify that the optical thinness assumption is valid, an approximate value of the optical depth was calculated for the $2^3P - 6^3D$ line and

for the $2^3S - 4^3P$ line. Griem (ref. 13) gives the following expression for the optical depth for a cylindrical source.

$$\tau(y) = 2\int_0^{\left(R^2 - y\right)^{1/2}} k'dx = \int_y^R \frac{\varepsilon(r)}{I_T} \frac{rdr}{\left(r^2 - y^2\right)^{1/2}} \tag{43}$$

The expression is the integral of the absorption coefficient along the path of observation. $\varepsilon(r)$ is the emission coefficient, determined from an Abel-inversion of the intensity scan of the line, and I_T is the Planck function

$$I_T(r) = \frac{2hc^2}{\lambda^3}\left[\exp\left(\frac{hc}{\lambda kT(r)}\right) - 1\right]^{-1} \tag{44}$$

The temperature distribution $T(r)$, which is shown in figure 9, was fit by the least-square technique to a power series.

$$T(r) = \sum_{n=0}^{7} b_n r^n \tag{45}$$

This approximate temperature-distribution function and the function obtained from the Abel-inversion calculation were substituted into equation (43). A numerical evaluation of the integral was performed. The resulting optical depths were 3×10^{-4} for the $2^3P = 6^3D$ line and 2.5×10^{-3} for the $2^3S - 4^3P$ line. These values are much smaller than unity. Therefore, the assumption that the jet is optically thin is justified for these lines. Because these are low quantum number lines, the jet was assumed to be optically thin for all lines that were measured.

TABLE IV.- LINES AND CORRESPONDING ATOMIC PARAMETERS

Wavelength, Å	Transition	g	f (a)	E_u, cm^{-1} (b)
3187.7	$2^3S - 4^3P$	3	0.0271	191217
3613.6	$2^1S - 5^1P$	1	.0231	193942
3652.	$2^3P - 8^3S$	9	.00063	196461
3732.8	$2^3P - 7^3S$	9	.00102	195868
3964.7	$2^1S - 4^1P$	1	.0506	191493
4120.9	$2^3P - 5^3S$	9	.00373	193347
4437.6	$2^1P - 5^1S$	3	.00317	193664
4713.	$2^3P - 4^3S$	9	.0104	190298

[a]Oscillator strengths are from velocity calculations by Green, Johnson, and Kolchin (ref. 23).

[b]Energy levels are from Martin (ref. 16).

4.2 ABSOLUTE CONTINUUM MEASUREMENTS AND THE ELECTRON-DENSITY PROFILE

The electron density profile of the jet was found by solving equation (2) for N_e^2. The assumption was made that $N_e = N_i$. The following data were used in calculating the continuum emission coefficients. The photoionization cross sections were those calculated by Anderson and Griem (ref. 11), and the bound-free averaged Gaunt factors $g_n(\lambda)$ are those calculated by Karzas and Latter (ref. 12). The free-free average Gaunt factor was set equal to a constant $g_f(\lambda,T) = 1.1$. The results of the calculations are plotted in figure 10 for $T = 7800°$ K and $N_e = 1.38 \times 10^{15}$ cm^{-3}. Measured values of the emission coefficient were combined with equation (2), giving the relationship

$$N_e^2(r) = \frac{\varepsilon_m(\lambda,r)}{\left[\varepsilon\left(\lambda,N_e,T\right)/N_e^2\right]_c} \tag{46}$$

where $\varepsilon_m(\lambda,T)$ is the measured emission coefficient and $[\varepsilon(\lambda,N_e,T)/N_e^2]_c$ is the theoretical value obtained from equation (2). Equation (2) was programed for computation on a digital computer. Although $\varepsilon(\lambda,N_e,T)/N_e^2$ is a function of N_e, its dependence on N_e is so small at most of the wavelengths of interest that it is negligible over the range of densities involved. Therefore, only an order of magnitude guess was needed for the first iteration.

These emission coefficients were calculated as a function of radius at the measured wavelengths by the use of the temperature distribution shown in figure 9, and an initial electron density of 6×10^{14} cm^{-3}. Then, from equation (46), electron density distributions were calculated for each

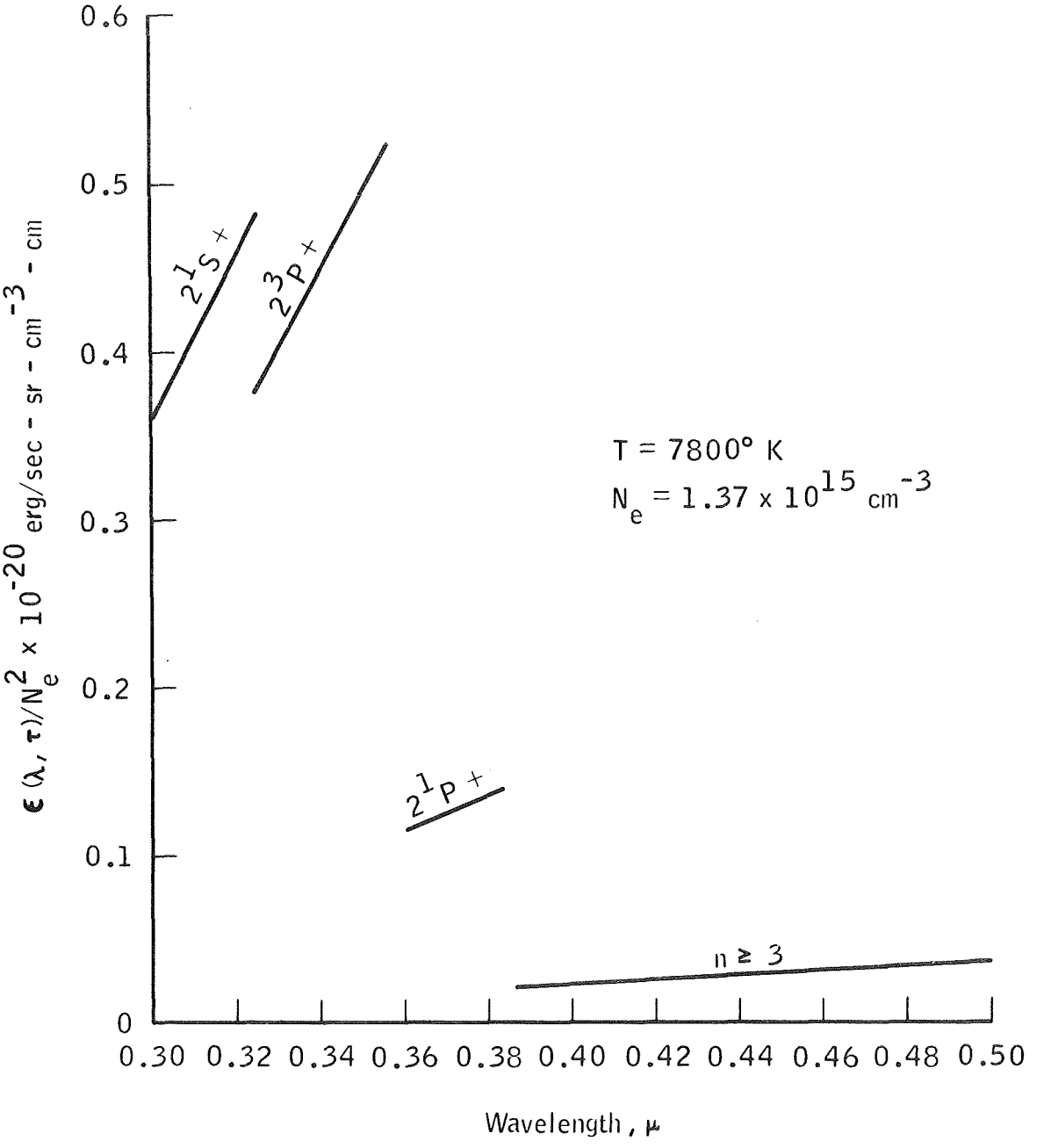

Figure 10.- Calculated continuum-emission coefficients divided by N_e^2. The notation + beside the term designations implies that the curve includes the continuum resulting from transitions into that level plus all other energy levels above it.

wavelength and were normalized to unity at $r = 0$. The measurements for each wavelength were then averaged for each value of r to obtain a first iteration radial-electron density distribution.

Using this distribution for N_e and $T(r)$ distribution, a second set of $\frac{\varepsilon(\lambda, N_e, T)}{N_e^2}$ was calculated. From these, the average radial-electron density distribution was determined as in the first iteration.

The normalized profile was calculated from Abel-scans of the continuum near the wavelengths given in table IV, plus the wavelength 3400 Å, which is in the $2^3P - n^3D$ series limit continuum. The center line or peak value was determined from Abel-inverted measurements at 3184, 3400, 4127, 4442, and 4718 Å plus noninverted measurements at 3250, 3280, and 3475 Å. Here, the center-line emission coefficient was obtained from the center-line intensity by dividing by the mean effective thickness t of the plasma, as shown in the expression $\varepsilon(0) \approx I(0)/t$. The value $t = 3.80$ cm was obtained from the average value of $I(0)/\varepsilon(0)$ for each Abel-inverted continuum measurement. The center-line electron density was found to be 1.38×10^{15} cm^{-3} ± 12.5 percent. The electron-density profile is shown in figure 11. Error bars are plotted at r/R equal to 0, 0.3, 0.6, and 0.9.

A portion of the series limit continuum and the merging lines are plotted in figure 12. The intensity measurement is for $y = 0$ (along a diameter), and the scale is in arbitrary units, with no account made for the change in sensitivity of the spectrometer with change in wavelength.

4.3 REMARKS ON THE ABEL-INVERSION TECHNIQUE

The technique for scanning the jet and spectrum seemed well suited for these experiments because the variable scan rates permitted scanning

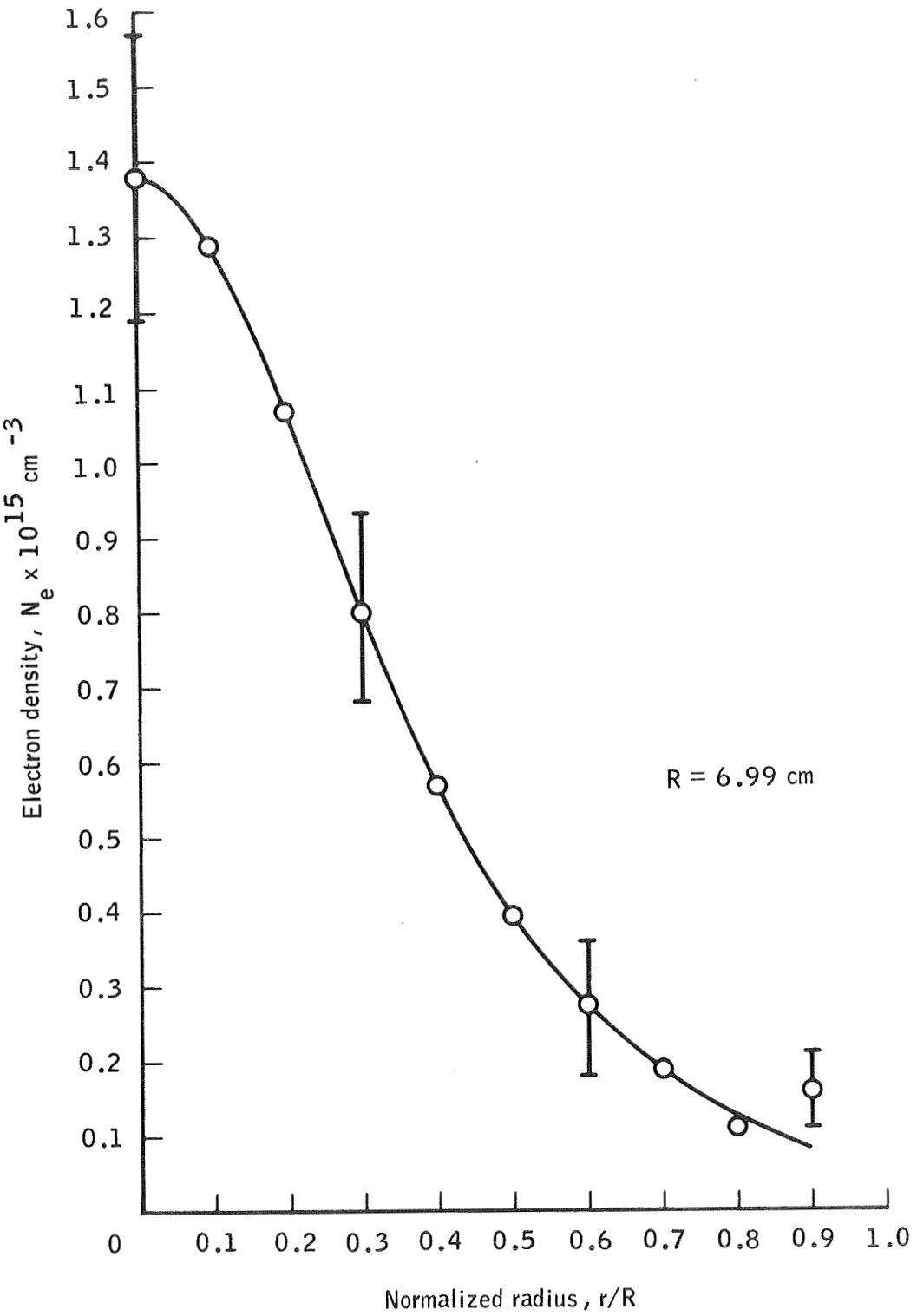

Figure 11.- The electron density distribution in the jet; error bars denote the standard error.

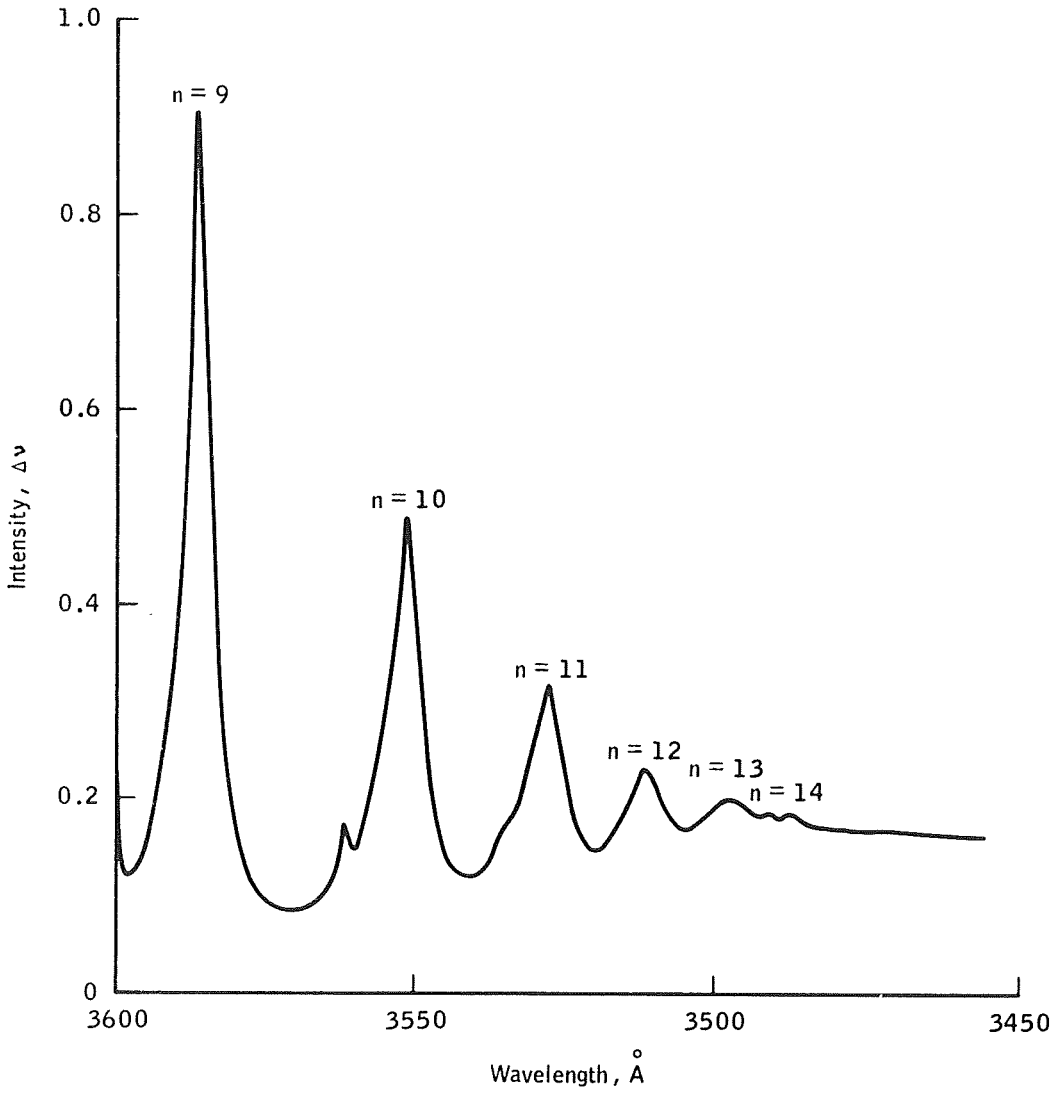

Figure 12.- A scan of the 2^3P - n^3D series limit of He, uncompensated for changes in system spectral sensitivity. The last discernable line in the line-of-sight measurement is the n = 14 line.

different parts of the line profile at rates which give the optimum signal averaging and resolution. For example, in the core of the line where the signal is strongest but higher resolution is required, one could scan rapidly with small $\Delta\lambda$. However, out on the wings where there is less need for high resolution, one could scan more slowly a fewer number of points with larger $\Delta\lambda$. This technique permitted a fairly precise knowledge or measure of the positions in the scan for each wavelength increment. The estimated error in position was about 2 percent of the radius R. The curve fit of the data in the numerical Abel-inversion yielded a standard deviation of less than 1 percent of the center-line intensity near the line core, to approximately 2 percent on line wings and in the continuum. The fractional error increased near the edge of the jet where the intensity is small. The major sources of error are related to the jet itself, rather than to the measurement or numerical techniques. First, the jet is not strictly symmetrical and deviations from cylindrical symmetry are largest near the edge of the jet. There was sometimes a factor of two difference in the intensity near one edge compared with the other edge. The technique of fitting the data to symmetrical curves effectively averaged the data. In the case of the Abel-inverted line profiles, the antisymmetrical component was calculated, but there were large deviations in the curve fit caused by a poor choice of functions for the curve fit. For that reason, these data are not presented. The other major source of error in the radial-intensity profiles stems from uncertainty in the overall jet diameter. It was difficult to determine accurately where the intensity of the jet decreased to zero because of background-scattered radiation. Both visually measuring the luminous diameter of the jet and a stagnation-pressure probe survey (fig. 13) yielded

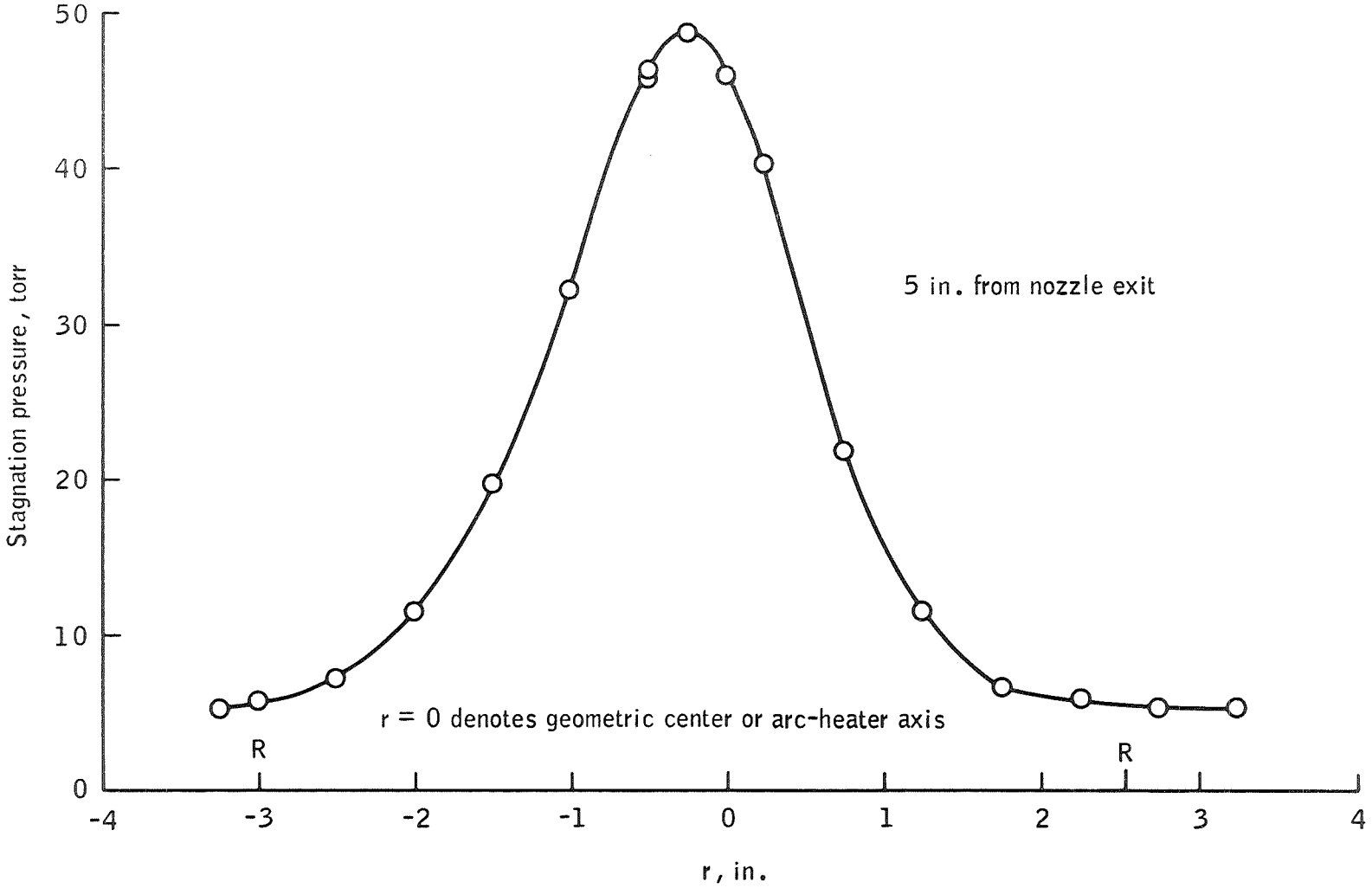

Figure 13.- Stagnation-pressure distribution measured with a 0.5-inch-diameter probe. The center of the distribution is approximately 0.25 inch below the arc-heater axis.

a diameter of 14.0 ± 1.2 cm; hence, the standard error in the radius R was ± 4 percent. This uncertainty in the radius yielded a similar uncertainty in the Abel-inverted intensity N(r). The combination of the errors just mentioned yields a net uncertainty of about 5 percent near r = 0, and this uncertainty increases to about a factor of two for weak parts of the spectrum near the edge of the jet.

4.4 HELIUM LINE-BROADENING AND QUASISTATIC-THEORY COMPARISON

Experimental line profiles were measured by the use of two techniques. In the first technique, the profiles were averaged over a diameter of the jet by a line-of-sight measurement. In the second method, the profiles were Abel-inverted by scanning both in wavelength and position.

4.4.1 Averaged (Non-Abel-Inverted) Line Profiles

The averaged profiles are not suitable for precise comparison with the theory because they are averages and an accurate comparison would require that the theoretical profiles also be averaged over the temperature and electron-density distributions along a diameter of the jet. Such theoretical calculations would be very lengthy even on a computer, and the results probably would not be very helpful in determining the validity of the theory in detail. However, for a rough comparison, the experimental average profiles and the theoretically calculated profiles are presented in figures 14 to 18 for the triplet diffuse lines with principle quantum numbers n = 4 to n = 8. In these comparisons, the mean temperature 8750° K and a perturber density 1.58×10^{15} cm^{-3} (which is two times the root-mean-square electron density)

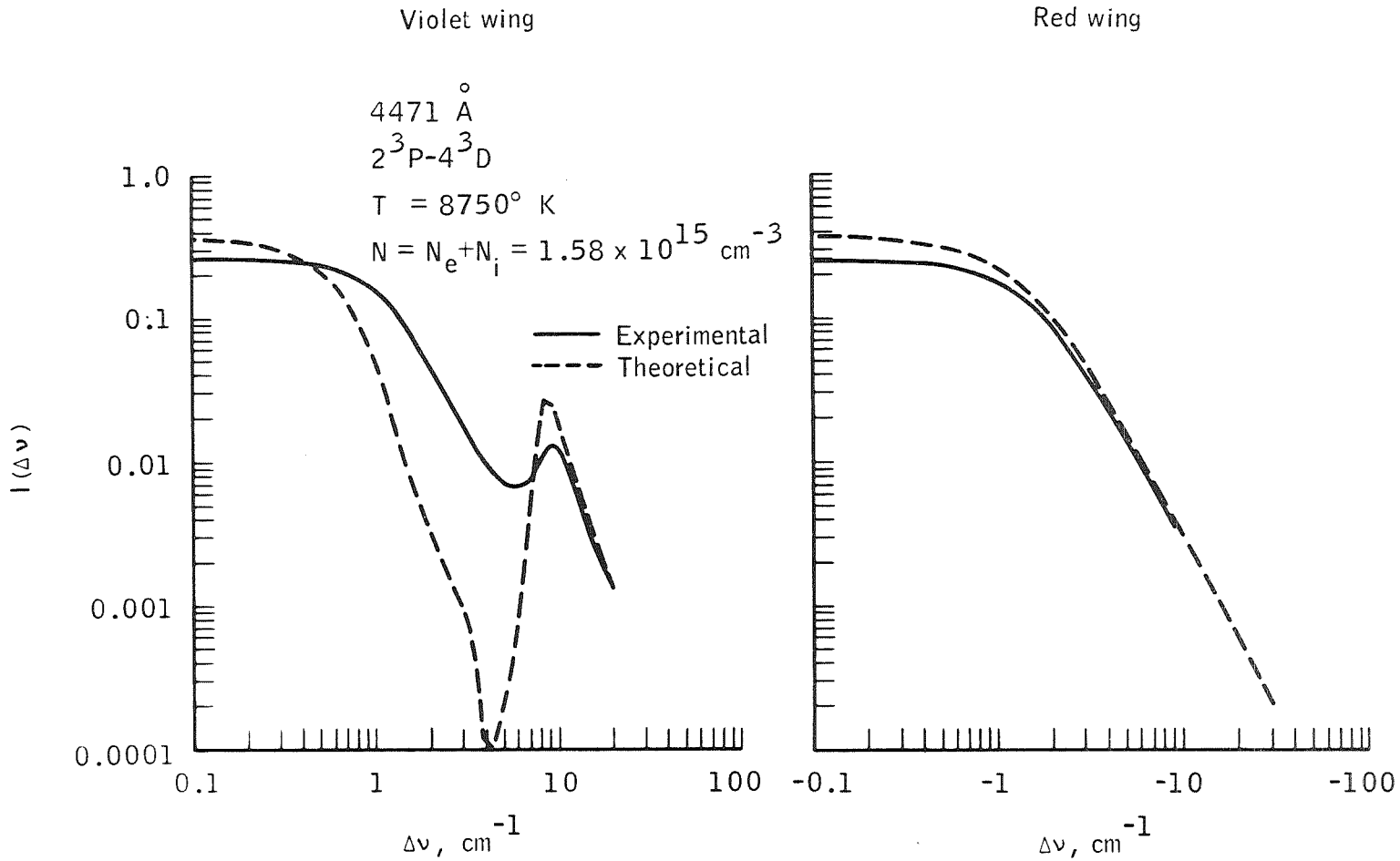

Figure 14.-Non-Abel-inverted experimental profile and quasistatic profile folded with instrument and Doppler profiles 2^3P - 4^3D, normalized to total intensity.

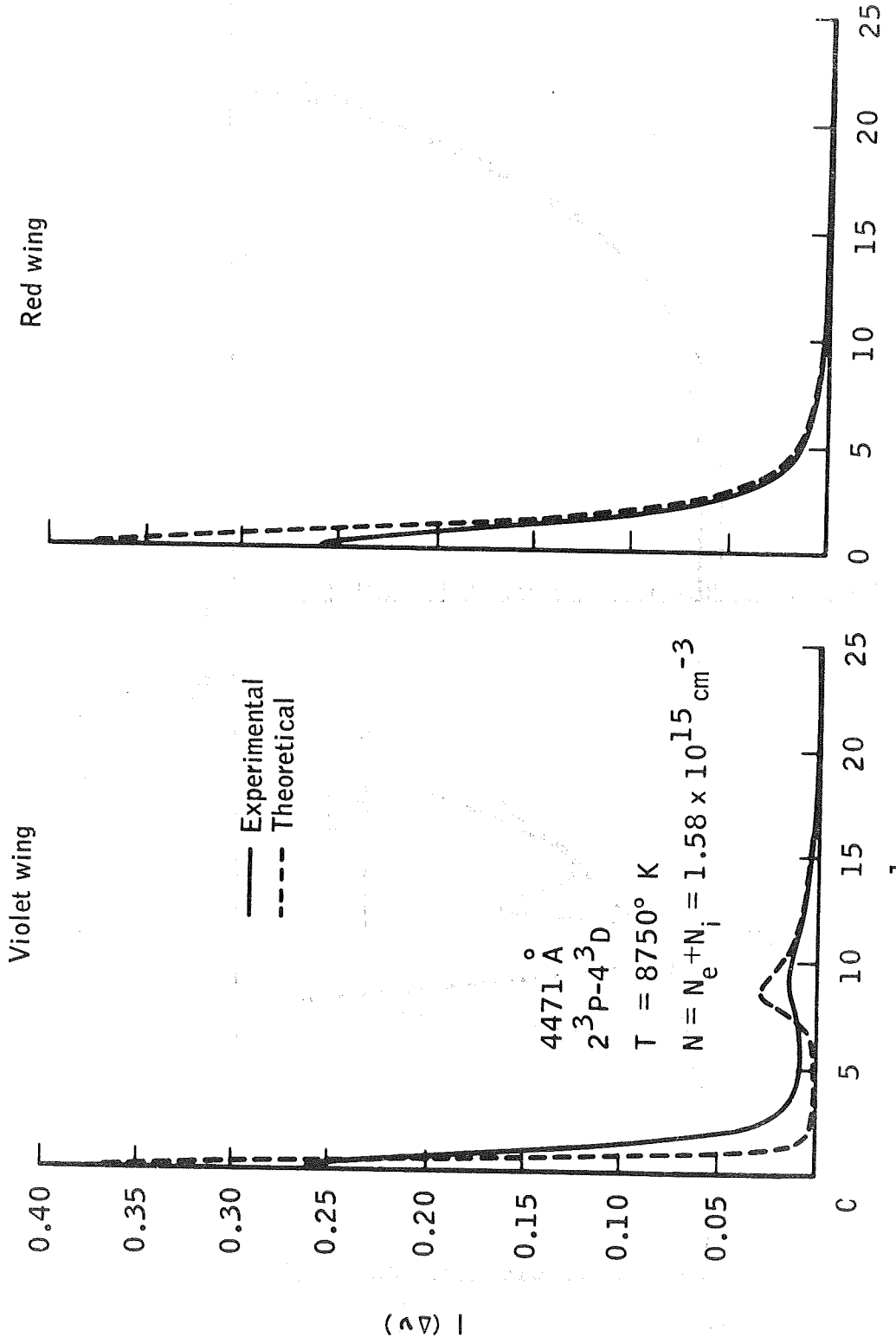

Figure 14.- Concluded.

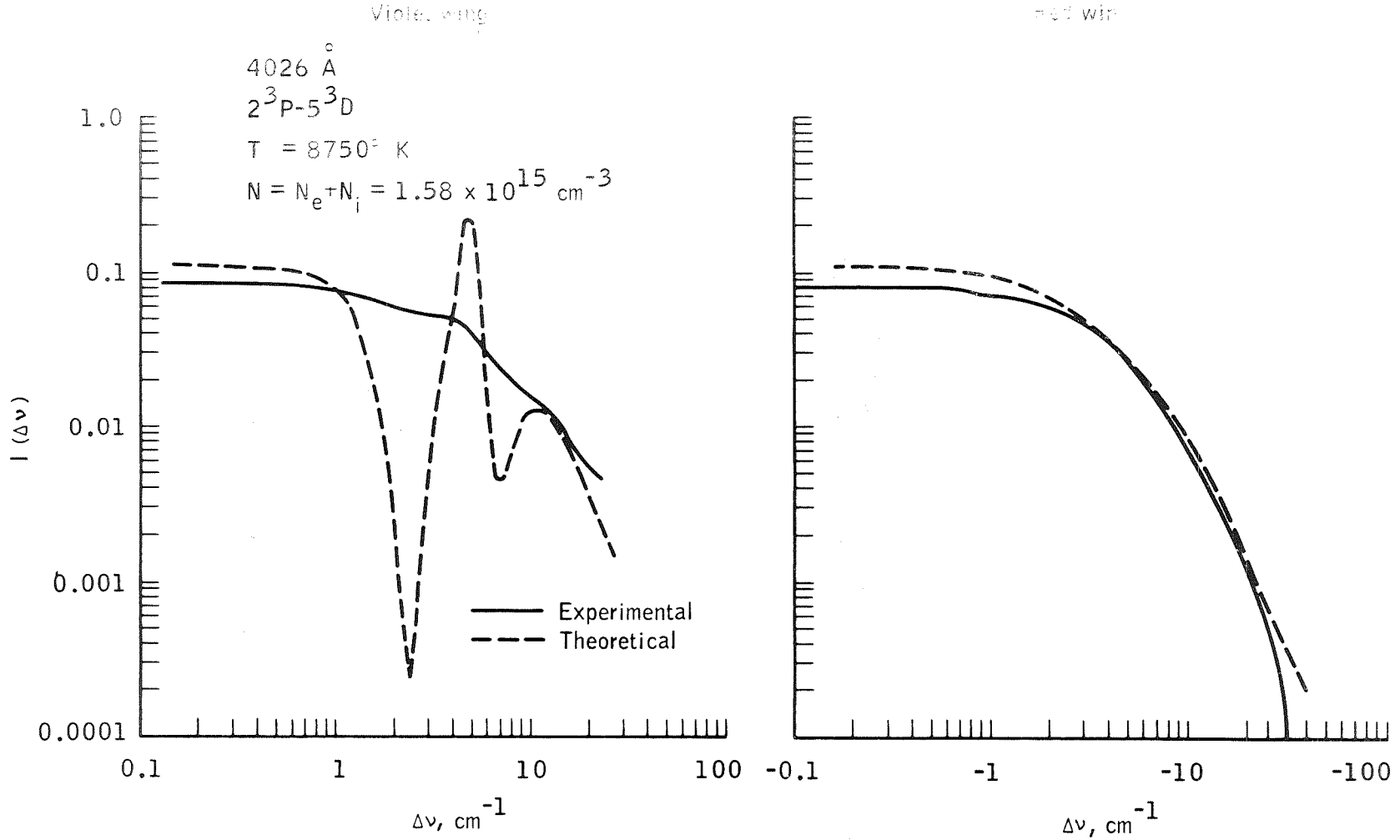

Figure 15.- Non-Abel-inverted experimental profile and quasistatic profile folded with Doppler profile for 2^3P - 5^3D, normalized to total intensity.

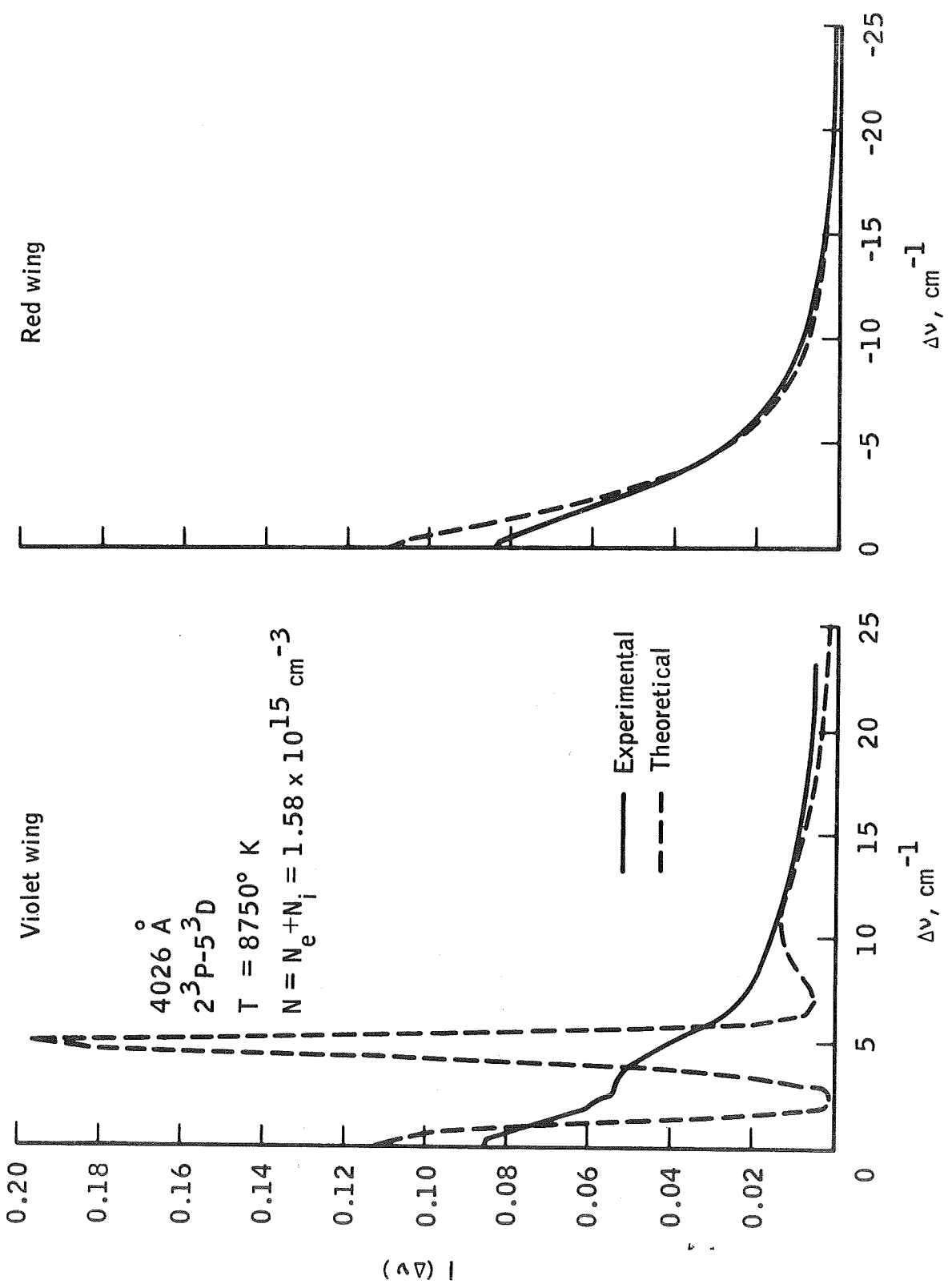

Figure 15.- Concluded.

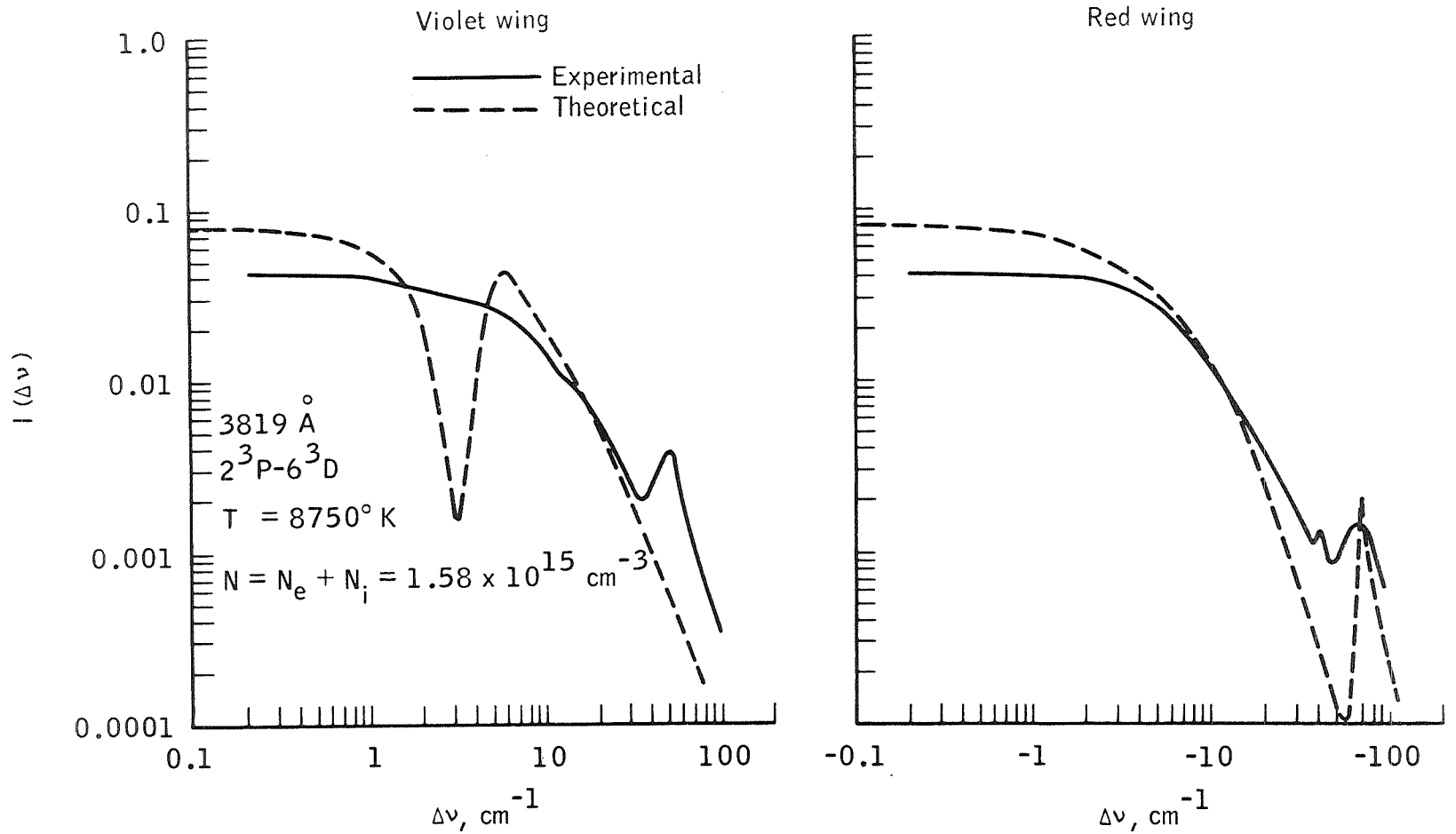

Figure 16.- Non-Abel-inverted experimental profile and quasistatic profile folded with Doppler profile for $2^3P - 6^3D$, normalized to total intensity.

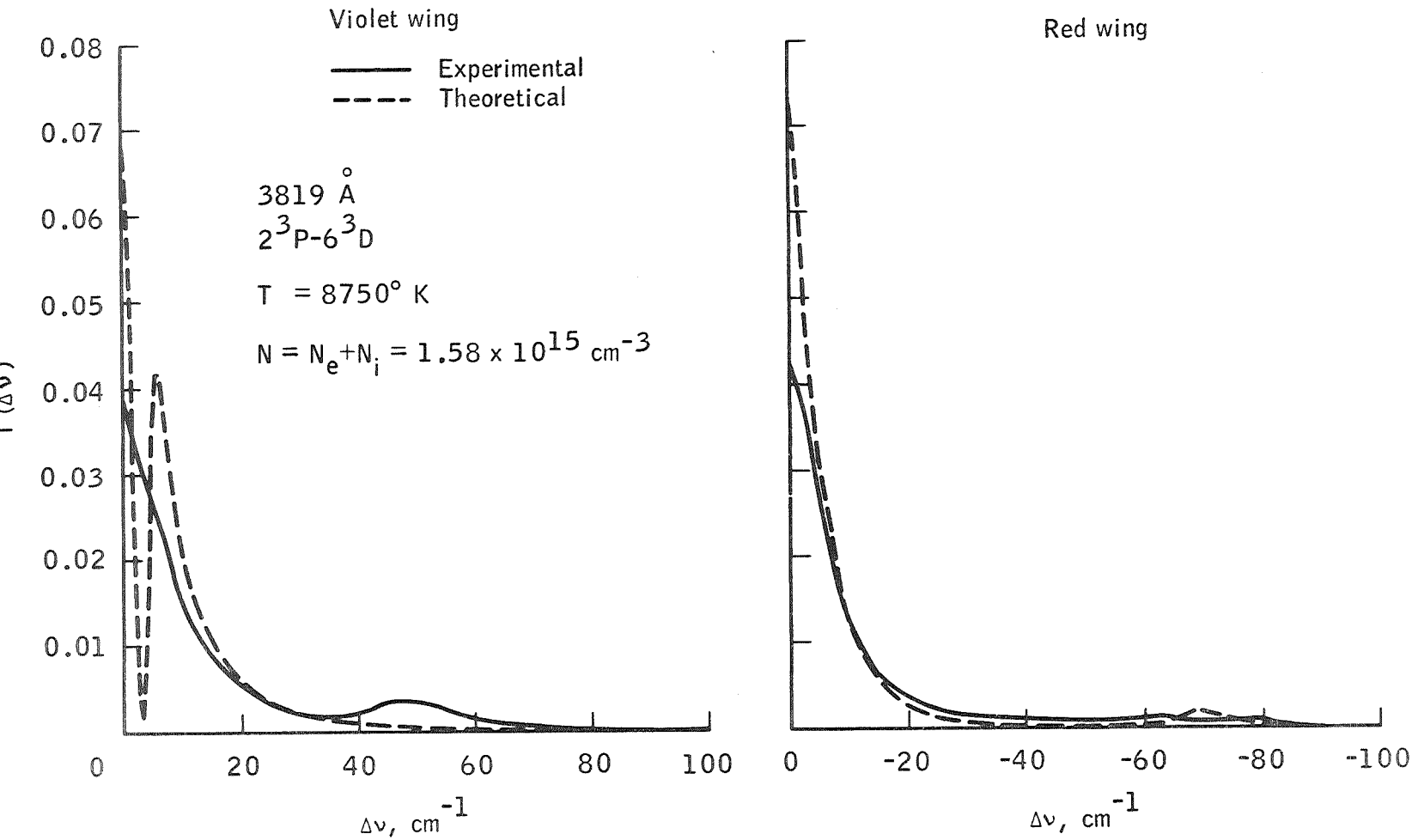

Figure 16.- Concluded.

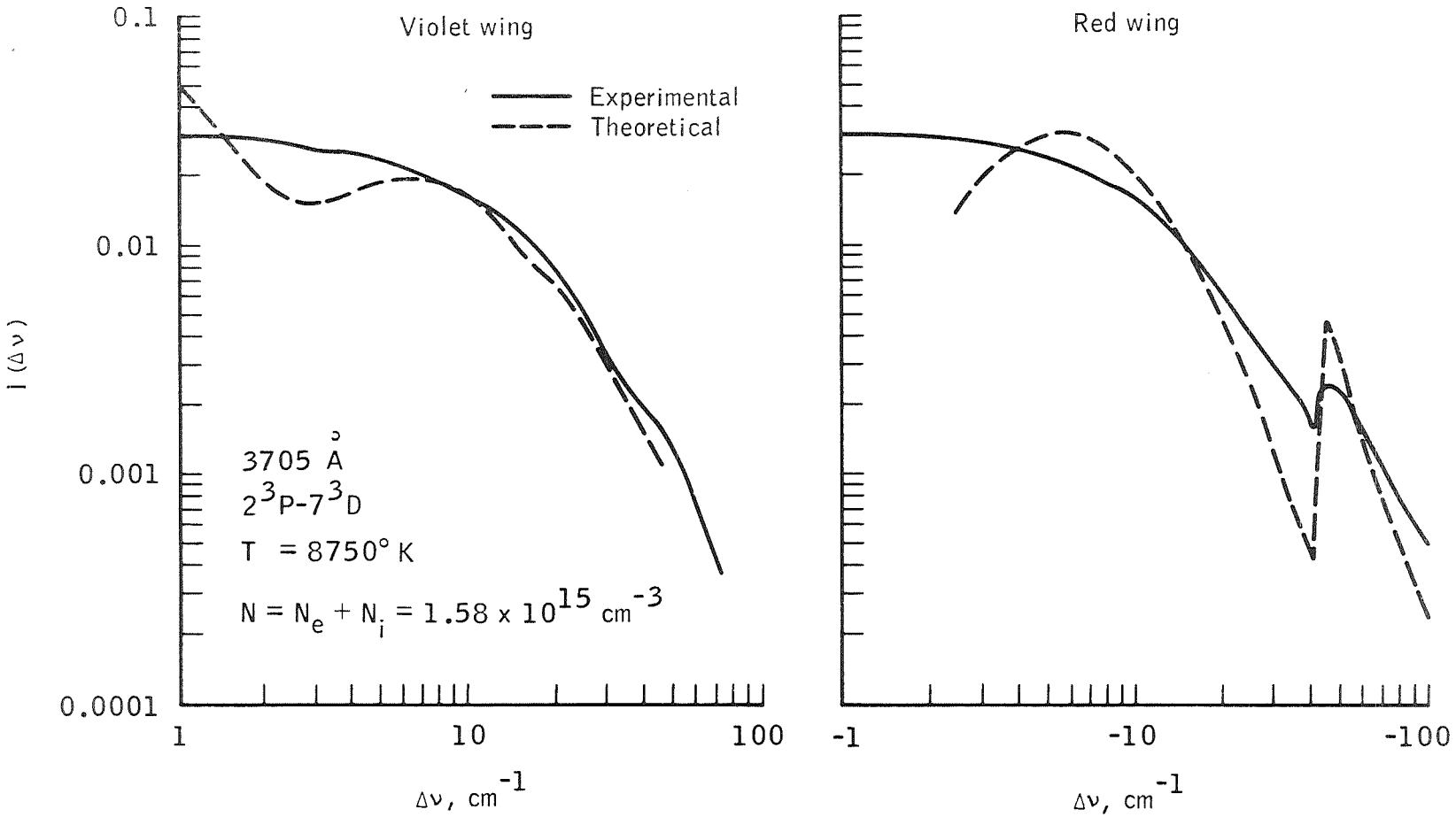

Figure 17.- Non-Abel-inverted experimental profile and quasistatic profile folded with Doppler profile for 2^3P - 7^3D, normalized to total intensity.

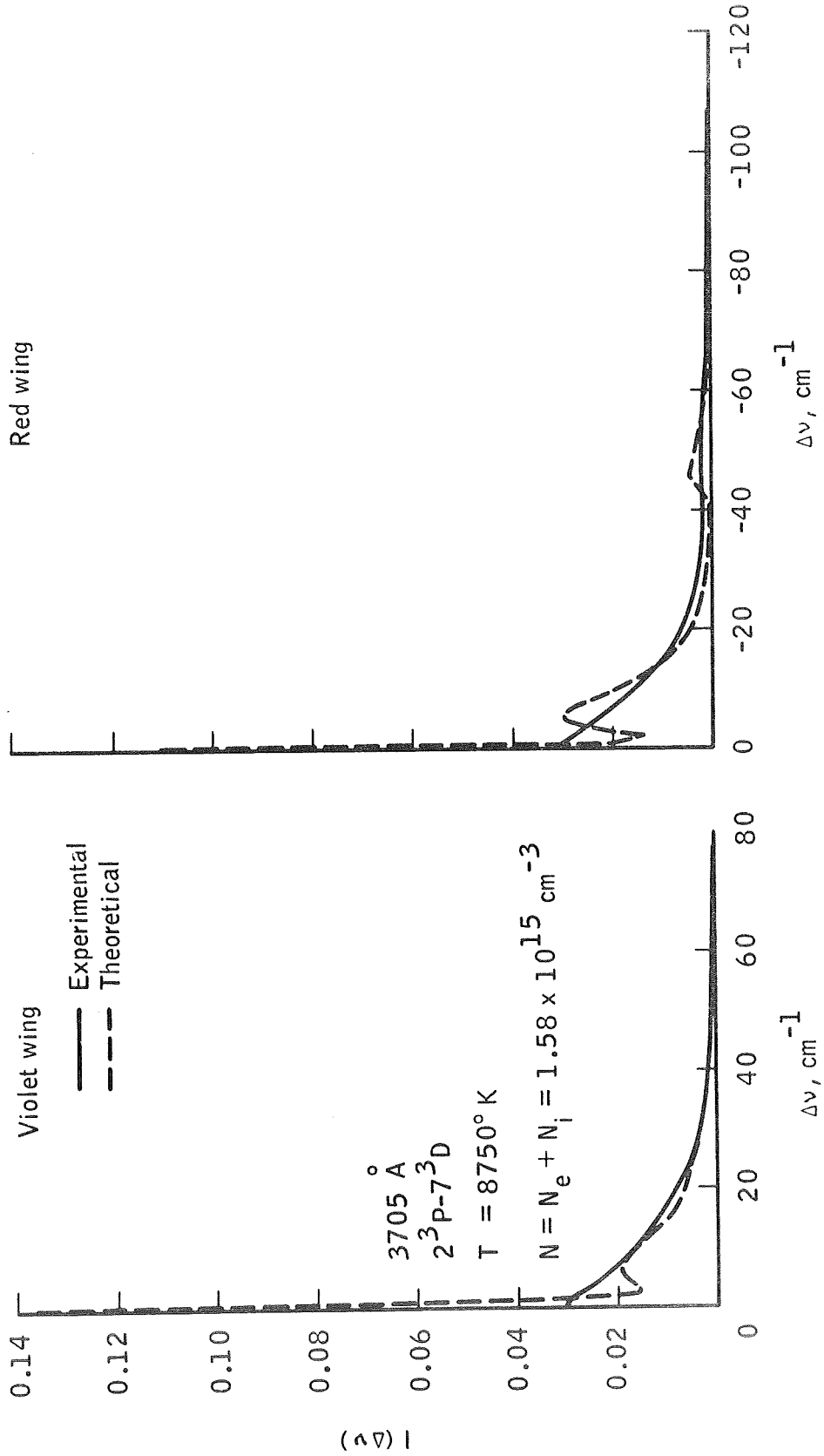

Figure 17.- Concluded.

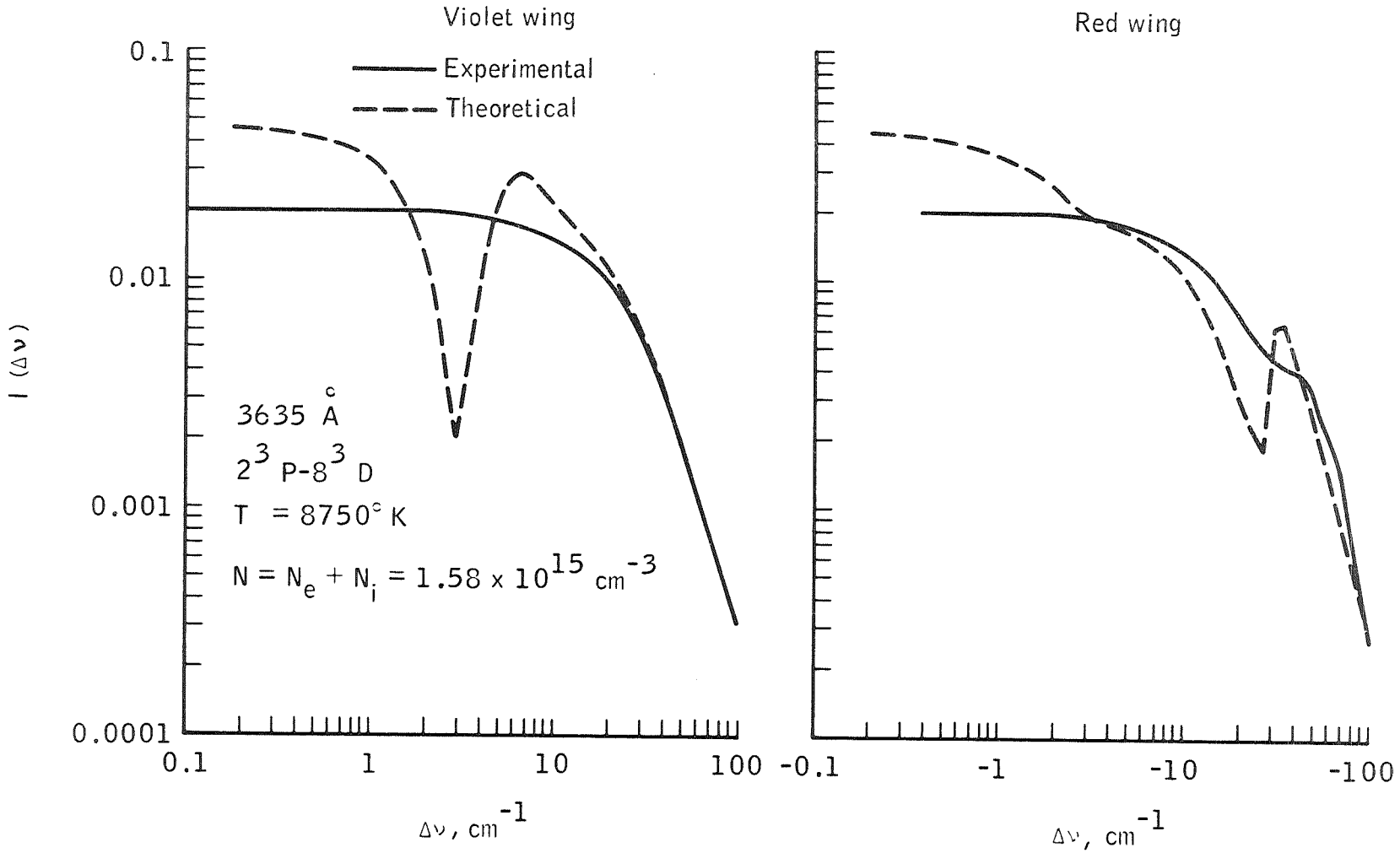

Figure 18.- Non-Abel-inverted experimental profile and quasistatic profile folded with Doppler profile for $2^3P - 8^3D$, normalized to total intensity.

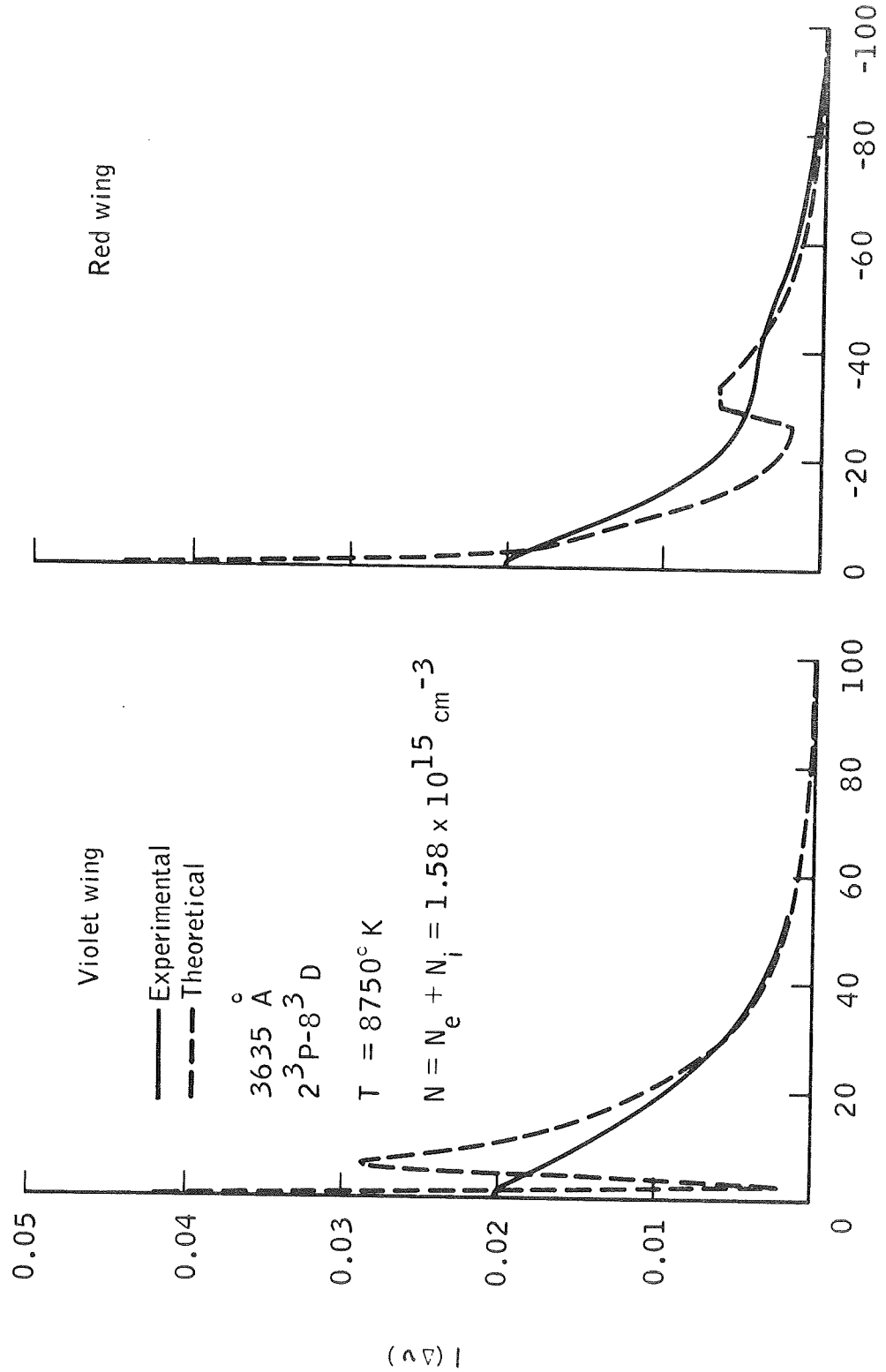

Figure 18.- Concluded.

were used. The root-mean-square value was chosen because the line intensity depends on the square of the electron density because $N_e = N_i$.

In the theoretical calculations, no variation in the perturber density with wave number was used, because such a correction is much smaller than the accuracy of the overall comparison. The higher lines have uncertain background, as was mentioned previously. In addition, the higher lines overlap, making the comparisons in the line wings less accurate. For the case $n = 4$, the theoretical profile was folded with the instrument profile. This was not necessary for the higher lines, because their half widths exceeded the instrument half width by at least a factor of ten. The profiles for the above lines, plus those for $n = 9$ and $n = 10$ are shown plotted together in figure 19. The profiles in figures 14 to 18 are normalized to the total intensity, as shown in the following equation.

$$\int_{-\infty}^{\infty} I(\Delta\nu)d\Delta\nu = 1 \tag{47}$$

Because the profiles do not extend to plus and minus infinity, a correction term was added to the integral. It was assumed that the line wings have a $\Delta\nu^{-5/2}$ dependence; therefore, that part of the wing omitted in an integration over a finite interval approximately equals $2/3\Delta\nu_f I(\Delta\nu_f)$, where $\Delta\nu_f$ is the finite integration limit. The profiles in figure 19 are normalized to the peak intensity.

Allowance for the background continuum and overlapping was made by subtracting an estimated background from the profiles prior to normalization. However, this was a rather crude approximation for the higher lines. For nonoverlapping lines, it would be possible to fit the far wings to a

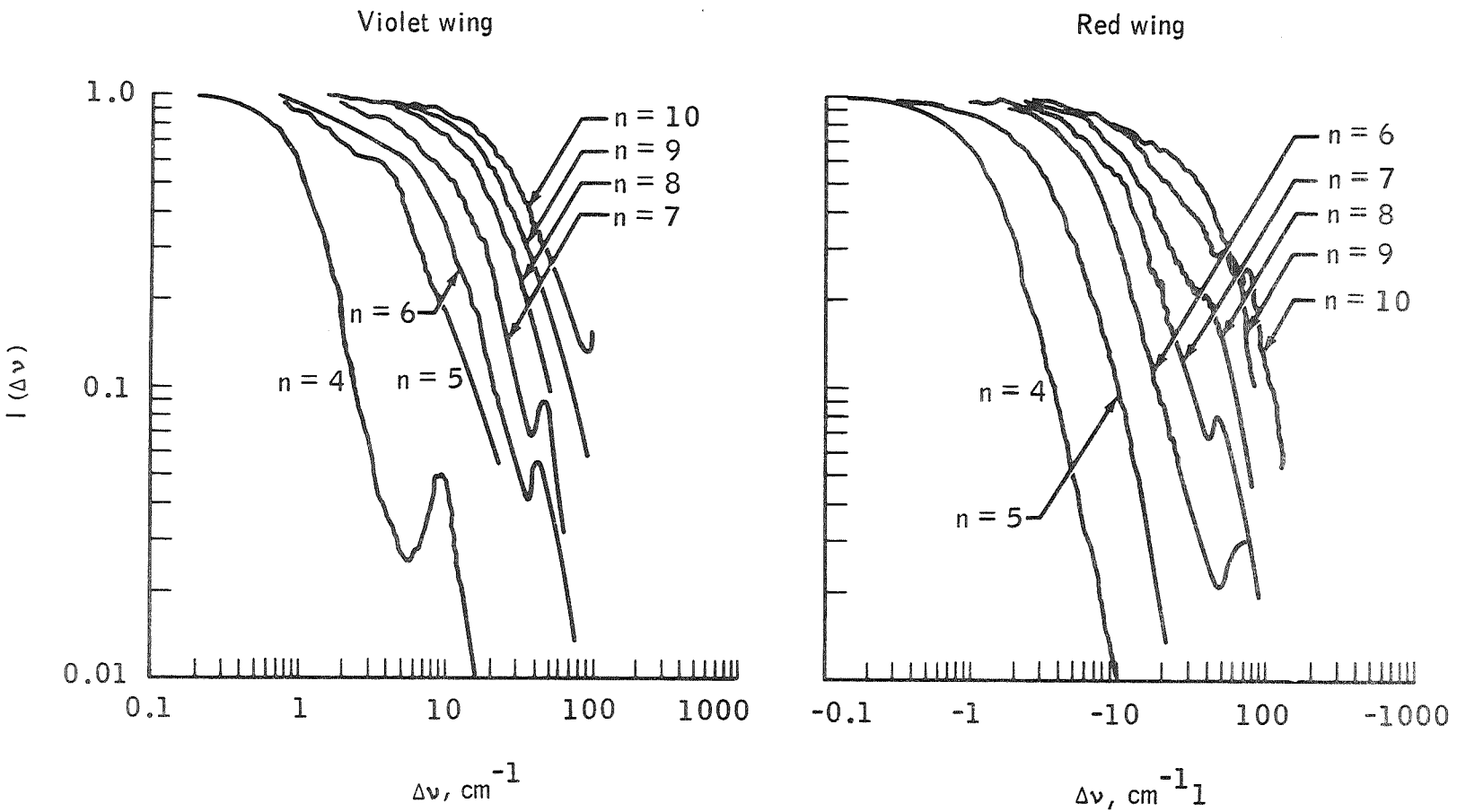

Figure 19.- Non-Abel-inverted experimental profiles for the $2^3P - n^3D$ series for $n = 4$ to $n = 10$, normalized to peak intensity.

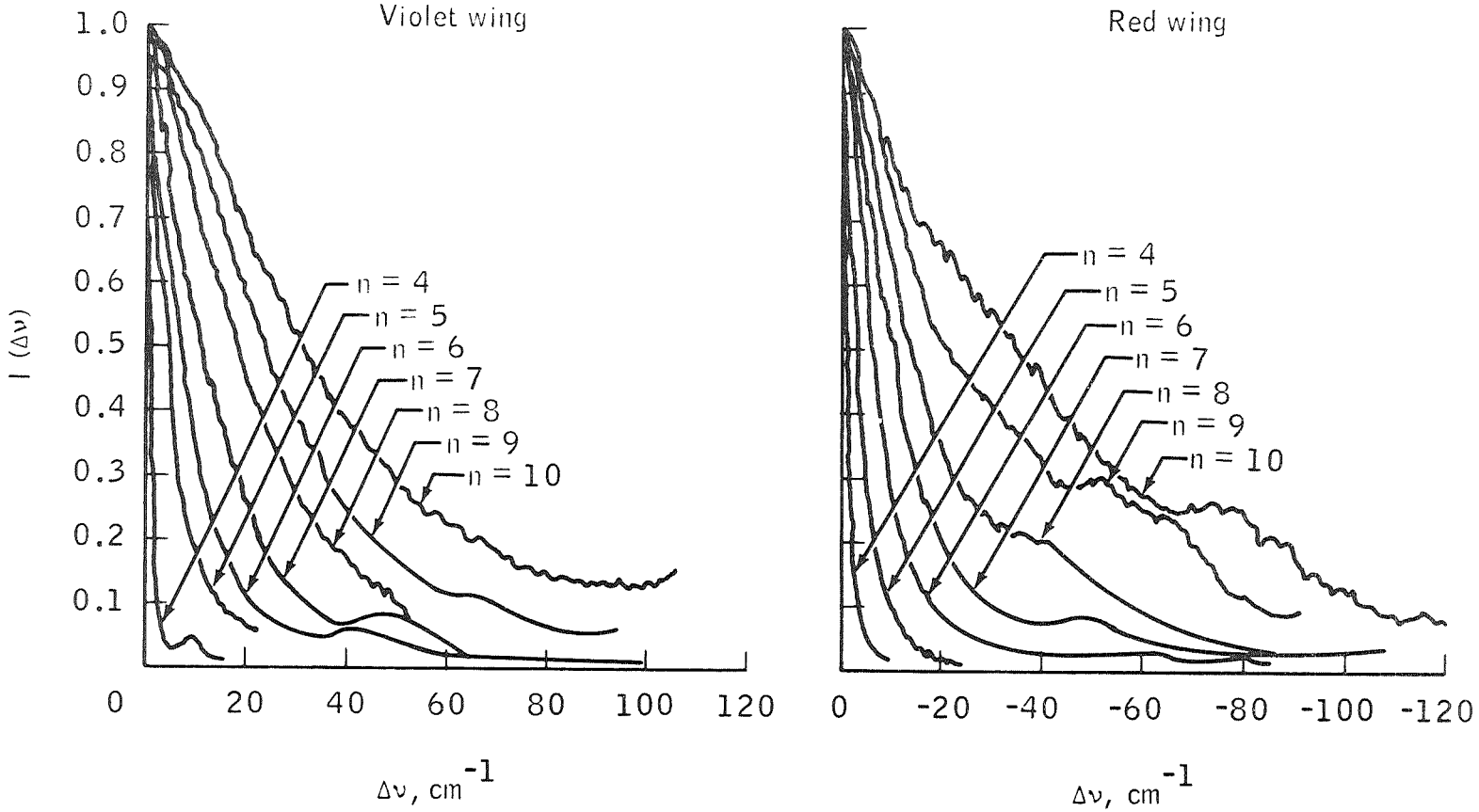

Figure 19.- Concluded.

-5/2 power-law curve and thus determine the amount of background, if one assumes the -5/2 power holds for the far wings. If one does not want to make this assumption, then the only course is to try to actually measure the background.

The theoretical profiles for the $n = 4$ and $n = 5$ lines exhibit strong peaks in their violet wings fairly near $\Delta\nu = 0$. In the case of $n = 4$ (fig. 14), the peak at $\Delta\nu = 7$ cm^{-1} is the $F_{0,1,2}$ Stark components ($\mu = 3$). Unlike the experimental profile, the group of $F_{0,1,2}$ components in the theory is well isolated. This indicates that another broadening mechanism is needed to establish agreement. In the case of $n = 5$ (fig. 15), the violet wing exhibits two isolated peaks: one at $\Delta\nu = 5$ cm^{-1} and another at $\Delta\nu = 11$ cm^{-1}, corresponding to the $F_{0,1,2}(\mu = 3)$ and $G_{0,1,2}(\mu = 4)$ Stark components, respectively. Again, there is a large deviation from the experimental profile, indicating the inadequacy of the quasistatic theory here. There is poor agreement in the violet wing because of overlapping with the 4009 Å line. There is fair agreement in most of the red wing for both $n = 4$ and $n = 5$. The $S(\mu = 0)$ and $P(\mu = 1)$ components are not present, because they are off the scale of the figures. The agreement of the quasistatic profile with the experimental profile for $n = 6$ (fig. 16) is rather poor for two reasons. The violet wing of the measured profile has some background interference from an unidentified source yielding a peak at approximately $\Delta\nu = 50$ cm^{-1}. The red wing agreement is disturbed by the presence of the forbidden P component.

For $n = 7$ and $n = 8$ (figs. 17 and 18, respectively), the agreement in both the red and violet far wings is reasonably good, considering that these profiles are averages. The profiles disagree near forbidden components and in the core.

4.4.2 Abel-Inverted Line Profiles

Abel-inverted line profiles were measured for three of the triplet diffuse lines of helium having $n = 6$, $n = 7$, and $n = 8$. These lines were chosen as a compromise. The higher lines had significant overlapping and were weak. The lower lines were so narrow as to require narrow exit slits to avoid significant instrument broadening, reducing the signal strength. In addition, the quasistatic theory does not apply to the low lines until extremely far out on the wings. The lines were scanned as described in Section 3.2.3, Abel-Inverted Line Profiles, and Abel-inversions were calculated at each $\Delta\nu$, beginning with $\Delta\nu = 0$ and progressing toward higher $|\Delta\nu|$.

The scan positions and intensities were then symmetrized (according to the scheme described in appendix B) by the use of a linear interpolation to obtain intensities at positive positions equal to the absolute value of the negative positions. The symmetrization reduced the error in the Abel-inversion caused by uncertainty in the center of the jet (ref. 25). Once the data were symmetrized, a least squares curve fit was performed on the symmetrical component. It was found that nine terms in the expansion gave the best overall fit. The functions had the form $(R^2 - y^2)^k$, where k took all integer values from zero to eight. A typical example of the measured data and the fitted curve are shown in figure 20. The corresponding radial-intensity distribution, numerically obtained from the curve-fit expansion coefficients and the analytic form of the inverted functions (which is $\lambda_k(R^2 - r^2)^{k-1/2}$, where λ_k is a constant resulting from Abel-inversion of $(R^2 - y^2)^k$ are shown in figure 21. Note that this function is singular at $r = R$ for $k = 0$; hence, the computed radial-intensity distribution is invalid in the neighborhood of $r = R$.

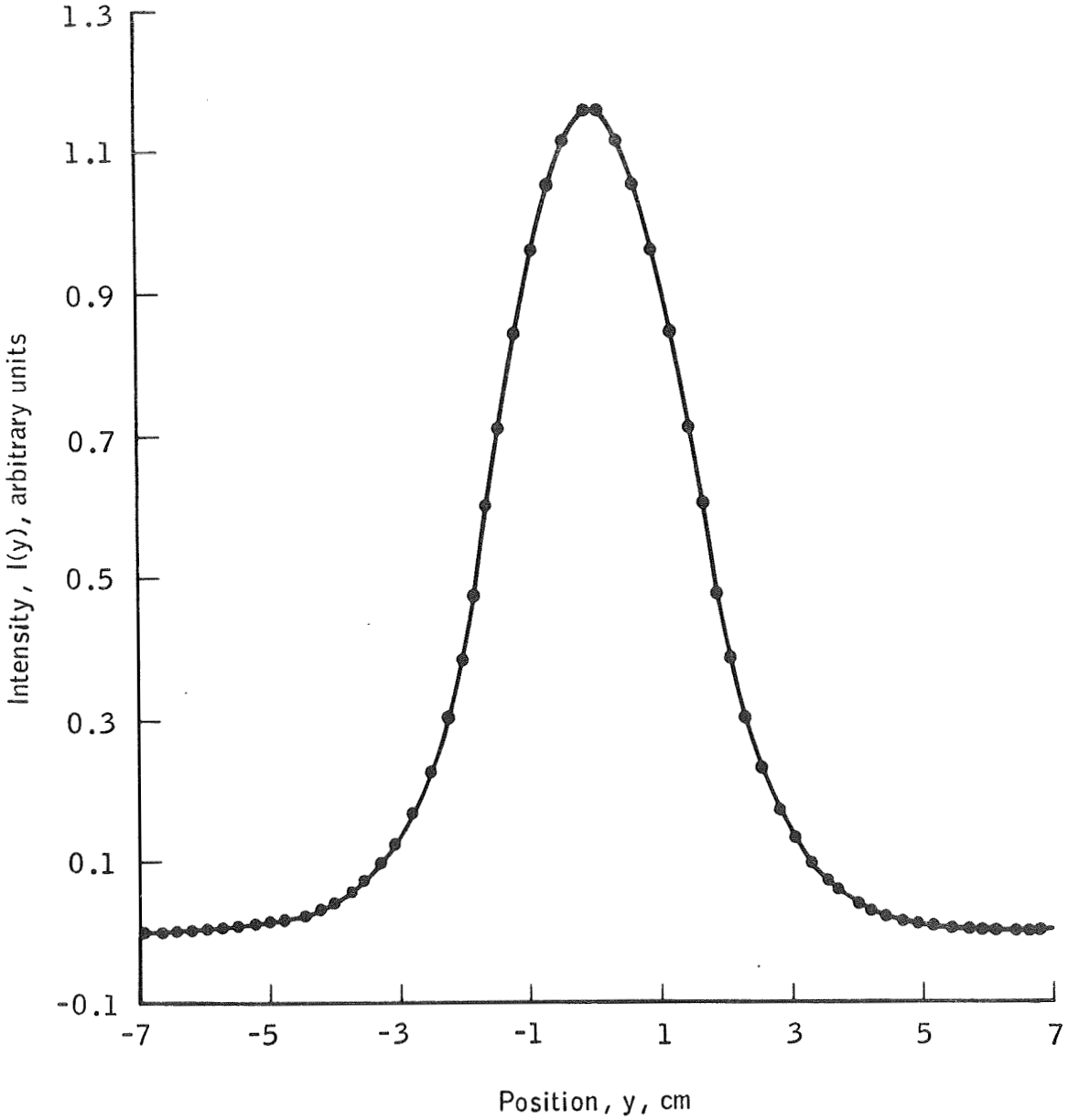

Figure 20.- Sample scan of jet for Abel-inversion which has been symmetrized (denoted by the plotting symbol); the continuous curve is the least-square fit.

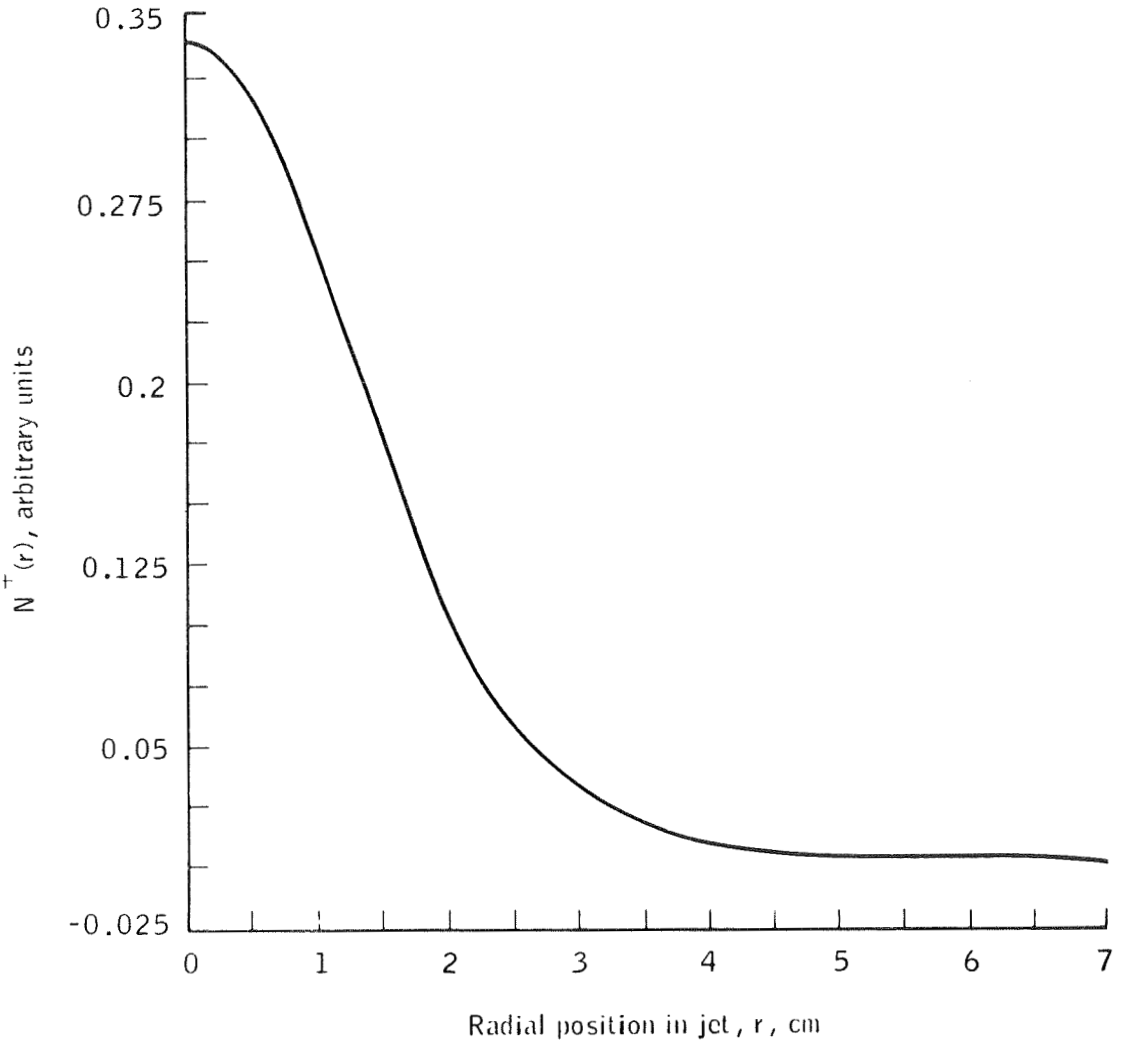

Figure 21.-Sample radial intensity distribution, which is the Abel-inversion of the data in figure 20.

After the radial intensity distributions $N(r)$ were calculated for each $\Delta\lambda$, the data were merged to obtain the line profiles at each radius $r = 0, 0.1R, 0.2R, \ldots, 0.8R$.

The profiles including the background continuum and so forth are plotted in figures 22 to 24. Note the wavelength shift in the peaks of the profiles with radius.

The background intensity was determined from other measurements and was assumed to be constant in the neighborhood of the lines. The center-line values were subtracted from the $r = 0$ Abel-inverted line profiles prior to plotting in figures 25 to 26. Along with these profiles, several quasi-static theoretical profiles are plotted. In these curves, the scale has been adjusted so that the maximum intensity is at $\Delta\nu = 0$.

The profiles for $n = 6$ are plotted in figure 25. The agreement is only fair here because of the presence of the $2^3P - 6^3P$ component in the red wing, and because of the uncertainty in background. The discrepancy in the line core where the quasistatic theory does not apply is quite apparent. However, even here the influence of the splitting of the 2^3D state by the Stark effect can be seen. Figure 26 is an expanded plot of the $n = 6$ line core and is presented merely to show the gross correspondence of the peaks in the quasistatic theory with the prominences in the experimental curve.

The theoretical curves in figures 25 and 26 were calculated for $T = 7800°$ K. Curve 1 involved a perturber density of $N = N_e = 1.37 \times 10^{15}$ cm^{-3}

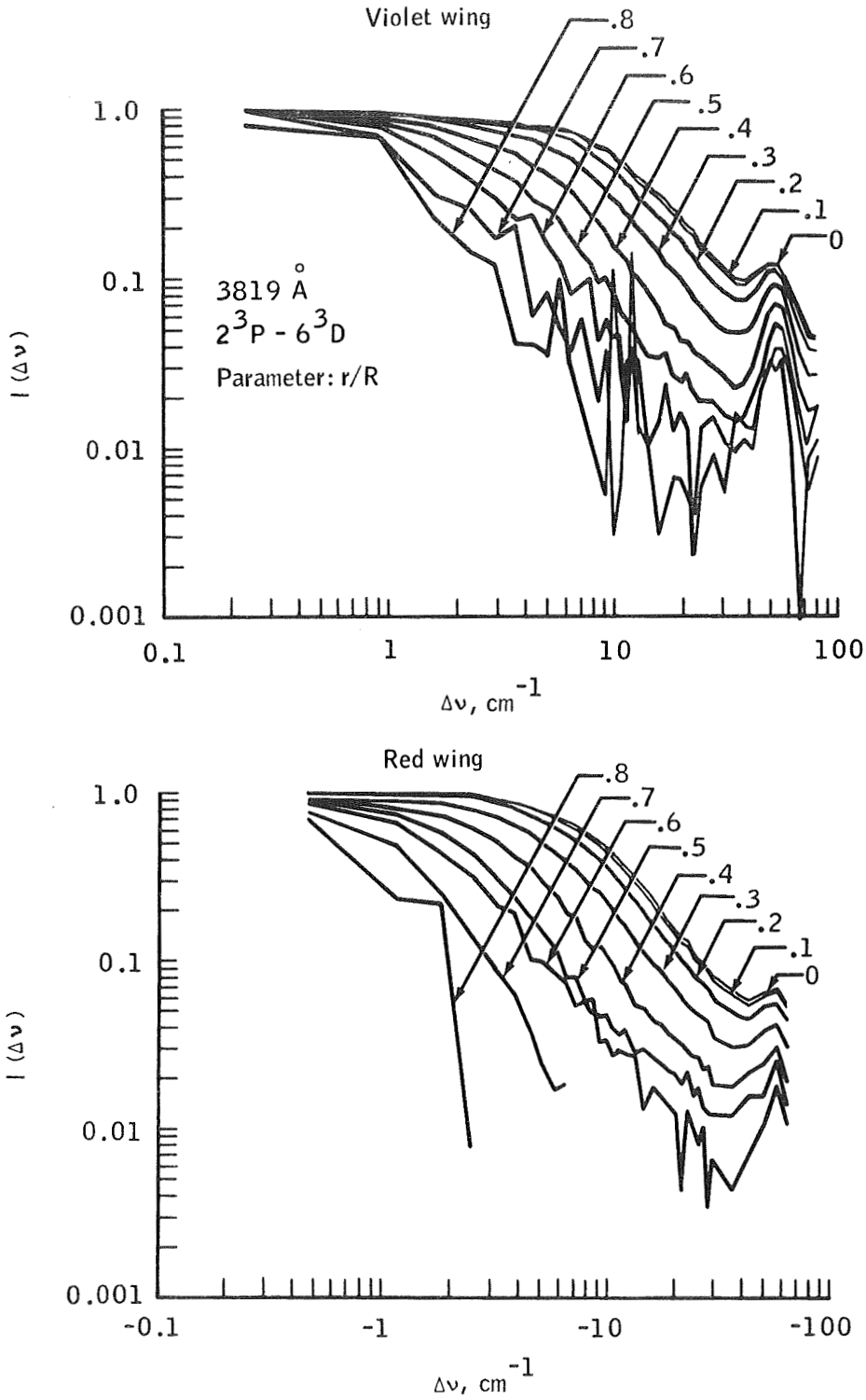

Figure 22.- Abel-inverted profiles of the $2^3P - 6^3D$ line, including background continuum, and so forth.

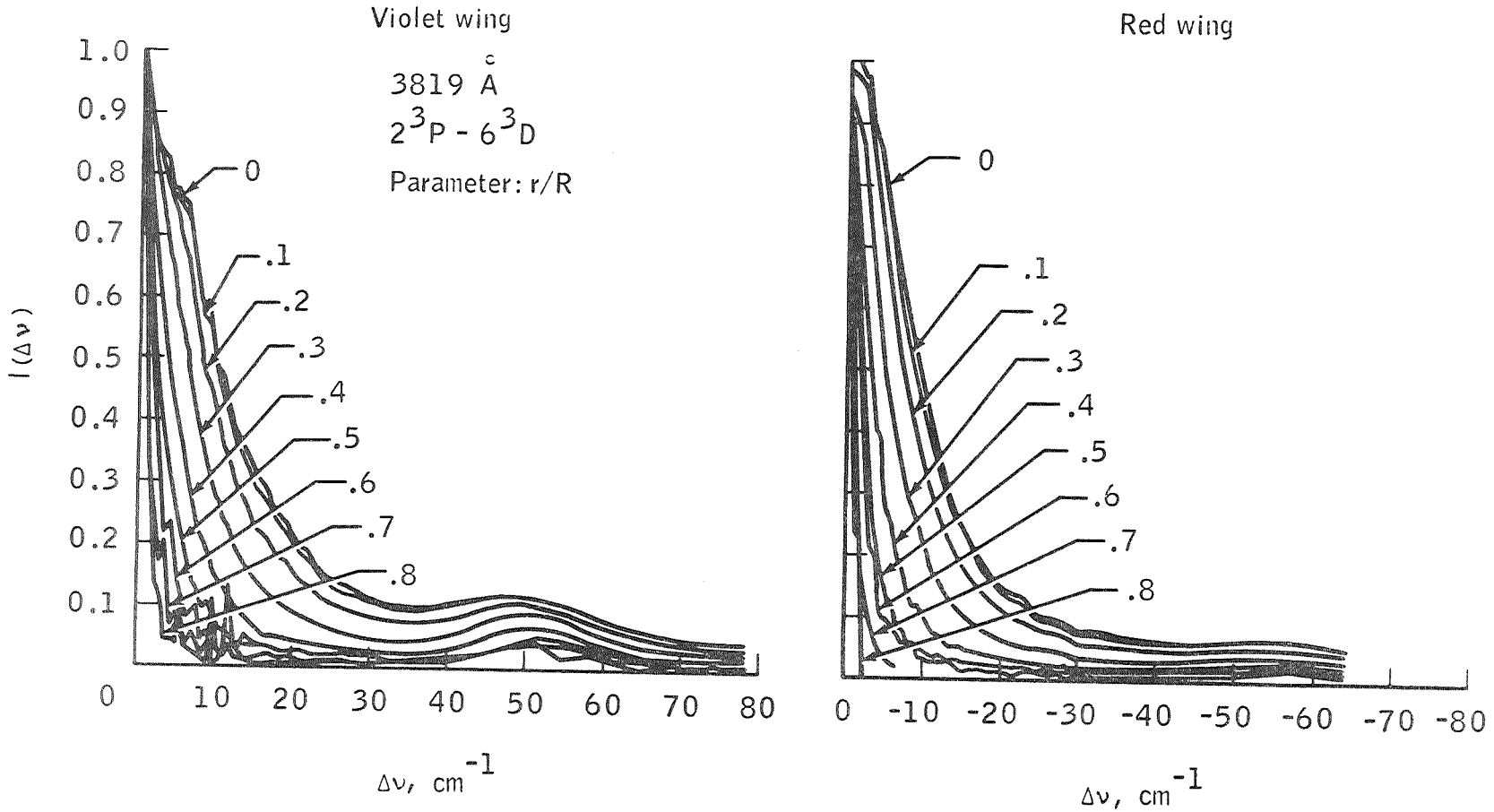

Figure 22.- Concluded.

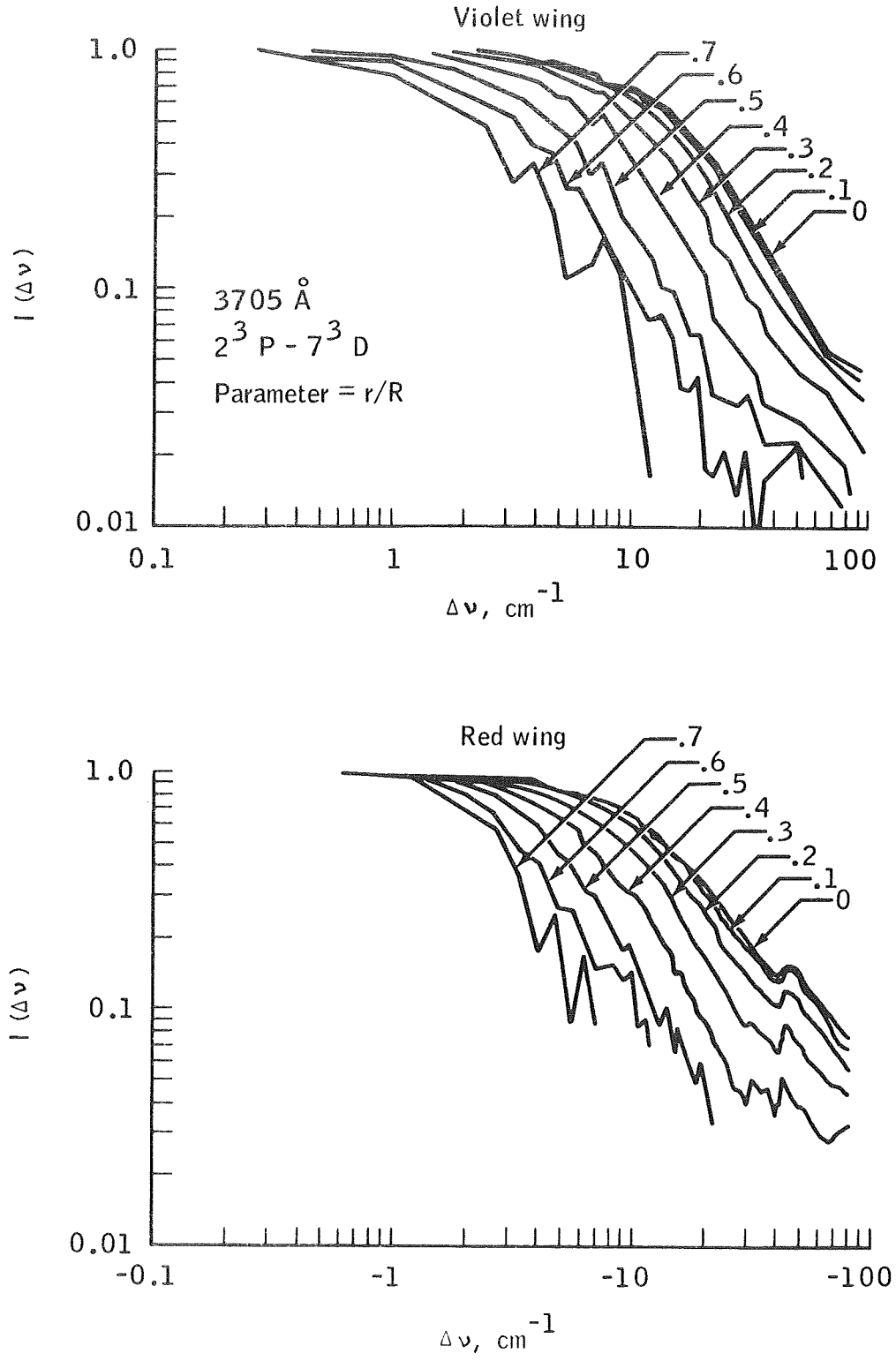

Figure 23.- Abel-inverted profiles of the $2^3P - 7^3D$ line, including background continuum, and so forth.

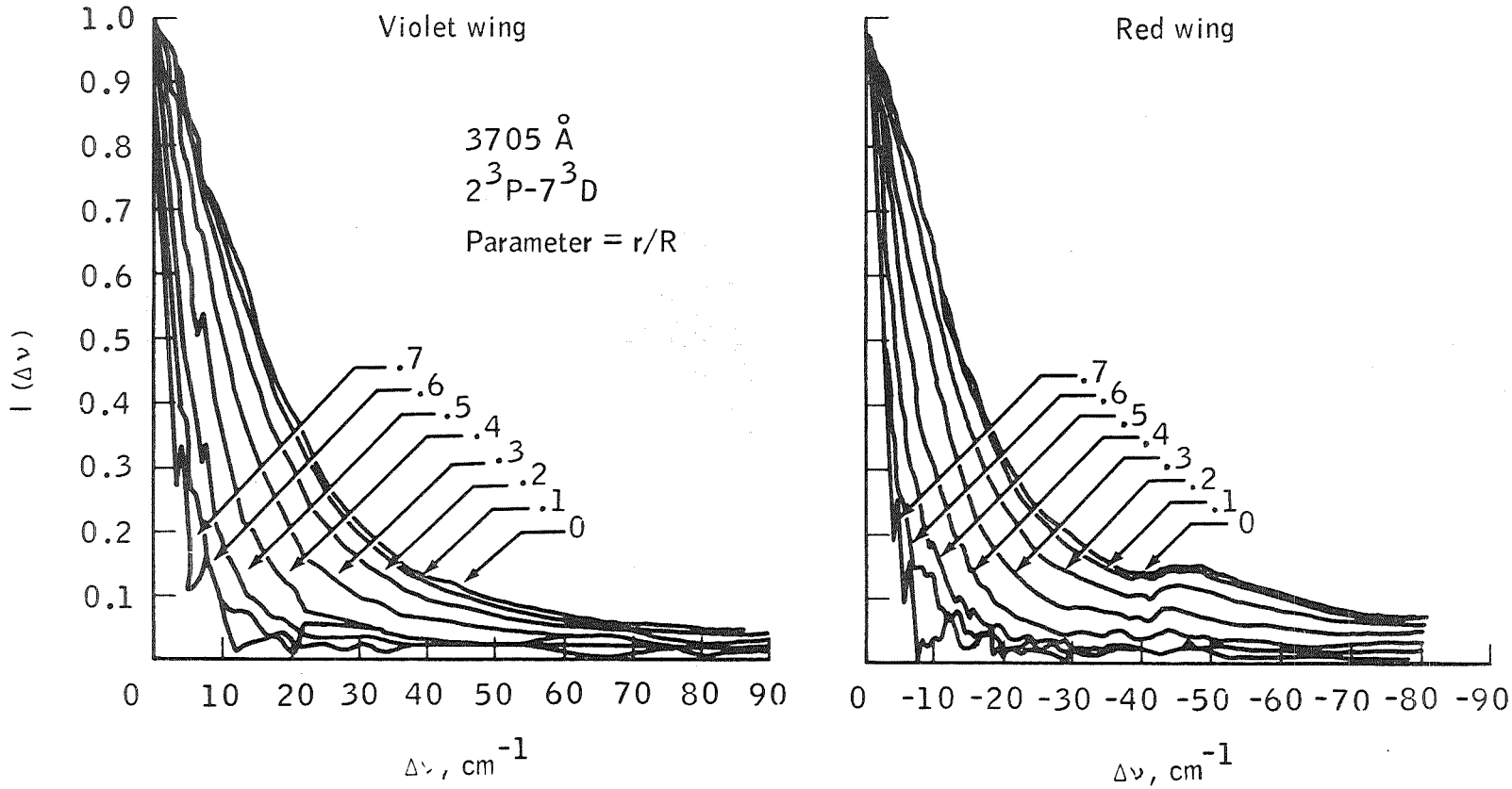

Figure 23.- Concluded.

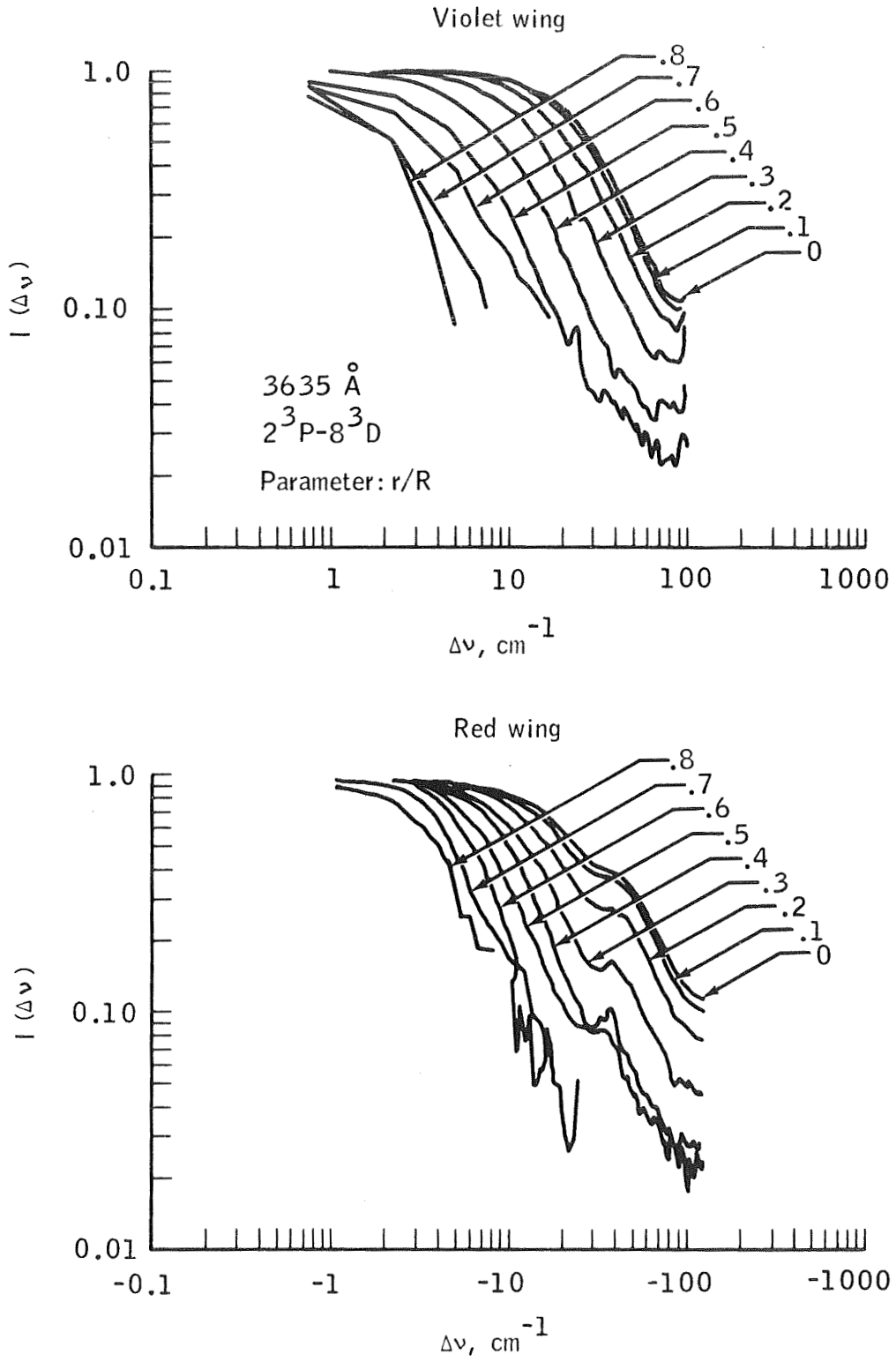

Figure 24.- Abel-inverted profiles of the $2^3P - 8^3D$ line, including background continuum, and so forth.

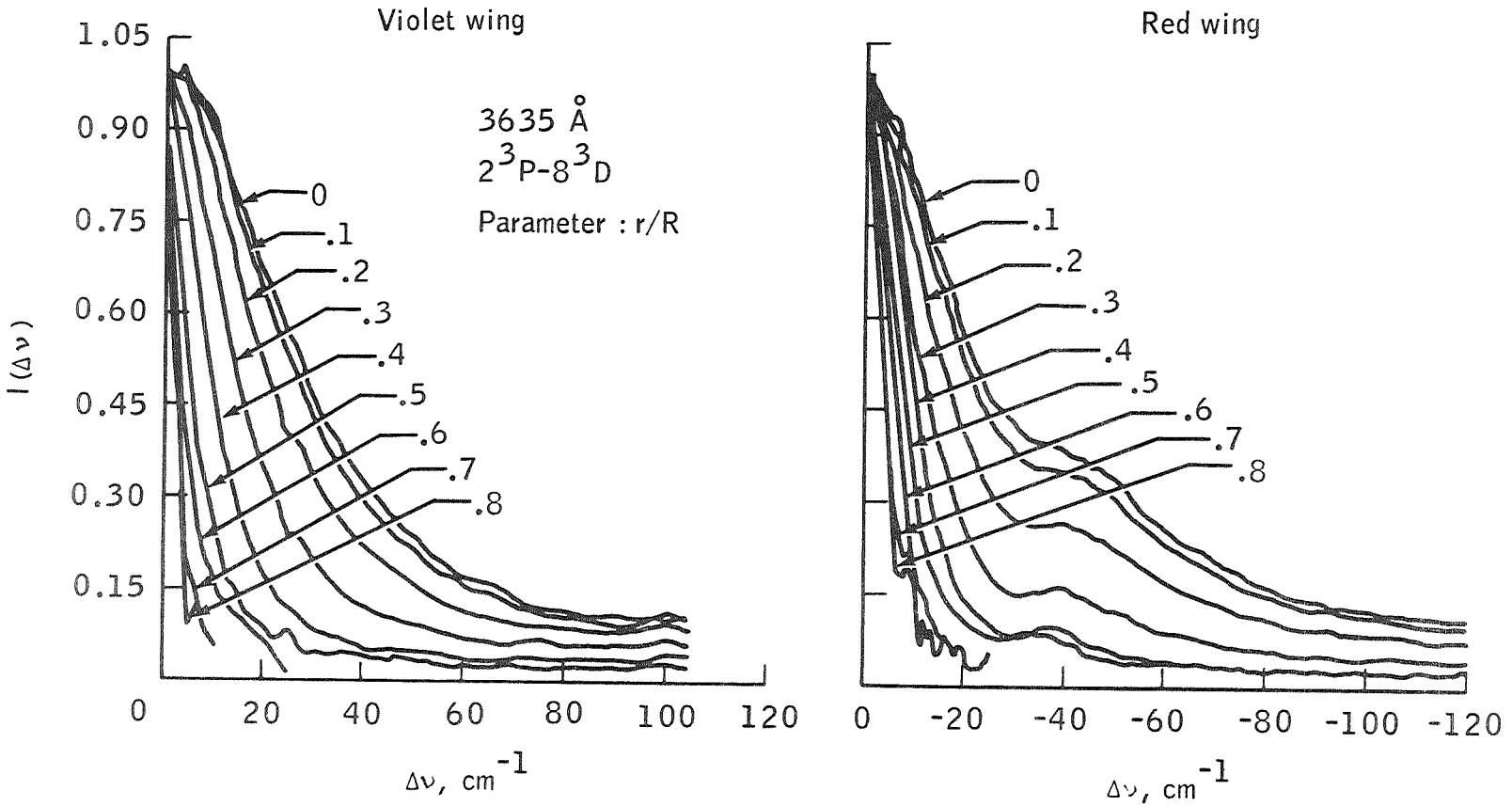

Figure 24.- Concluded.

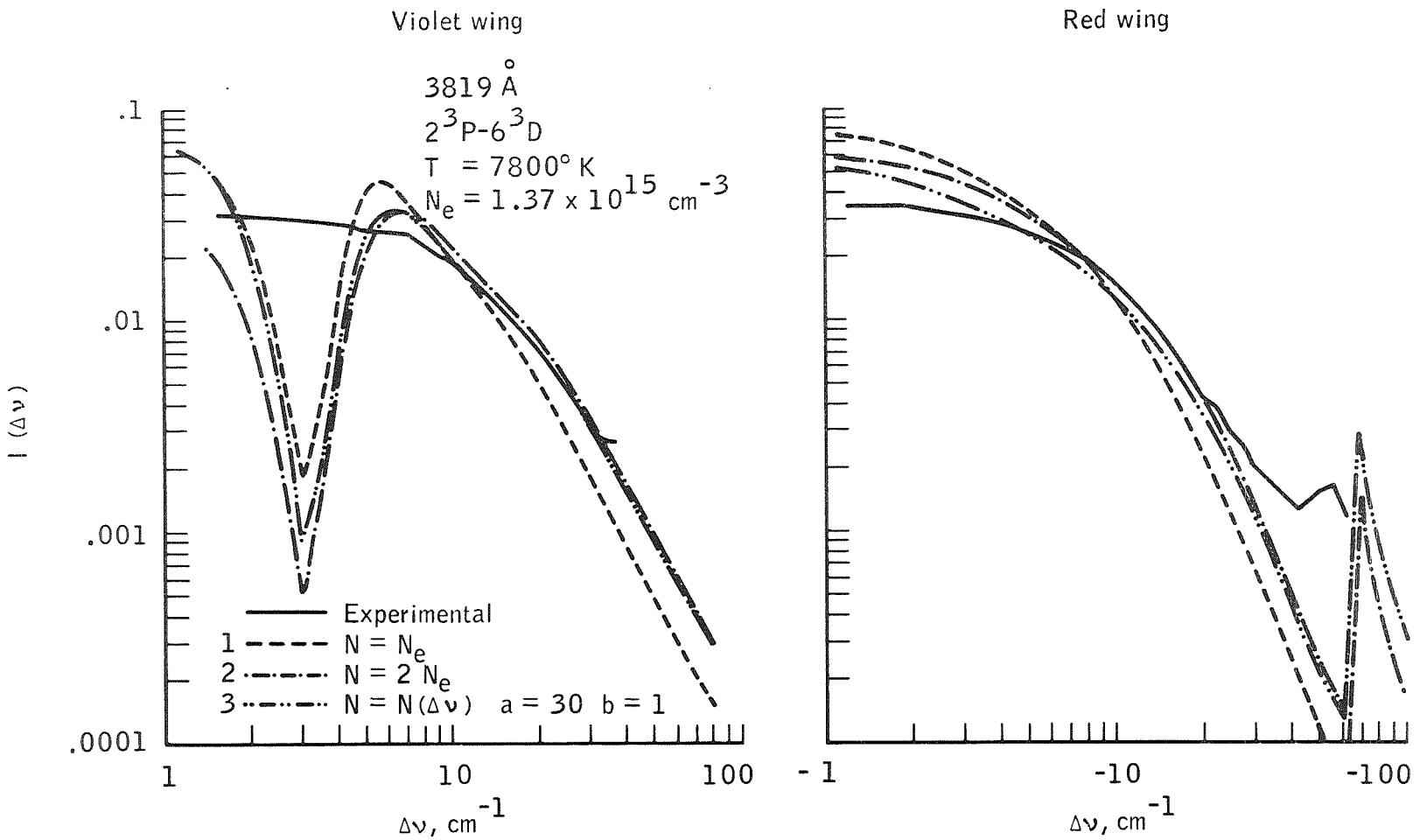

Figure 25.- Abel-inverted profile (r = 0) and quasistatic profiles folded with the Doppler profile for the 2^3P - 6^3D line.

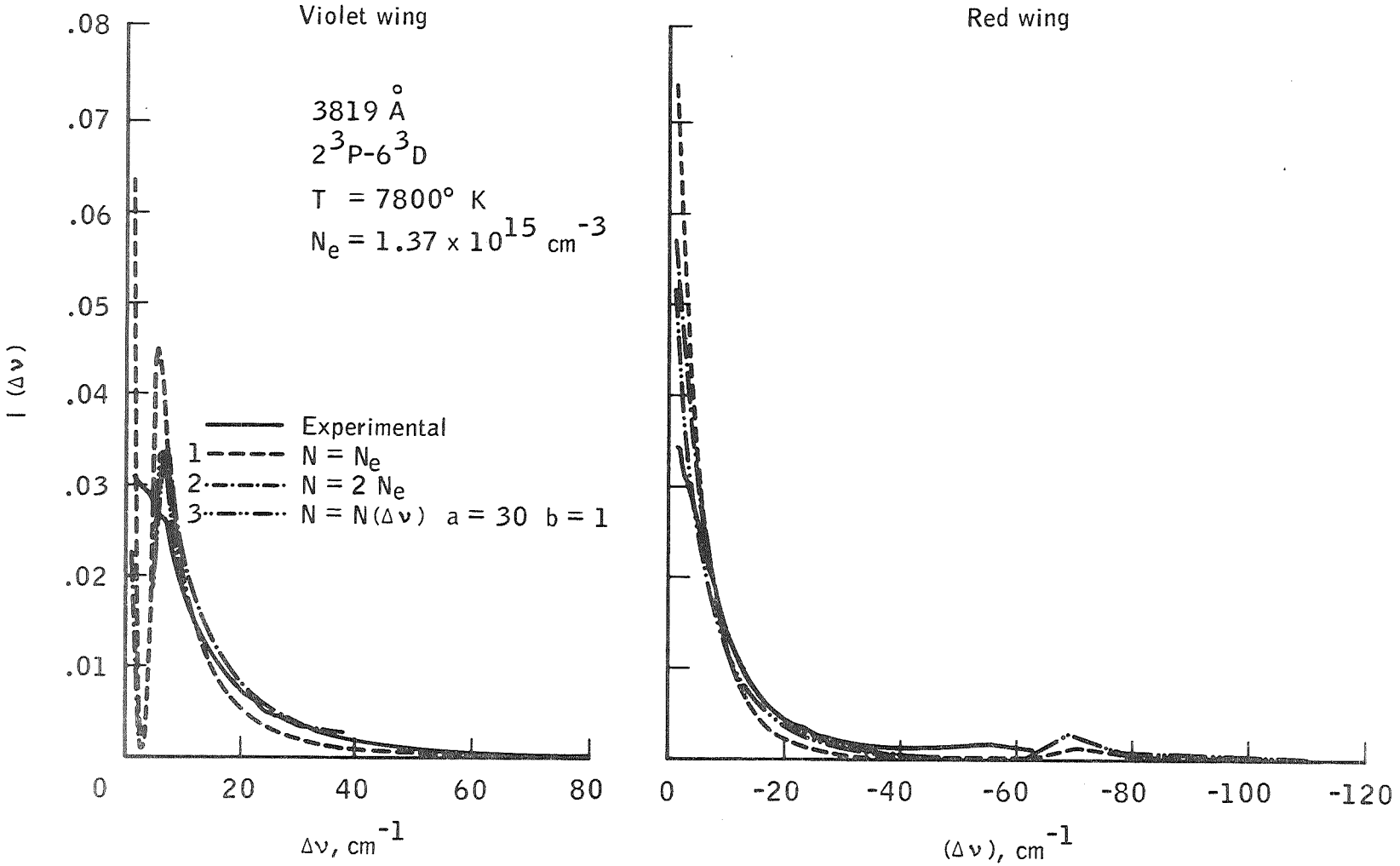

Figure 25.- Concluded.

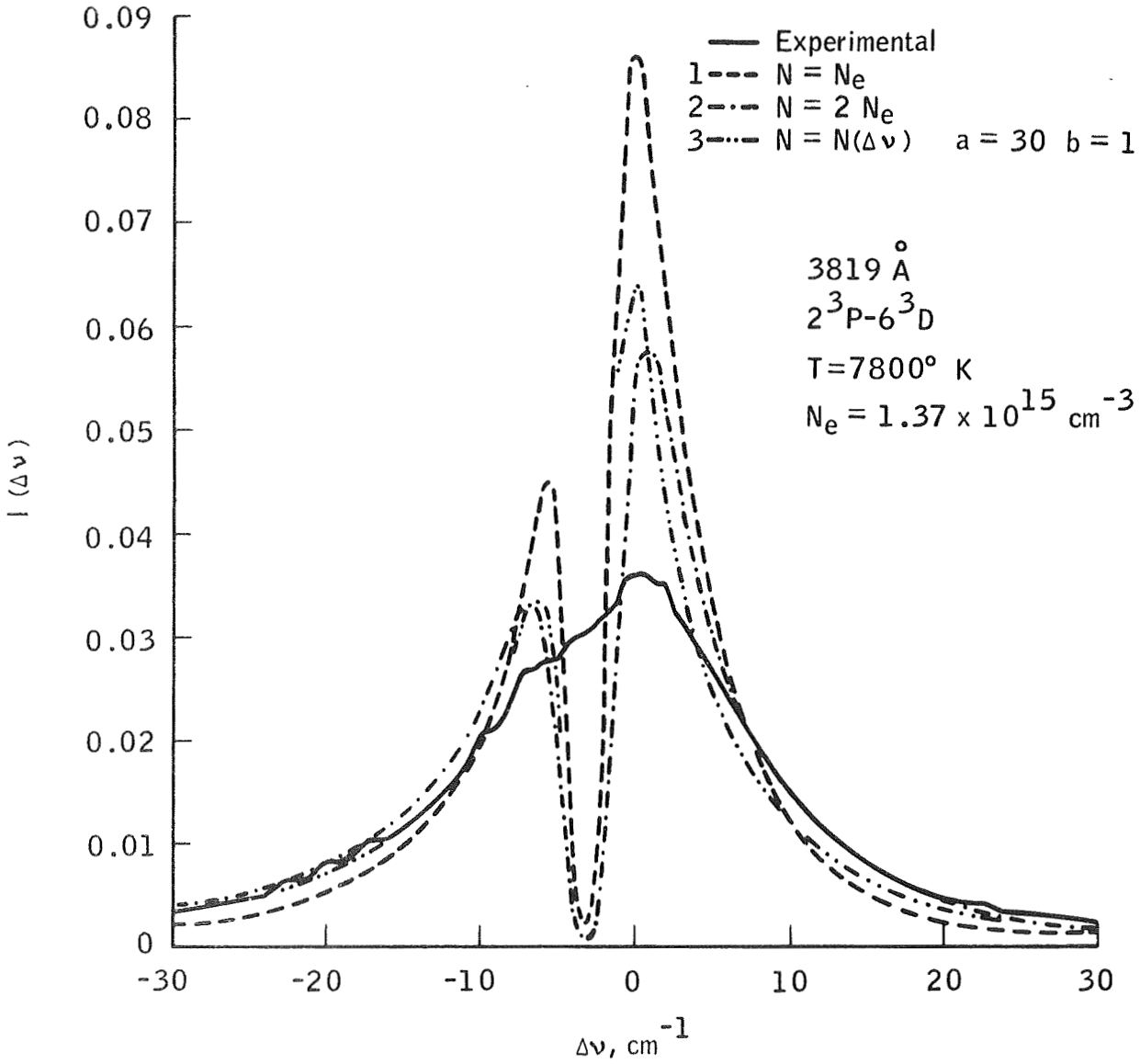

Figure 26.- Abel-inverted profile (r = 0) and quasistatic profiles folded with the Doppler profile for the $2^3P - 6^3D$ line in the line core.

with no dependence of N on $\Delta\nu$. Curve 2 involved $N = 2N_e$ with no dependence on $\Delta\nu$. Curve 3 involved $N = N_e$ with a dependence on $\Delta\nu$ of

$$Z = \left(\frac{30\Delta\nu}{\Delta\nu_L}\right)^{\frac{1}{I}} \tag{48}$$

that is, $a = 30$ and $b = 1$.

This choice of the parameters a and b improved the fit toward the center of the line in the violet wing, but no conclusions should be drawn here because of the uncertainties just mentioned.

The Abel-inverted profile of the $2^3P - 7^3D$ line is presented with three theoretical profiles in figure 27. The parameters used in the theoretical calculations were: curve 1, $a = 7$, $b = 1$; and curve 2, $a = 30$, $b = 1$ with $N = N_e$. Curve 3 has $N = 2N_e$ and no dependence of N on $\Delta\nu$ was used. The fit in the wings is rather poor, mainly because of uncertainty in the background, although measurement inaccuracy is manifest. No improvement in the fit is indicated by using a wavelength-dependent perturber density.

In figure 28 the Abel-inverted profile of the $2^3P - 8^3D$ line is shown. In this case, the fit in the violet wing is quite good until well into the core of the line. The red wing fit is not good because of the presence of the forbidden component. Curve 1 was calculated with $N = N_e$, $a = 10$, $b = 2$, curve 2 was calculated with $N = N_e$, $a = 10$, $b = 3$, and curve 3 with $N = N_e$, $a = 20$, $b = 2$. Curve 4 was calculated with $N = 2N_e$ and no dependence upon $\Delta\nu$. It can be seen that the best overall agreement of the experimental profile was obtained with curve 3. It is possible, by further adjusting the parameters a and b, that even better agreement could be obtained. Several other values were tried, but the agreement was not as good. Those values are listed in table V.

TABLE V.- EMPIRICAL PARAMETERS USED TO EXTEND RANGE OF AGREEMENT OF QUASISTATIC THEORY FOR THE $2^3P - 8^3D$ TRANSITION

$N_e = 1.37 \times 10^{15}$ cm^{-1}

$T = 7800°$ K

a	b
1	1
1	2
1	10
7	1
7	10
10	1
30	1
30	2
30	10
100	1
100	2
100	10
The following plotted in figure 28.	
7	2
10	2
10	3
20	2

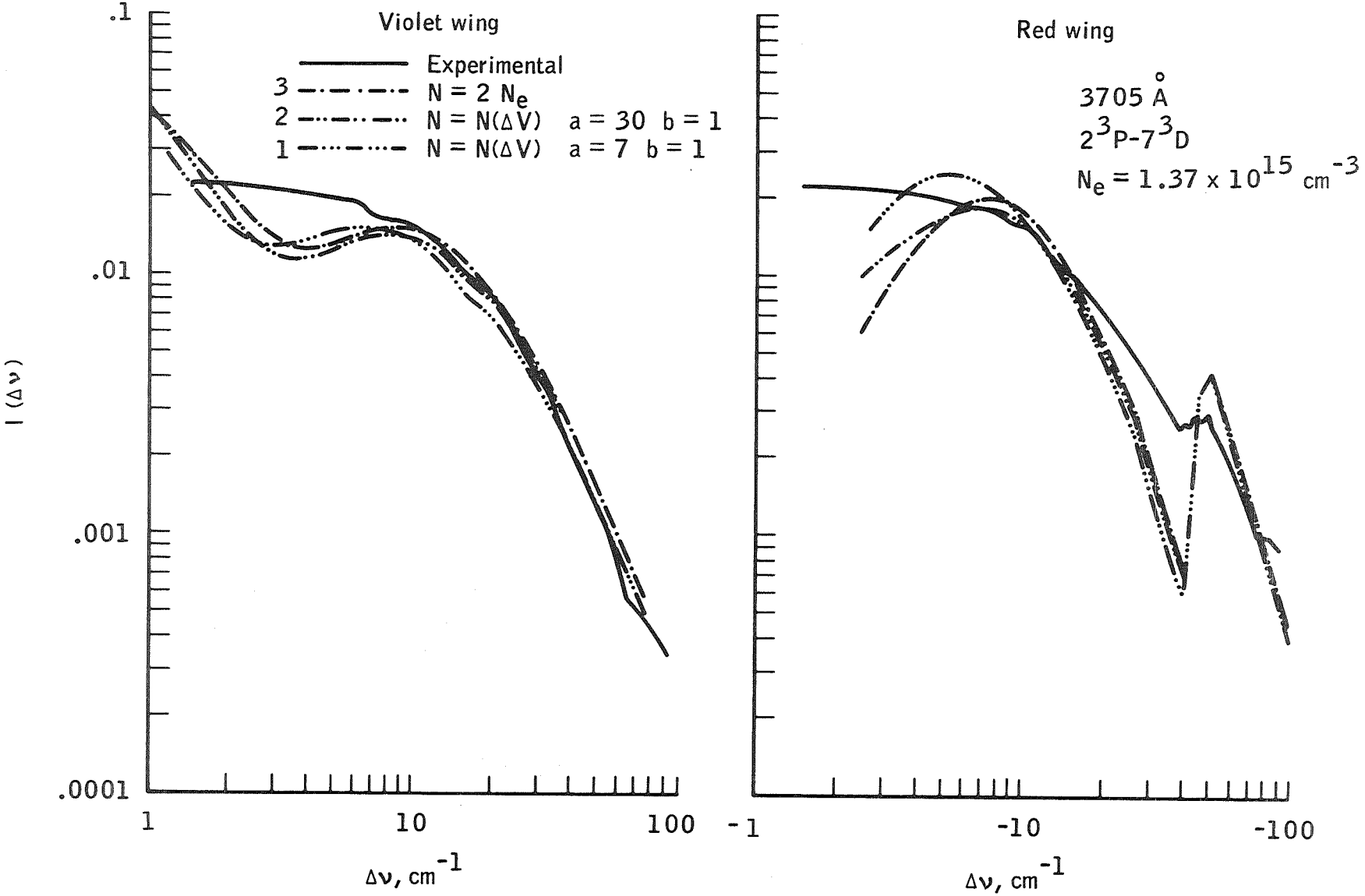

Figure 27.- Abel-inverted profile (r = 0) and quasistatic profiles folded with the Doppler profile for the $2^3P - 7^3D$ line.

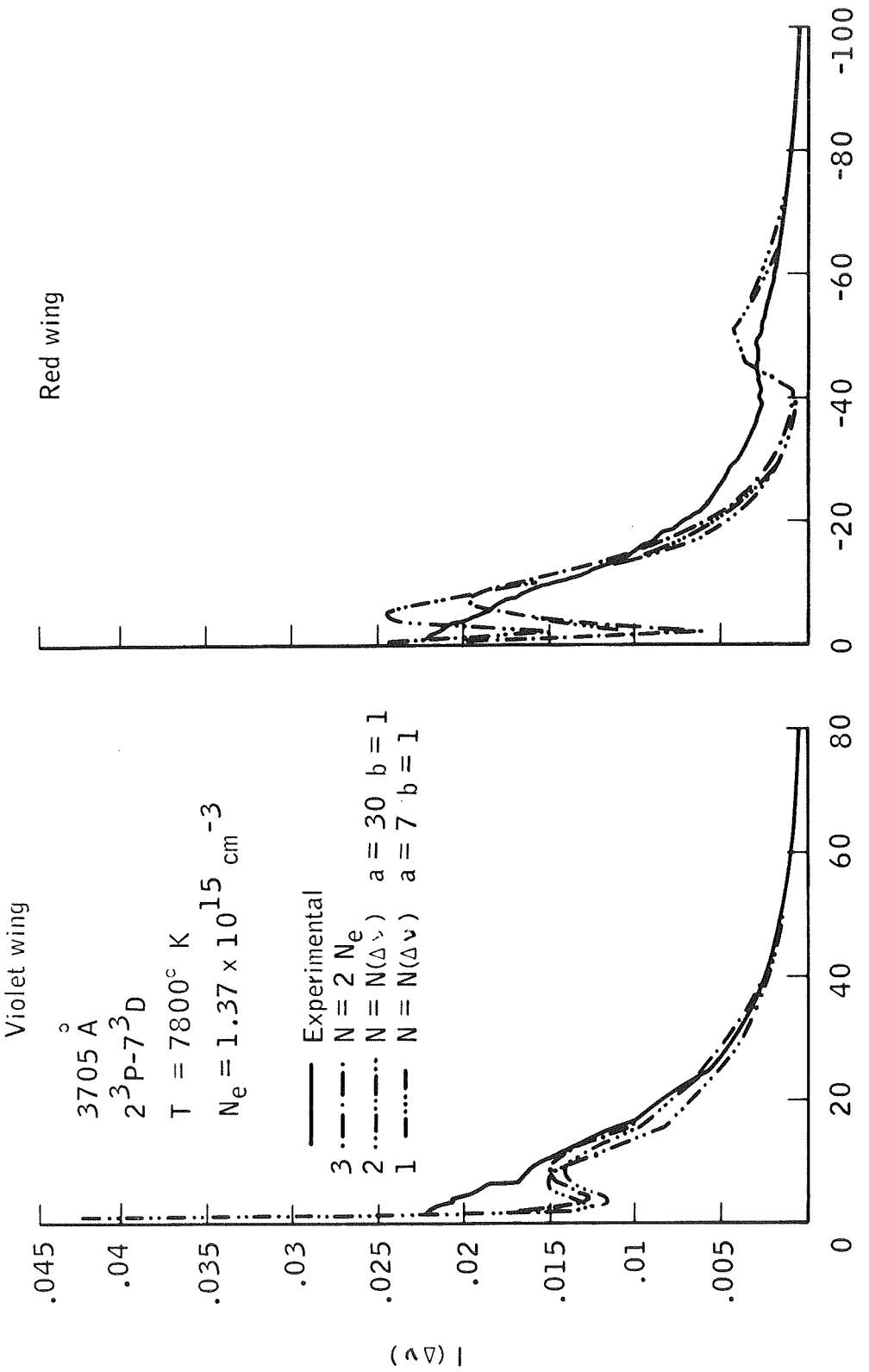

Figure 27.- Concluded.

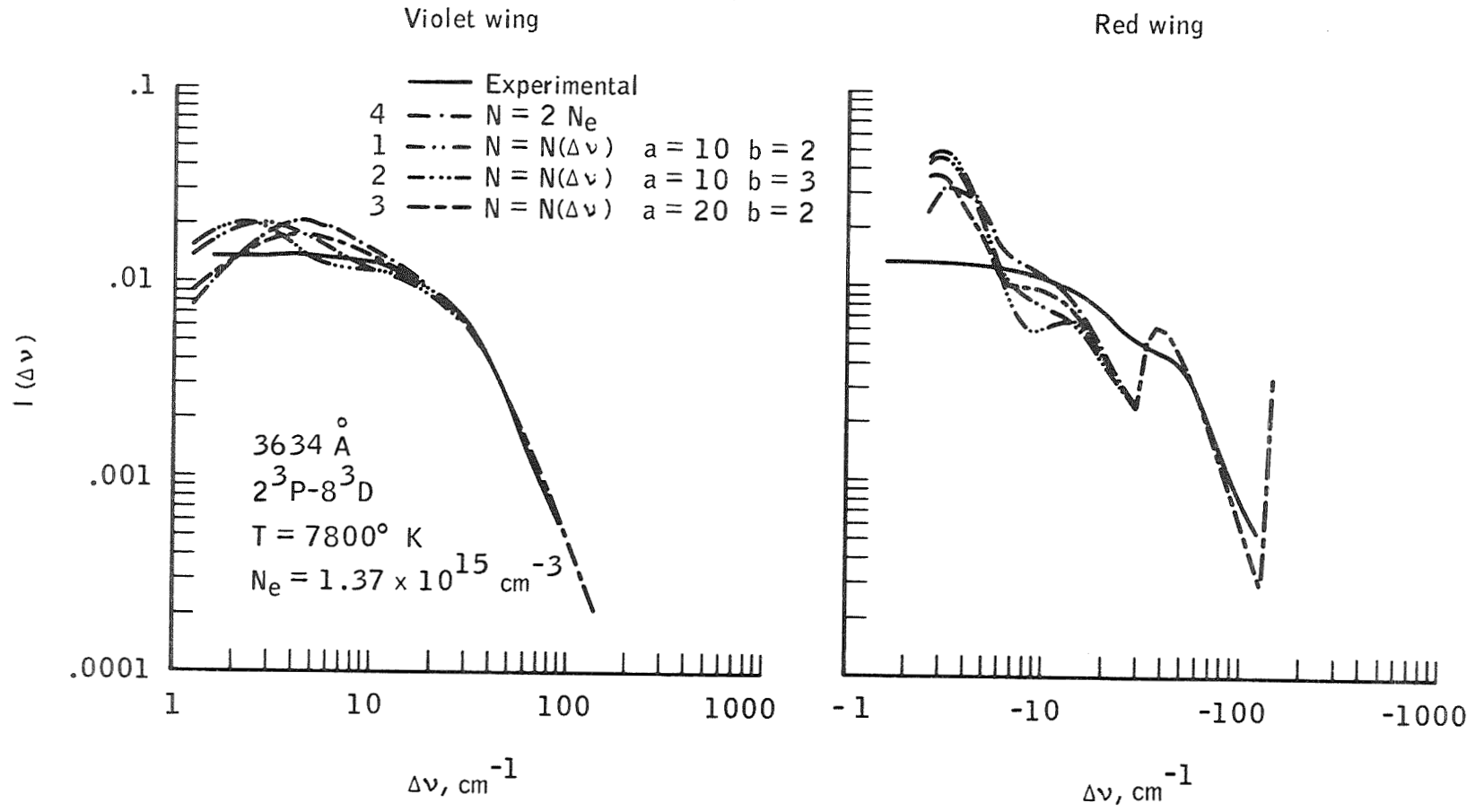

Figure 28.- Abel-inverted profile (r = 0) and quasistatic profiles folded with the Doppler profile for the $2^3P - 8^3D$.

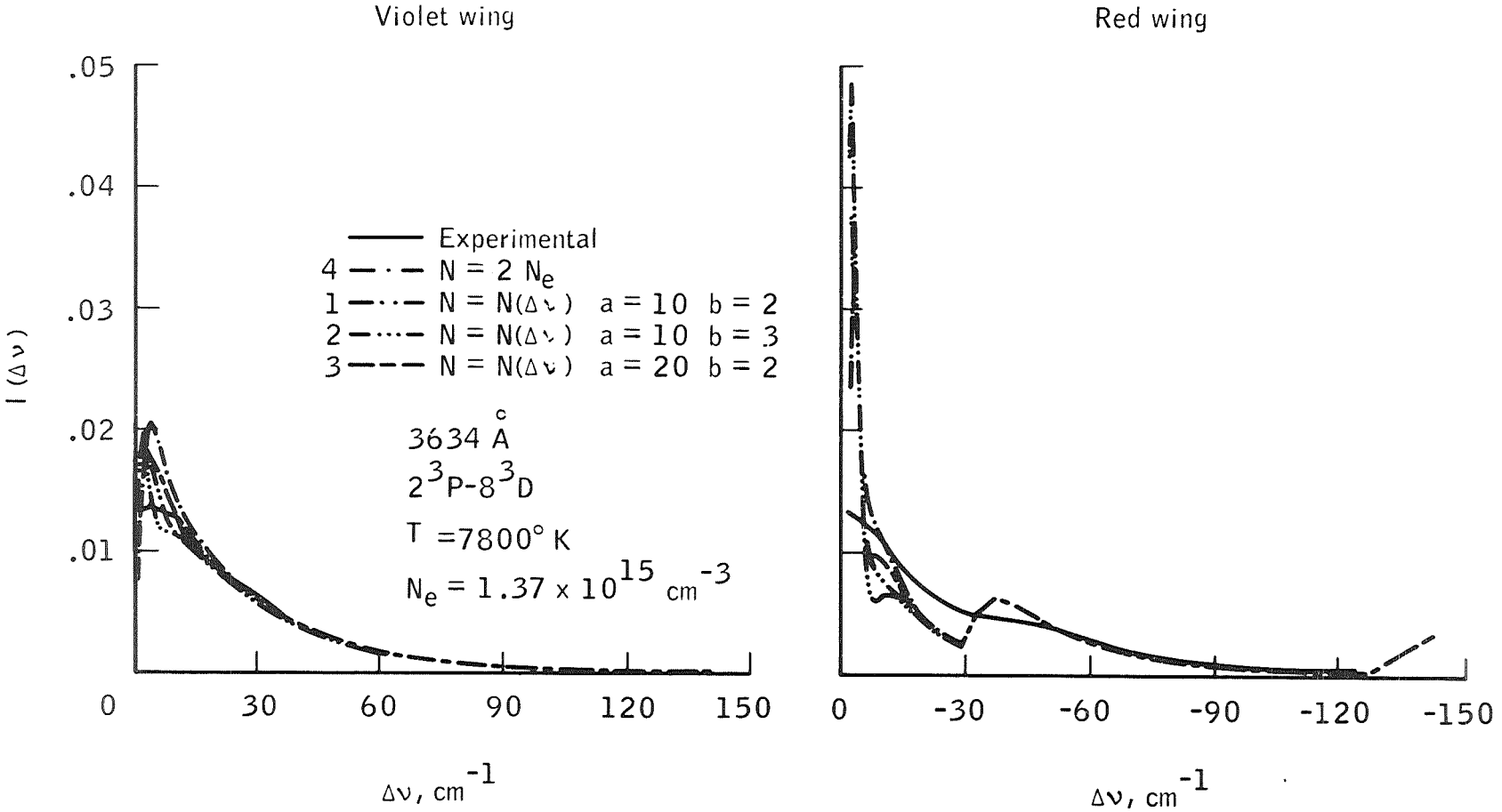

Figure 28.- Concluded.

In general, a fast transition from $N = 2N_e$ to $N = N_e$ provided the best agreement. That this was so is indicated by having to go to larger values of b. The parameter a shifts the point of transition, whereas b governs the rate at which the transition occurs.

The half widths of the averaged profiles and the Abel-inverted profiles are compared with $n(n - 1)$ in figure 29. The points for the averaged profiles fall close to a straight line, as would be predicted by use of the hydrogenic quasistatic theory. The points for $n = 4$ and $n = 5$ fall above the line, indicating deviation from the quasistatic approximation and the influence of other types of broadening. The point for $n = 10$ has a large uncertainty because of overlapping lines and background.

As was expected, the half widths corresponding to the Abel-inverted profiles $(r = 0)$ lie above the points for the profiles averaged along the line of sight. These points also show the same trend with quantum number, except the point for $n = 8$ should be about 20 percent lower to fall on a line whose slope is the same as that of the averaged profiles.

To determine whether one can use the half widths of the Abel-inverted profiles to measure the electron density profile of the jet, $W_{1/2}/N_e^{2/3}$ is compared with the radius in figure 30.

Note that the first few points of the $n = 6$ and $n = 7$ curves fall fairly well on a horizontal line; however, beyond that they begin to drop. This indicates that the latter two possibilities are more probable, because the reliability of the inversions decreases with increasing radius. The $n = 8$ curve begins to drop immediately and its relative position is too high, as indicated in figure 29. Thus, it is likely that in this case the half

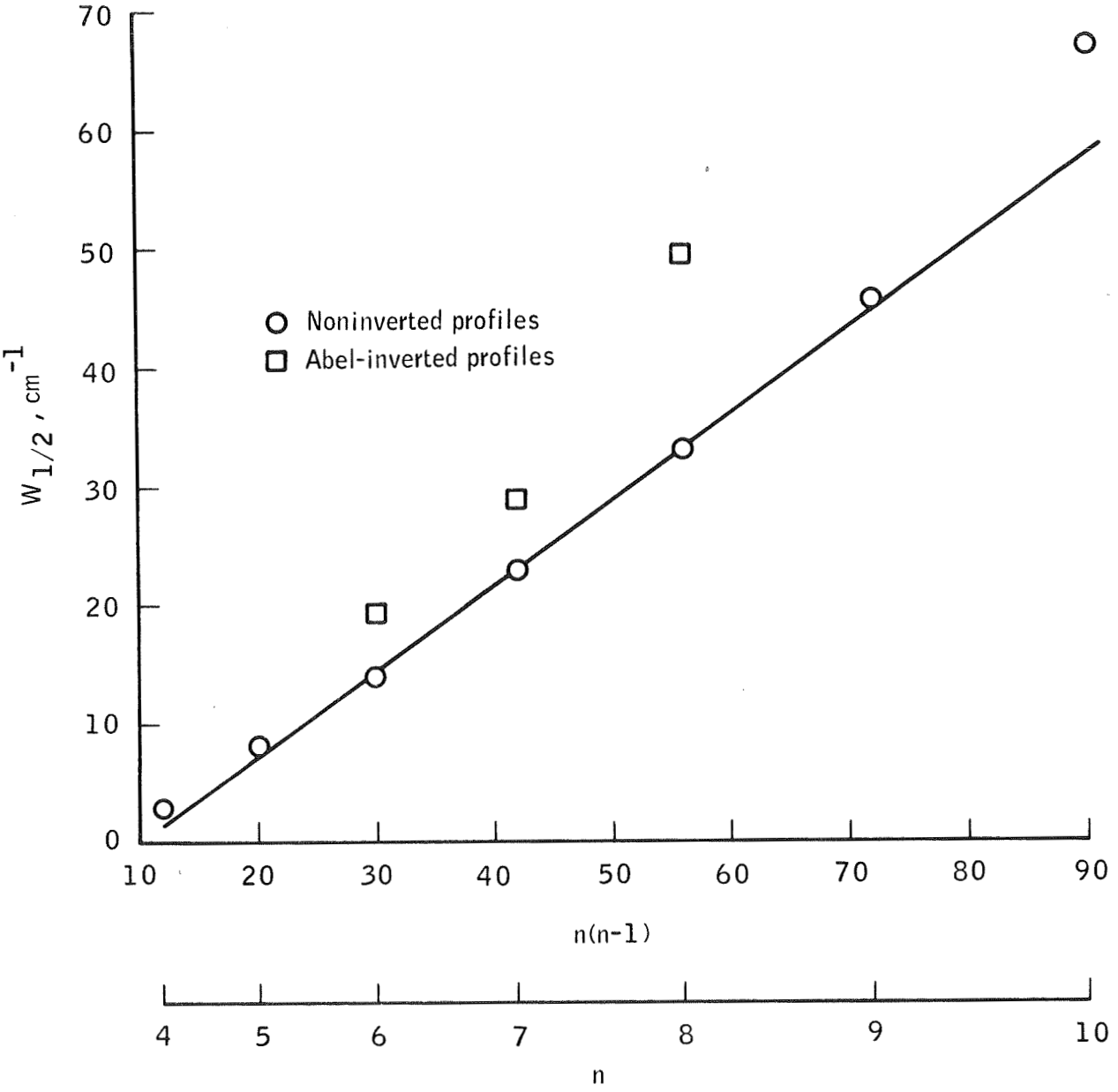

Figure 29.- Full widths of the measured Abel-inverted and non-Abel-inverted line profiles of the $2^3P - n^3D$ series. A best straight line is fit to the noninverted points. As expected the inverted data points lie above the noninverted points. The n = 8 point should fall about 20 percent lower in order for the Abel-inverted widths to have the same slope on the plot.

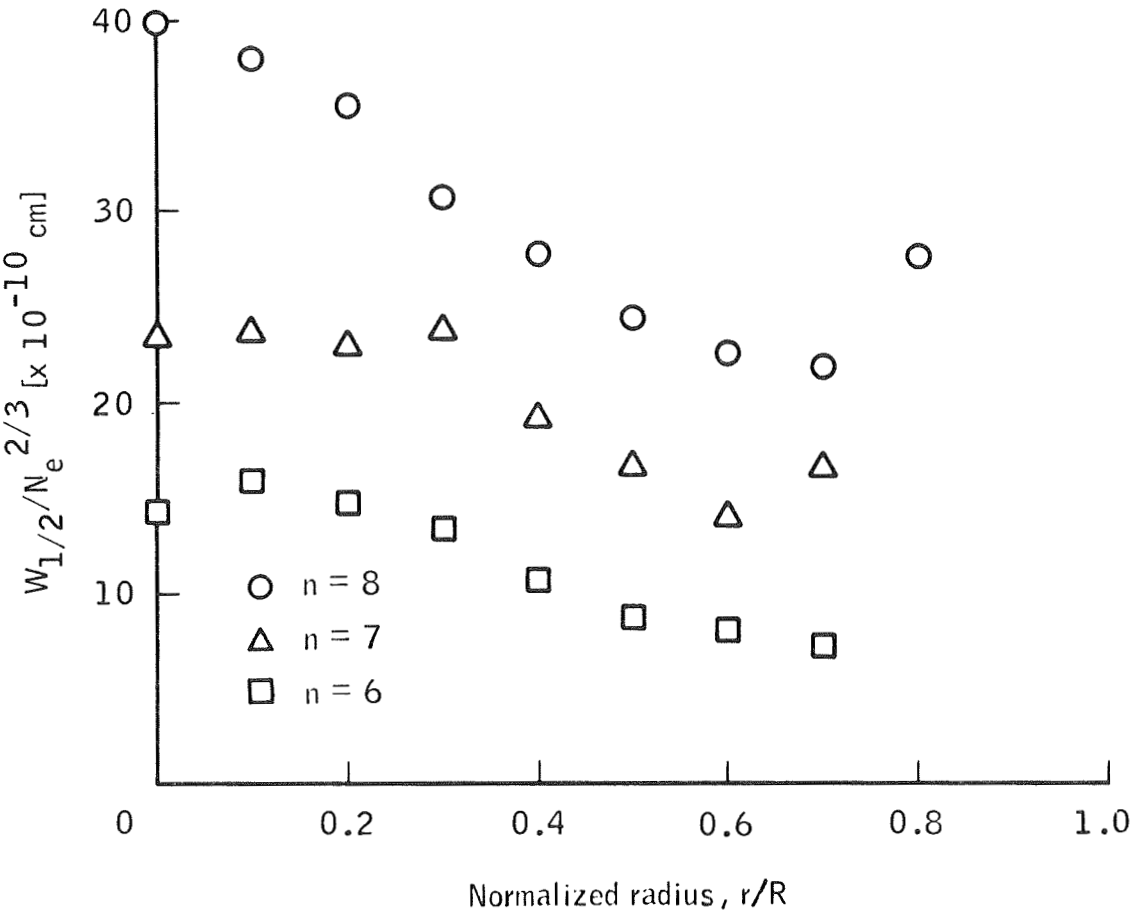

Figure 30.- Full widths of the Abel-inverted profiles divided by $N_e^{2/3}$ are plotted against the radius. The decrease with radius indicates increasing errors with r in the N_e or the widths or the failure of the $N^{2/3}$ dependence on width.

widths are in error as well, although it was in this case that the best agreement of the profile with the theoretical profile was obtained. Ideally, the curves should be straight horizontal lines. There are three possible causes for the exhibited behavior: (1) the half widths do not obey the $N_e^{2/3}$ dependence; (2) the density profile is in error, with either the center values too low or the outer values too high; or (3) the half widths obtained from the Abel-inverted profiles are in error. To determine the probable cause of this behavior, the Abel-inversion technique must be investigated. It is possible that a better choice of expansion functions would improve the accuracy of the inversions. Probably, the Abel-inversions yield values too large toward the edge of the jet, thus causing the density to be too large.

5.0 SUMMARY

Until now, there have been virtually no helium line-profile measurements in the electron density range from 10^{14} to 10^{15} cm^{-3}; all previous measurements have been made in low-density (10^{13} cm^{-3}) or high-density (10^{16} to 10^{17} cm^{-3}) plasmas. This has prevented comparison of the quasistatic and impact theories for helium Stark broadening in a range where the uncertainties in the theories are greatest. The measurements presented herein indicate a general agreement with the quasistatic theory for electrons and ions in the wings, except where forbidden components or overlapping with neighboring lines prevent a valid comparison. There was a general improvement in the agreement of the calculated profiles with the measured ones when the dependence of perturber density on wave number was included empirically in the calculations. This is consistent with the results of Schlüter (ref. 7), and an even better consistency with his results is found if Unsöld's estimate (ref. 26) for the critical value for the transition between the quasistatic and impact domains of electron broadening $\Delta\nu_L$ is used. His estimate is approximately one-half that of Traving (ref. 19); using it would effectively decrease the parameter a by a factor of one-half, yielding values closer to those of Schlüter in his hydrogen-profile calculations.

Because the only method used for determining the electron density was absolute continuum measurements, no assessment of any systematic errors could be obtained; and, because the electron density is the most important parameter in the profile calculations, future comparisons should have the benefit of a more certain electron density.

To improve the accuracy of the measurements, better accounting of the background is needed. If the assumption is made that the wings obey the $\Delta\nu^{-5/2}$ dependence, the fit in the wings could be forced by subtracting an amount of background which will yield the best $\Delta\nu^{-5/2}$ fit. Also, a more precise Abel-inversion measurement and numerical technique should be attempted. Choosing expansion functions which are a set of orthogonal functions satisfying suitable boundary conditions, as suggested by Birkeland and Oss (ref. 27), might improve the numerical fit in the Abel-inversion.

Because the standard error in N_e is ±13 percent at the jet center line and the line profile measurements have about ±5 to 10 percent uncertainty (possibly larger in the far wings), the comparisons have an accuracy of ±13 to 16 percent, at best.

To achieve the best overall agreement in the line core and in the wings, the impact theory would have to be accounted for in the theoretical profiles. However, this was not the objective of this work. This may be done in future investigations.

APPENDIX A

ABSOLUTE CALIBRATION OF THE SPECTROMETER

The response of a voltmeter which measures the current in the spectrometer photomultiplier is the folding of the instrument profile with the source profile. This can be represented mathematically by the equation

$$V = \int_0^\infty \sigma_\lambda P(\lambda - \lambda_o) I(\lambda)\, d\lambda \qquad (A1)$$

where V is the measured voltage, $I(\lambda)$ is the source intensity profile, σ_λ is a normalization constant, and $P(\lambda)$ is the normalized shape function of the instrument profile, $\int_0^\infty P(\lambda)\, d\lambda = 1$.

Suppose that the source is a calibrated source, such as a ribbon-filament lamp, whose intensity function is denoted by $I_{cal}(\lambda)$. If it is assumed that $I_{cal}(\lambda)$ is very nearly constant in an interval in which $P(\lambda)$ is not negligible $(\lambda_1 \leq \lambda \leq \lambda_2)$, then equation (A1) will reduce to

$$V_{cal} = I_{cal} \int_{\lambda_1}^{\lambda_2} \sigma_\lambda P(\lambda - \lambda_o)\, d\lambda \qquad (A2)$$

where $I_{cal} \approx I_{cal}(\lambda_o)$ and V_{cal} is the voltmeter response to the calibration source. Because of the normalization condition, equation (A2) will reduce to $V_{cal} = I_{cal}\, \sigma_\lambda$. If the sensitivity of the spectrometer S_λ is defined by the relation $V = S_\lambda I$, where V is the response of the voltmeter

to an intensity I, then it is readily seen that the normalization constant σ_λ equals the sensitivity S_λ. The absolute sensitivity is then

$$\sigma_\lambda = S_\lambda = \frac{V_{cal}}{I_{cal}} \tag{A3}$$

where I_{cal} is in absolute units.

Continuum Radiation

To measure the steradiancy of an unknown continuum source, the source is placed in the same location as the calibration source and the voltage V_c is measured

$$V_c = \frac{V_{cal} I_c}{I_{cal}} \tag{A4}$$

Then, intensity of the unknown continuum source in absolute units is

$$I_c = \frac{I_{cal} V_c}{V_{cal}} = \frac{V_c}{S_\lambda} \tag{A5}$$

Line Radiation

If the source is line radiation rather than continuum, the treatment is somewhat more involved. There are two cases. One case is where the width of the instrument profile is not wide compared with the line to be measured. In this case, one must scan over the line and integrate the resulting profile. The second case is where the instrument profile is wide compared with the line. If background is negligible, then only the peak (flat top) intensity must be measured.

Case I. Instrument profile not wide compared with the line profile.-

The output of the voltmeter can be represented by the equation

$$v(\lambda') = \int_0^\infty \sigma_\lambda P(\lambda - \lambda') J(\lambda)\, d\lambda \tag{A6}$$

where $J(\lambda)$ is the spectral steradiancy of the line in $\mu W/cm^2\text{-sr-}\mathring{A}$.

If

$$I_{line} = \int_0^\infty J(\lambda)\, d\lambda \tag{A7}$$

is the total steradiancy of the line in $\mu W/cm^2\text{-sr}$, then we can write $I_{line} L(\lambda) = J(\lambda)$ and $\int_0^\infty L(\lambda)\, d\lambda = 1$, where $L(\lambda)$ is the normalized line profile.

By scanning over wavelength then integrating the result, we have

$$V_{line} = \int v(\lambda')d\lambda' = \int_0^\infty \int_0^\infty \sigma_\lambda P(\lambda - \lambda') I_{line} L(\lambda) d\lambda d\lambda' \tag{A8}$$

V_{line} has units of $mV - \mathring{A}$, say.

Because $P(\lambda)$ and $L(\lambda)$ are independent, the order of integration can be interchanged.

$$\int_0^\infty v(\lambda')d\lambda' = I_{line} \int_0^\infty \sigma_\lambda P(\lambda - \lambda')d\lambda' \int_0^\infty L(\lambda)d\lambda \tag{A9}$$

Then, $V_{line} = I_{line} S_\lambda$.

Solving equation (A9) for I_{line} and substituting equation (A4) for S_λ,

$$I_{line} = \frac{I_{cal} V_{line}}{V_{cal}} \tag{A10}$$

in $\mu W/sr\text{-}cm^2$.

Case II. Instrument profile wide compared with the line profile.- Beginning with equation (A6), the assumption is being made that $P(\lambda)$ is slowly varying or is constant over the range where $J(\lambda)$ is nonvanishing. Then, it can be removed from the integral

$$v(\lambda') = P_{\lambda'}{}^{o}\sigma_{\lambda'} \int_0^\infty J(\lambda)\, d\lambda \tag{A11}$$

where $P_\lambda{}^o$ is the peak value of the normalized profile. By equation (A7), this becomes

$$v(\lambda_o) = P_\lambda{}^o \sigma_\lambda I_{line} \tag{A12}$$

Using equation (A6) and integrating (scan) over the profile,

$$\int v(\lambda')d\lambda' = \iint \sigma_\lambda P(\lambda - \lambda')J(\lambda)d\lambda d\lambda'$$

$$= I_{line} \int \sigma_\lambda P(\lambda - \lambda')\, d\lambda \tag{A13}$$

is obtained.

Dividing equation (A12) by equation (A13)

$$\frac{v(\lambda_o)}{\int v(\lambda')d\lambda'} = \frac{P_\lambda{}^o \sigma_\lambda}{\int \sigma_\lambda P(\lambda - \lambda')d\lambda} \tag{A14}$$

Using equation (A3) and solving for $P_\lambda{}^o \sigma_\lambda$

$$\sigma_\lambda P_\lambda{}^o = \frac{v(\lambda_o)}{\int v(\lambda')d\lambda'} \tag{A15}$$

is obtained.

Knowing $\lambda_o P_\lambda{}^o$ for any line, equation (A12) can be used to calibrate any narrow line by a single measurement at the peak intensity v_p. Therefore,

$$I_{line} = \frac{v_p}{S_\lambda} \frac{\int v(\lambda)d\lambda}{v(\lambda_o)} \tag{A16}$$

In the presence of background, the background voltage must be subtracted before integrating (if integration over λ is required). Otherwise, $v_b(\lambda_2 - \lambda_1)$ can be subtracted from the integrated value, where λ_1 and λ_2 are the lower and upper limits of the integration, and v_b is the background signal.

The units of $\int v(\lambda)d\lambda / v(\lambda_o)$ are wavelength. This quantity can be defined as the effective spectral slit width W. If the profile were an ideal rectangle, triangle, or trapezoid, then W would be the full half-width of the profile. When the exit slit is wide compared with the entrance slit, W is very nearly equal to the spectral exit-slit width.

APPENDIX B

ABEL-INVERSION

The Abel-inversion technique that was used in these experiments was adapted from that of Freeman and Katz (ref. 25). A review of the technique is given here.

Consider a cylindrically symmetric luminous plasma, viewed perpendicularly to the flow axis. The plasma is assumed to be optically thin. The observed intensity is the sum of intensities emitted from volume elements along the line of sight (fig. B-1).

These measurements are essentially averages or integrated intensities over the thickness of the plasma, which is assumed to have cylindrical symmetry. If the contribution to the intensity at a radius r is $N(r)$, the measured intensity can be represented by

$$I(y) = 2\int_{o}^{x} N(r)dx \tag{B1}$$

(fig. B-1). The integration is along the line of sight.

Changing the integration variable to r yields

$$I(y) = 2\int_{y}^{R} \frac{N(r)rdr}{\left(r^2 - y^2\right)^{1/2}} \tag{B2}$$

where $x = \left(r^2 - y^2\right)^{1/2}$.

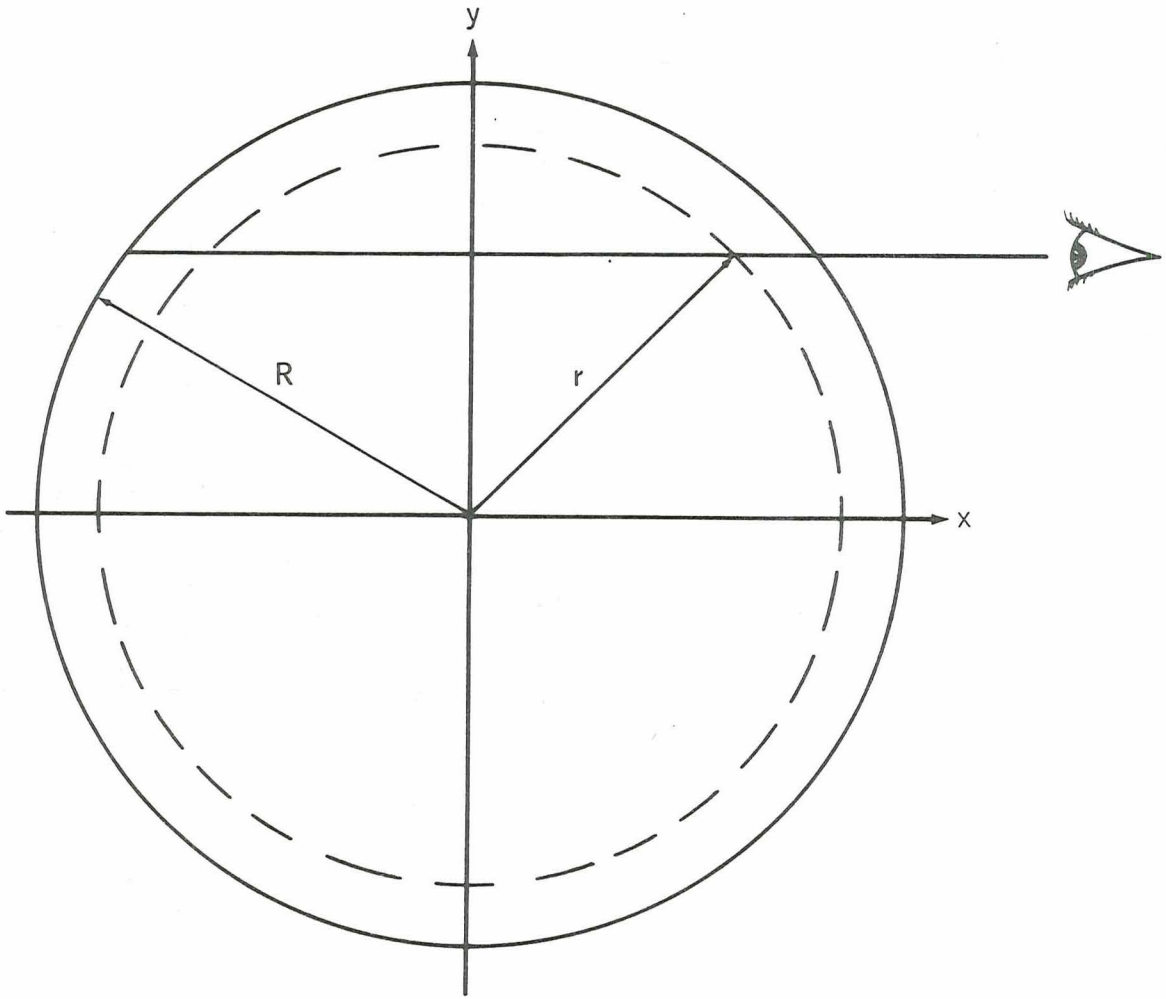

Figure B-1.- Cross section of the cylindrically symmetric jet; coordinate systems are indicated.

Equation (B2) is a form of Abel's integral equation, and it has the formal solution

$$N(r) = -\frac{1}{\pi}\frac{1}{r}\frac{d}{dr}\int_r^R \frac{yI(y)}{\left(y^2 - r^2\right)^{1/2}}\,dy \tag{B3}$$

If $I(R) = 0$, then equation (B3) can be written by integration by parts as

$$N(r) = -\frac{1}{\pi}\int_r^R \frac{dI(y)}{dy}\left(y^2 - r^2\right)^{-1/2}\,dy \tag{B4}$$

Unfortunately, the analytical form of $I(y)$ is not known, so equation (B4) cannot be integrated directly. A numerical technique must be used. One method is to expand $N(r)$ or $I(y)$ in a set of functional relations, then carry out the integration of this expansion analytically. Thus, if $N(r)$ is approximated by a linear combination of a set of functions

$$N(r) = \sum a_k \xi_k(r) \tag{B5}$$

then $I(y) = \sum a_k \eta_k(y)$ where $\xi_k(r)$ and the Abel transforms of $\eta_k(y)$.

The expansion coefficients a_k are determined by fitting experimental data $J(y_i)$, which is the measured intensity as a function of position, to a set of expansion functions by the method of least squares. Then, having these expansion coefficients and the analytically transformed expansion functions $\xi_k(r)$, $N(r)$ can be calculated easily.

The assumption of perfect cylindrical symmetry of the experiment is not entirely justified. It then becomes convenient to symmetrize the data as follows.

$$J^{+}(y) = \frac{1}{2}\,[J(y) + J(-y)] \quad \text{symmetrical part} \tag{B6}$$

$$J^{-}(y) = \frac{1}{2}\,[J(y) - J(-y)] \quad \text{antisymmetrical part} \tag{B7}$$

In the case of the Abel-inverted line profiles, each of these parts was fit by a least-squares technique to functions of the type

$$I^{+}(y) = \sum a_k \eta_k{}^{+}(y) \tag{B8}$$

$$I^{-}(y) = \sum b_k \eta_k{}^{-}(y) \tag{B9}$$

where $\eta_k{}^{+}(y)$ are symmetric functions and $\eta_k{}^{-}(y)$ are antisymmetric functions.

A measure of the goodness of fit is given by the error formula

$$\sigma = \left[\frac{\sum_{i=1}^{n} \left[J(y_i) - I(y_i) \right]^2}{N - 1} \right]^{1/2} \tag{B10}$$

The number of terms in the expansion was chosen such that σ was a minimum. The Abel-inverted functions are given by

$$N^{+}(r) = \sum a_k \xi_k{}^{+}(r) \tag{B11}$$

$$N^{-}(r) = \sum b_k \xi_k^{-}(r) \tag{B12}$$

where $\xi_k^{+}(r)$ and $\xi_k^{-}(r)$ are the transforms of $\eta_k^{+}(y)$ and $\eta_k^{-}(y)$, respectively.

The following functions were used.

$$\eta_k^{+}(y) = \left(R^2 - y^2\right)^k \qquad \eta_k^{-}(y) = \left(R^2 - y^2\right)^k y \tag{B13}$$

$$\xi_k^{+}(r) = \lambda_k \left(R^2 - r^2\right)^{k-1/2} \tag{B14}$$

$$\xi_k^{-}(r) = \lambda_k r \left(R^2 - r^2\right)^{k-1/2} \tag{B15}$$

where

$$\lambda_k = \frac{1}{\pi} 2^{2k} \frac{(k!)^2}{(2k)!} \tag{B16}$$

A computer program was written to compute the expansion coefficients a_k and b_k by the least-squares method. Then, the program was used to compute $N^{\pm}(r)$ compared with r for a set of radii.

In the cases other than the Abel-inverted line profiles, the symmetrization just described was not done. Here the data $J(y_i)$ were fitted to the symmetric functions, and no antisymmetric part was calculated.

REFERENCES

1. Wulff, H.: Die Linienprofile thermisch angeregter Heliumlinien. Zeit. für Physik, vol. 150, no. 5, 1958, pp. 614-631.

2. Griem, H. R.; Baranger, M.; Kolb, A.C.; and Oertel, G.: Stark Broadening of Neutral Helium Lines in a Plasma. Phys. Rev., vol. 125, no. 1, Jan. 1, 1962, pp. 177-195.

3. Vidal, C. R.: Die Druckverbreiterung der Balmer-Linien und der diffusen Linien des Heliums. Zeit. für Naturforschung, vol. 19a, 1964, pp. 947-967.

4. Pfennig, H.; and Trefftz, E.: Die Druckverbreiterung der Diffusen Heliumlinien, Vergleich Zwischen Messung und Theory im Quasistatischen Bereich, Zeit. Naturforschung, vol. 21a, 1966, pp. 697-718.

5. Greig, J. R.; Lim, C. P.; Moo-Young, G. A.; Palumbo, G.; and Griem, Hans R.: Measurements of the Stark Broadening of two Neutral Helium Lines in a Plasma. Phys. Rev., vol. 172, no. 1, Aug. 5, 1968, pp. 148-153.

6. Oertel, G.: Paper in Proceedings of the 8th International Conference on Phenomena in Ionized Gases, Vienna, 1967. Springer-Verlag (Berlin), 1968, p. 279.

7. Schlüter, H.: Studies on the Transition from Quasi-static to Impact Electron Contributions of Linear Stark Broadening. J. Quant. Spectrosc. Radiat. Transfer, vol. 8, no. 5, May 1968, pp. 1217-1232.

8. Edmonds, Frank N., Jr.; Schlüter, Hans; and Wells, Donald C., III: Hydrogen-Line Stark Broadening Functions. Memoirs Roy. Astron. Soc., vol. 71, pt. 5, 1967, pp. 271-344.

9. Pfennig, H.; and Trefftz, E.: Tables of the Stark Effect of Helium. Rept MPI-PAE/Astro 18/65, Max-Planck Institut für Physik and Astrophysik, München, 1965.

10. Baranger, Michel; and Mozer, Bernard: Electric Field Distributions in an Ionized Gas. Phys. Rev., vol. 115, no. 3, Aug. 1, 1959, pp. 521-525.

11. Anderson, A. D.; and Griem, H. R.: Continuum Emission Coefficients from the Quantum Defect Method. Proceedings of the 6th International Conference on Ionization Phenomena in Gases. North Holland Publishing Company (Amsterdam), vol. 3, 1963, pp. 293-295.

12. Karzas, W. J.; and Latter, R.: Electron Radiative Transitions in a Coulomb Field. Astrophys. J., 6. Suppl. Ser., 55, May 1961, pp. 161-212.

13. Griem, Hans R.: Plasma Spectroscopy. McGraw-Hill (New York), 1964.

14. Foster, J. Stuart: Application of Quantum Mechanics to the Stark Effect in Helium. Proc. Roy. Soc. (London), vol. A117, 1927, pp. 137-163.

15. Bethe, Hans A.; and Salpeter, Edwin E.: Quantum Mechanics of One- and Two-Electron Atoms. Springer-Verlag (Berlin), 1957.

16. Martin, W. C.: Energy Levels and Spectrum of Neutral Helium (^{4}He I). J. Res. NBS, Section A (Phys-Chem), vol. 64, no. 1, Jan.-Feb. 1960, pp. 19-28.

17. Hooper, C. F., Jr.: Electric Microfield Distributions in Plasmas. Phys. Rev., vol. 149, no. 1, Sept. 9, 1966, pp. 77-91.

18. Griem, Hans R.: Corrections to the Asymptotic Holtsmark Formula for Hydrogen Lines Broadened by Electrons and Ions in a Plasma. Astrophysical J., vol. 147, no. 3, Mar. 1967, pp. 1092-1099.

19. Traving, G.: Über die Theorie der Druckverbreiterung von Spektrallinien. G. Braun (Karlsruhe), 1960, p. 115.

20. Winovich, Warren: On the Equilibrium Sonic-Flow Method for Evaluating Electric-Arc Air-Heater Performance. NASA TN D-2132, 1964, p. 36.

21. Brahde, Rolf: The Influence of a Scanning Slit on the Line Profile Observed with a Spectrograph. Rept. No. Scientific-3 of Contract AF61 (052)-743, Astrophysica Norvegica, vol. 9, no. 21, 1965, pp. 199-212.

22. Barford, N. C.: Experimental Measurements: Precision, Error and Truth. Addison-Wesley Publishing Co. (London), 1967.

23. Green, Louis C.; Johnson, Norma C.; and Kolchin, Eleanor K.: Oscillator Strengths for Singlet and Triplet Series in Neutral Helium. Astrophysical J., vol. 144, no. 1, Apr. 1966, pp. 369-375.

24. Trefftz, E.; Schlüter, A.; Dettmar, K. H.; and Jörgens, K.: Oszillatorstärken für Neutrales Helium. Zeit. für Astrophysik, vol. 44, no. 1, 1957, pp. 1-17.

25. Freeman, Mark P.; and Katz, S.: Determination of a Radiance-Coefficient Profile from the Observed Asymmetric Radiance Distribution of an Optically Thin Radiating Medium. J. Opt. Soc. Amer., vol. 53, no. 10, Oct. 1963, pp. 1172-1179.

26. Unsöld, Albrecht: Physik der Sternatmosphären, mit besonderer Berücksichtigung der Sonne. Springer-Verlag (Berlin), 1955, p. 866.

27. Birkeland, Jorgen W.; and Oss, John P.: Spatial Resolution of Emission and Absorption Coefficients in Self-Absorbing Sources of Cylindrical Symmetry. Rept No. ARL 67-0279 Office of Aerospace Research USAF. Dec. 1967, p. 40.